nature metabolism

Article

https://doi.org/10.1038/s42255-026-01510-2

A conserved hormonal signalling–H2A.Z axis rapidly reorganizes 3D chromatin interactions in adipocyte thermogenesis

Received: 26 November 2025

Accepted: 10 March 2026

Published online: 21 April 2026

Check for updates

Yang Zhang[1,12], Rongbin Zheng[2,3,12], Tadataka Tsuji[1], Chih-Hao Wang[1], Xiang-Yu Liu[1,4], Yu-Hang Xing[4,5], Justin Darcy[1], Matthew D. Lynes[1], Morten Lundh[1,6], Rini Arianti[7], Ferenc Győry[8], Rui Dong[4,5], Brice Emanuelli[6], Sarah E. Johnstone[4,9], Miguel N. Rivera[4,5], Endre Kristóf[7], C. Ronald Kahn[1], Kaifu Chen[2,3] ✉ & Yu-Hua Tseng[1,10,11] ✉

Three-dimensional genome organization underlies gene regulation, yet how acute hormonal signalling reshapes chromatin structure to control metabolism remains unclear. β3-adrenergic receptor (β3-AR) hormonal signalling drives adipocyte thermogenesis. Here, we show three-dimensional genome maps of mouse and primary human brown adipocytes during thermogenesis using Micro-C. We find that β3-AR signalling rapidly reorganizes chromatin loops within 4 h, with dynamically gained loops coupled to thermogenic gene activation in both species. Mechanistically, β3-AR stimulation promotes histone variant H2A.Z deposition to enhance chromatin accessibility at loop anchors, facilitating the recruitment of bridging factor MED1. Loss of H2A.Z compromises loop formation and thermogenic gene activation across species. Brown fat-specific H2A.Z deficiency in mice impairs thermogenic activity and glucose tolerance. Integration with genome-wide association studies links H2A.Z-occupied loops to genetic variants associated with obesity and related metabolic disorders. Together, our findings uncover a cross-species conserved β3-AR signalling–H2A.Z axis that rapidly reorganizes chromatin interactions in adipocyte thermogenesis, providing mechanistic and translational insights into metabolic regulation.

Brown adipose tissue (BAT) maintains body temperature by generating heat through metabolizing glucose and fatty acids, a physiological process termed adaptive thermogenesis[1]. BAT activation inversely correlates with body mass index (BMI) and positively impacts cardiometabolic health in humans[2,3], making it a promising target for combating obesity and its associated metabolic disorders[4]. In response to cold exposure, the hormone noradrenaline, which is released from sympathetic nerves, stimulates the β3-AR in brown adipocytes, resulting in the rapid activation of genes essential for heat generation[5]. While transcription factors, cofactors and histone modifications have been implicated in orchestrating thermogenic gene activation[6–8], it remains unknown whether β3-AR signalling elicits a rapid transcriptional response by modulating three-dimensional (3D) genome organization, an increasingly recognized regulator of gene expression[9,10]. The contribution of 3D genome organization to adaptive metabolism has yet to be elucidated.

Recent advancements in high-throughput chromosome conformation capture-based methodologies, alongside the development

A full list of affiliations appears at the end of the paper. ✉e-mail: kaifu.chen@childrens.harvard.edu; yu-hua.tseng@joslin.harvard.edu

of high-resolution Micro-C, have revealed the intricate hierarchical structure of 3D genome organization in eukaryotic cells[10–12]. At the megabase scale, chromatin segregates into gene-active compartment A and gene-inactive compartment B[13]. Below the level of compartments, CTCF and cohesin coordinate genome folding into topologically associating domains (TADs) through DNA loop extrusion[14,15]. TADs vary in size from hundreds of kilobases to a few megabases[14]. At a much finer scale, long-range chromatin interactions (henceforth referred to as chromatin loops) regulate gene expression by bringing distal regulatory elements (for example, enhancers) into proximity with gene promoters[11,12]. Most functional insights into 3D genome organization have come from studies of long-term processes such as development and cell differentiation[9,16,17]. By contrast, it remains unexplored whether the 3D genome can be rapidly reshaped by β3-AR hormonal signalling to drive metabolic adaptation in response to acute environmental cues. Notably, BAT-mediated thermogenesis represents an evolutionarily conserved adaptation that enables many mammals to maintain body temperature[18], prompting the question of whether 3D genome organization might also function as a conserved regulatory layer in this process.

Using Micro-C, our study presents the 3D genome maps in both mouse and primary human brown adipocytes during thermogenesis. Our results reveal consistent patterns of rapid and substantial chromatin loop reorganization within 4 h of β3-AR stimulation in both species. Integration with RNA sequencing (RNA-seq) and precision run-on sequencing (PRO-seq) demonstrates that dynamically gained chromatin loops are associated with thermogenic gene activation. Through combined analyses of Micro-C, chromatin immunoprecipitation coupled with sequencing (ChIP–seq) and the assay for transposase-accessible chromatin with sequencing (ATAC-seq), we find that the histone variant H2A.Z contributes to β3-AR signalling-induced loop formation by enhancing chromatin accessibility at loop anchors, providing a permissive chromatin environment that facilitates the recruitment of the bridging factor MED1, a subunit of the Mediator complex. Loss of H2A.Z selectively disrupts the formation of dynamically gained loops in both mouse and human brown adipocytes, impairing thermogenic gene activation and reducing thermogenic activity. BAT-specific H2A.Z knockout mice exhibit decreased energy expenditure, impaired glucose tolerance and reduced insulin sensitivity, underscoring the physiological importance of this pathway. Integration with genome-wide association studies (GWASs) further reveals that H2A.Z-occupied loops are linked to genetic variants associated with obesity and its related metabolic disorders. Together, our findings reveal a cross-species conserved mechanism by which β3-AR signalling engages histone variant H2A.Z to promote chromatin looping during thermogenesis. This discovery highlights rapid chromatin loop reorganization as a conserved feature in thermogenic adipocytes and underscores its importance to metabolic health.

Results

Dynamic changes in chromatin loops during thermogenesis

To elucidate the effects of acute β3-AR hormonal signalling on 3D genome organization during thermogenesis, we treated in vitro cultured mouse brown adipocytes with vehicle or a selective β3-AR agonist, CL316,243, for 4 h to initiate the thermogenic programme (Fig. 1a). We then profiled the gene expression of vehicle-treated and β3-AR-stimulated brown adipocytes by RNA-seq. The results confirmed gene activation during thermogenesis induced by β3-AR signalling, with 693 upregulated genes enriched in pathways pivotal for the key functions of brown adipocytes, involving thermogenesis, lipid metabolism and energy expenditure (Extended Data Fig. 1a,b). To interrogate whether the acute activation of β3-AR signalling could mediate 3D genome reorganization, which could contribute to gene activation during thermogenesis (Fig. 1a), we performed the Micro-C assay for both vehicle-treated and β3-AR-stimulated brown adipocytes. We generated four highly reproducible biological replicates for each condition (Extended Data Fig. 2a), producing a total of ~1.1 billion valid read pairs across both conditions (Supplementary Table 1).

Chromatin interaction maps derived from Micro-C reveal ultrafine 3D genome architectures at the level of chromatin loops[11,12]. Using the Peakachu algorithm[19], we detected 24,078 and 23,532 chromatin loops for vehicle-treated and β3-AR-stimulated brown adipocytes, respectively (Supplementary Table 1). To assess the degree of plasticity of chromatin loops in response to β3-AR stimulation, we defined differential

Fig. 1 | Dynamic changes in chromatin loops during thermogenesis in brown adipocytes. a, Schematic outlining the study questions: Does chromatin reorganization occur during thermogenesis induced by acute treatment with CL316,243, a selective agonist of β3-AR? Does chromatin reorganization contribute to gene activation during thermogenesis? **b**, Left: violin plot showing contact frequencies of upregulated (Up), downregulated (Down) and unchanged (No) loops in β3-AR-stimulated (β3AR-stim; orange) versus vehicle-treated (vehicle; grey) brown adipocytes. Violin plot shows median (dot), 25–75th percentiles (bar) and 1.5 times the interquartile range (IQR; whiskers). Right: averaged contact signals (APA) plotted with loops sorted by Up, Down or No. The contact map was normalized by matrix balancing and distance (Obs/Exp). The APA plots show signals of aligned loop anchor centres and flanking 50-kb regions. The numerical value in the upper-left corner of each plot indicates the ratio of contact enrichment for the centre pixels. This colour scheme and normalization method are used for normalized matrices throughout the paper unless otherwise mentioned. **c**, Pie charts showing the percentage of upregulated, downregulated or unchanged loops mediated by β3-AR stimulation for E-P, P-P and P-other loops. **d**,**e**, Rank-ordered distribution of delta loop contact frequency (Δ contact frequency) against gene expression (**d**) and transcription (**e**) changes ($\log_2$ fold change, $\log_2$FC) after β3-AR stimulation. The associated gene for each P-anchored loop was determined by the identification of the TSS located ±5 kb around the loop anchor. The distribution of $\log_2$FC in gene expression (**d**) and transcription (**e**) for each loop type was smoothed by LOESS (locally estimated scatterplot smoothing) regression. The error bands indicate the fitted curve ± s.e.m. with a 95% confidence interval. **f**, Functional enrichment analysis for upregulated genes associated with gained P-anchored loops after β3-AR stimulation. Selected brown adipocyte-related terms are shown. The *x* axis shows the statistical significance ($-\log_2$ adjusted *P* value, $-\log_2(P_{adj})$). Gene-set enrichment was performed using Enrichr (one-sided Fisher's exact test with Benjamini–Hochberg correction). **g**,**h**, Snapshots of Micro-C contact maps at the *Slc16a1* (**g**) and *Ppargc1a* (**h**) loci comparing vehicle-treated (upper-right triangle) and β3-AR-stimulated (bottom-left triangle) brown adipocytes. Gene annotations are shown at the top (exons in dark green). Trimethylated histone H3 Lys4 (H3K4me3) and H3K27ac ChIP–seq tracks are included to facilitate the visualization of promoter and enhancer regions, respectively. Bar plots showing the fold changes in *Slc16a1* (**g**) and *Ppargc1a* (**h**) expression and transcription quantified by RNA-seq and PRO-seq, respectively. Error bar represents the mean ± s.d. of three biological replicates of RNA-seq per condition. Two-sided Wald test implemented in DESeq2. The E-P loop is highlighted by a black arched line, and the interacting enhancer and promoter are highlighted by transparent light-purple boxes in the chromatin tracks. E-P loops in the contact maps are highlighted by circles. Micro-C contact maps and ChIP–seq were visualized using Juicebox software. **i**,**j**, The CRISPR–Cas9-dual gRNA system was used to delete the annotated enhancers identified in **g** and **h**, respectively. Left: genomic DNA PCR followed by agarose gel electrophoresis. Del, deletion. Middle: the interaction frequency of E-P loops was assessed by 3C-qPCR and normalized to the interaction frequency between two consecutive HindIII (**i**) or NdeI (**j**) fragments at the *Rplp0* locus. Adipocytes were treated with vehicle or 1 μM CL316,243 (CL) for 4 h before analysis. $N = 4$ technical replicates per group for qPCR. Right: expression of *Slc16a1* (**i**) and *Ppargc1a* (**j**) in different conditions. $N = 3$ technical replicates per group for qPCR with reverse transcription (RT–qPCR). In **i** and **j**, the data shown are from one of two biological replicates with similar results, and error bars indicate the mean ± s.d. of technical replicates in each group. Differences were assessed with two-sided unpaired *t*-test. Icons in **a**, **i** and **j** created in BioRender; Tseng, Y. https://biorender.com/iu0x6dt (2026).

https://doi.org/10.1038/s42255-026-01510-2

loops by requiring at least a twofold change in the probability score determined by Peakachu. This criterion was consistently applied to define differential loops throughout the study. By doing so, 7,600 upregulated and 8,639 downregulated loops were identified within 4 h of β3-AR stimulation (Fig. 1b and Supplementary Table 1). Consistently, aggregate peak analysis (APA) revealed that the averaged contact signal of the upregulated loops was greater in the β3-AR-stimulated brown adipocytes than in the vehicle-treated adipocytes, and the downregulated loops displayed lower averaged contact signal (Fig. 1b).

Together, Micro-C analyses in brown adipocytes reveal that acute activation of β3-AR signalling leads to rapid and dynamic changes in chromatin loops during thermogenesis, highlighting the rapid adaptability of genome organization in response to acute external cues.

Dynamically gained chromatin loops are coupled to gene activation in the thermogenic programme

To delineate whether the dynamic changes in chromatin loops mediated by β3-AR signalling are associated with gene activation in the thermogenic programme, we performed an integrative analysis of the Micro-C and RNA-seq data from both conditions. Previous studies have suggested that the contact frequency of enhancer–promoter (E-P) and promoter–promoter (P-P) loops, rather than other types of chromatin loops, aligns positively with gene expression levels[11,20]. Thus, we decided to focus on promoter-anchored chromatin loops with at least one anchor overlapping with a gene transcription start site (TSS; Supplementary Table 2). To define active enhancers in brown adipocytes, we performed ChIP–seq for acetylated histone H3 Lys27 (H3K27ac) and integrated the obtained data with annotated candidate enhancers from the ENCODE SCREEN in mouse. The promoter-anchored chromatin loops in brown adipocytes were then classified into E-P, P-P and P-other (non-promoter/enhancer regions) loops (Supplementary Table 2). All three types of promoter-anchored chromatin loops exhibited dynamic changes in response to β3-AR stimulation, with 37–49% of the loops identified as differential loops (Fig. 1c and Supplementary Table 2). Notably, integrative analysis revealed that promoter-anchored loops, particularly E-P loops, with increased contact frequency after β3-AR stimulation were coupled to enhanced expression of their associated genes (Fig. 1d). To further

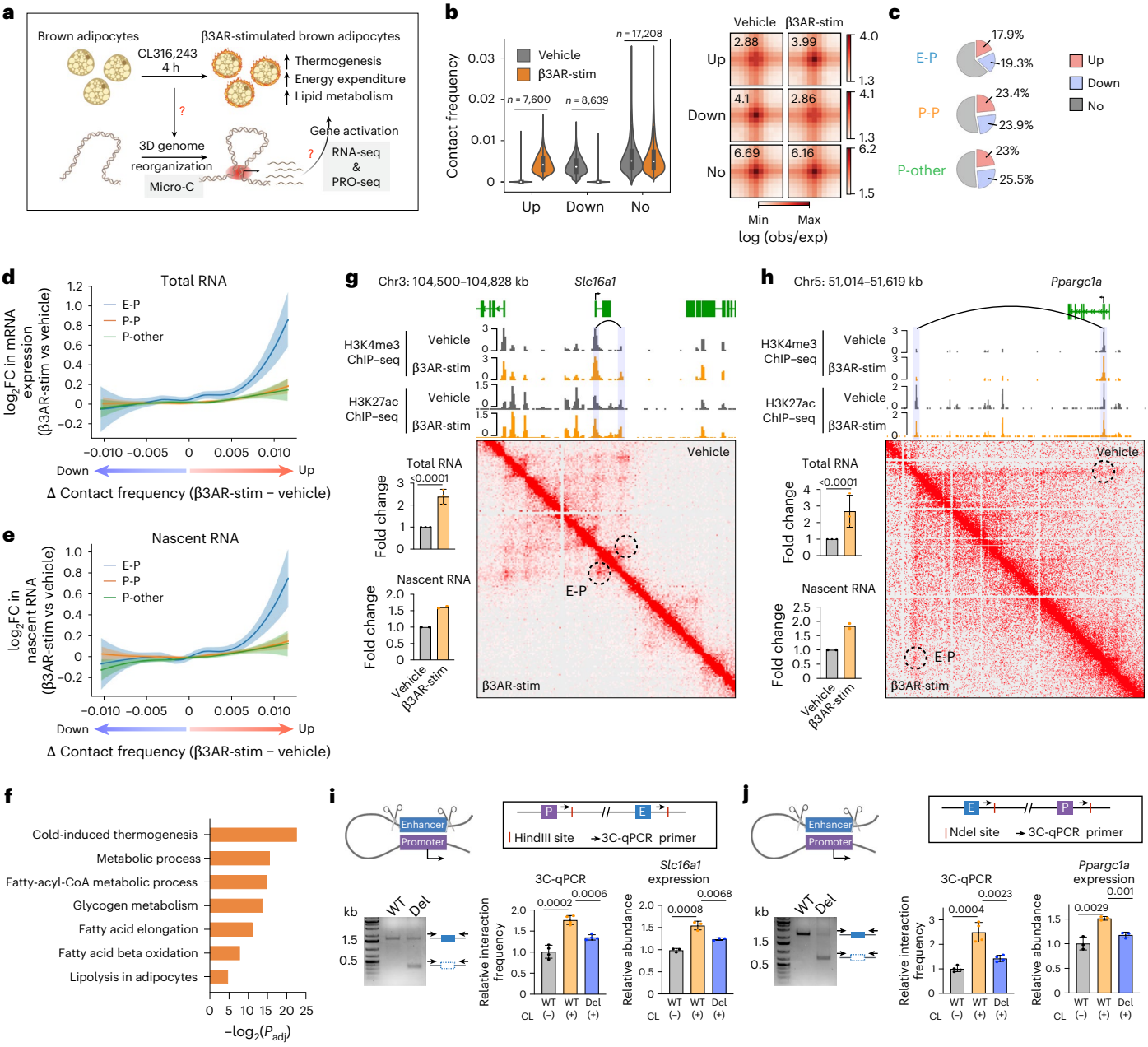

assess transcriptional changes, we profiled nascent transcription using PRO-seq[21]. We observed that changes in steady-state mRNA correlated well with changes in nascent transcription after acute β3-AR stimulation (Extended Data Fig. 2b). Combined analysis showed that dynamically gained loops with increased contact frequency, particularly E-P loops, were positively associated with transcriptional activation during thermogenesis (Fig. 1e). However, we noticed that such concordant patterns were not observed for loops with decreased contact frequency, as the average expression and nascent transcription of their associated genes remained largely unchanged in response to β3-AR stimulation (Fig. 1d,e). Collectively, our data indicate that dynamically gained, but not lost, chromatin loops are coupled to gene activation during thermogenesis in brown adipocytes.

Of the 693 genes upregulated in response to β3-AR stimulation, 422 were associated with promoter-anchored loops (Extended Data Fig. 2c). Notably, 80% of these genes were linked to dynamically gained promoter-anchored loops (Extended Data Fig. 2c and Supplementary Table 2). Importantly, these dynamically gained loop-associated genes were involved in the thermogenic function of brown adipocytes, including thermogenesis, lipolysis and fatty acid metabolism (Fig. 1f). These results underscore the essential role of β3-AR stimulation-induced dynamic loop formation in orchestrating the thermogenic programme in brown adipocytes.

Two representative examples of the dynamically gained chromatin loop-associated genes, *Slc16a1* and *Ppargc1a*, are illustrated in Fig. 1g,h. The proteins, monocarboxylate transporter 1 (MCT1) and PPARγ coactivator 1-alpha (PGC1A), encoded by *Slc16a1* and *Ppargc1a*, respectively, are essential for the metabolic function of thermogenic adipocytes[22,23]. Micro-C chromatin interaction maps revealed a short-range (~35 kb) E-P loop connecting the promoter of *Slc16a1* with a downstream enhancer, with increased contact frequency in response to β3-AR stimulation (Fig. 1g). This enhanced interaction was accompanied by elevated expression and transcriptional activity of *Slc16a1* in β3-AR-stimulated brown adipocytes (Fig. 1g). At the *Ppargc1a* locus, a relatively longer range (~500 kb) upregulated E-P loop was identified (Fig. 1h), and its increased contact frequency was associated with enhanced *Ppargc1a* expression and transcription after stimulation (Fig. 1h). Notably, deletion of these enhancer DNA fragments using the CRISPR–Cas9 system led to reduced interaction between the enhancer and promoter regions after stimulation, as demonstrated by chromosome conformation capture (3C)-qPCR, resulting in impaired upregulation of *Slc16a1* and *Ppargc1a* (Fig. 1i,j). Additionally, *Ucp1* is a pivotal gene involved in heat generation during thermogenesis in brown adipocytes[24]. β3-AR stimulation increased *Ucp1* expression and transcription (Extended Data Fig. 2d). Alongside two well-characterized proximal enhancers[25], a less described distal enhancer[26] located 12 kb upstream of the *Ucp1* TSS was also observed (Extended Data Fig. 2d). Similarly, deletion of this distal enhancer DNA fragment impaired β3-AR stimulation-induced E-P loop formation and led to reduced *Ucp1* expression (Extended Data Fig. 2e).

Interestingly, temporal analysis of the interaction frequencies for these E-P loops revealed a progressive increase in loop formation during β3-AR stimulation (Extended Data Fig. 2f). After removal of stimulation, the loops gradually disassembled (Extended Data Fig. 2f), highlighting their highly dynamic and reversible nature.

Collectively, the analysis of chromatin looping using our Micro-C data reveals that activation of β3-AR signalling within 4 h in brown adipocytes leads to dynamic changes in chromatin loops. The dynamically gained chromatin loops favour gene activation in the thermogenic programme.

Acute activation of β3-AR signalling modestly affects large-scale chromatin structures

In addition to fine-scale chromatin loops, Micro-C maps also provide information on large-scale chromatin structures, including A/B compartments and TADs. When we assessed A/B compartment switching in vehicle-treated and β3-AR-stimulated brown adipocytes, approximately 2.2% of the compartments displayed plasticity between the two conditions (Extended Data Fig. 3a). Consistent with previous studies, the A/B compartment switches correlated well with changes in the corresponding gene expression, with the A-to-B switch associated with decreased gene expression and vice versa (Extended Data Fig. 3b).

At the level of TADs, we found that the number of detected TADs was comparable between the two conditions (Extended Data Fig. 3c). Around 1–2% of TADs exhibited differential strength in boundaries after acute β3-AR stimulation (Extended Data Fig. 3d). Our findings further support previous observations that TADs are relatively stable across different cell types[14].

H2A.Z is required for β3-AR signalling-induced gene activation and cellular metabolism

Next, we sought to identify the factors that mediate the dynamic formation of chromatin loops associated with thermogenic gene activation in response to β3-AR signalling. We hypothesized that such factors could be recruited to regulatory DNA regions after β3-AR stimulation, facilitating the formation of dynamically gained chromatin loops and activating thermogenic gene expression. To this end, we performed unbiased CRISPR-based engineered DNA-binding molecule-mediated chromatin immunoprecipitation (enChIP)[27] in mouse brown adipocytes, targeting a region up to 3 kb upstream of the *Ucp1* TSS (Extended Data Fig. 4a). Proteins immunoprecipitated from vehicle-treated and β3-AR-stimulated brown adipocytes were analysed by mass spectrometry (Extended Data Fig. 4a,b). Unexpectedly, the histone variant H2A.Z was among the most strongly enriched proteins at *Ucp1* regulatory regions after β3-AR stimulation (Extended Data Fig. 4c and Supplementary Table 3). Mammalian H2A.Z is an evolutionarily conserved variant of the canonical histone H2A[28], previously linked to gene regulation during development and cell differentiation[28], but its role in thermogenesis remains entirely unknown. Given its enrichment at promoters and enhancers, we reasoned that H2A.Z may serve as an active chromatin regulator that couples β3-AR signalling to thermogenic gene transcription.

To test our hypothesis, we first performed loss-of-function experiments to evaluate the importance of H2A.Z on gene activation in response to β3-AR stimulation in mouse brown adipocytes. H2A.Z has two major isoforms, known as H2A.Z1 and H2A.Z2 (ref. 28). Although differing by only three amino acids, they are encoded by two distinct genes, *H2AFZ* and *H2AFV*, with distinct nucleotide sequences[28]. Lentiviruses expressing isoform-specific CRISPR/guide RNAs (gRNAs) were utilized to transduce brown preadipocytes, and knockdown of each isoform was confirmed at both the mRNA and protein levels (Extended Data Fig. 4d). Notably, H2A.Z1 is the predominant isoform in both preadipocytes and mature adipocytes (Extended Data Fig. 4e), making its depletion easily detectable at the protein level, whereas H2A.Z2 knockdown was obscured by H2A.Z1 (Extended Data Fig. 4d). We found that the loss of H2A.Z1, but not H2A.Z2, notably impeded preadipocyte proliferation (Extended Data Fig. 4f), leading to impaired mitotic clonal expansion (Extended Data Fig. 4g), a prerequisite for adipogenesis[29]. Consequently, knockdown of H2A.Z1 resulted in reduced lipid accumulation and decreased expression of adipogenic markers (Extended Data Fig. 4h,i). In contrast, depletion of H2A.Z2 did not affect adipogenesis (Extended Data Fig. 4h,i), and adipocytes lacking H2A.Z2 displayed no defects in the expression of thermogenic genes (Extended Data Fig. 4j). Thus, in the following study, we decided to focus on H2A.Z1 and refer to it as H2A.Z unless otherwise noted.

To further distinguish the impact of H2A.Z on thermogenic gene activation in adipocytes from its role in adipogenesis, we introduced a short hairpin RNA (shRNA) targeting H2A.Z directly into mature brown adipocytes via lentiviral infection (Fig. 2a). Five days after infection, we observed a notable reduction in H2A.Z at both

the mRNA and protein levels (Fig. 2b). Knockdown of H2A.Z in fully differentiated brown adipocytes had no discernible effect on lipid accumulation (Extended Data Fig. 5a). Control and H2A.Z knockdown adipocytes had similar levels of *Pparg*, *Adipoq* and *Prdm16* mRNAs, the expression of which was also not affected by β3-AR stimulation (Extended Data Fig. 5a). Importantly, we found that the loss of H2A.Z substantially impaired the upregulation of β3-AR stimulation-induced thermogenic genes, including *Ucp1*, *Ppargc1a* and *Cidea*, as well as genes involved in fuel utilization, such as *Pck1* and *Elovl3* (Fig. 2c). Similarly, when we introduced a pool of four small interfering RNAs (siRNAs) targeting H2A.Z into mature brown adipocytes via transfection, the expression levels of genes induced by β3-AR stimulation were reduced, while the expression of adipogenic markers was unaffected (Extended Data Fig. 5b,c). Collectively, these loss-of-function experiments show that H2A.Z is required for β3-AR stimulation-induced thermogenic gene activation in brown adipocytes.

To comprehensively elucidate the regulatory role of H2A.Z in gene activation, we performed RNA-seq in both control and H2A.Z knockdown brown adipocytes after β3-AR stimulation. Notably, over 66% (459 of 693) of the β3-AR stimulation-upregulated genes (Extended Data Fig. 1a) exhibited reduced expression after H2A.Z knockdown (Fig. 2d). The transcriptional regulatory role of H2A.Z was supported by PRO-seq analysis, which revealed reduced nascent transcription of β3-AR stimulation-activated genes in H2A.Z knockdown adipocytes (Extended Data Fig. 5d). In line with the gene expression changes, gene-set enrichment analysis (GSEA) showed that functional pathways associated with the thermogenic activity of brown adipocytes were downregulated by H2A.Z knockdown after β3-AR stimulation (Fig. 2e and Extended Data Fig. 5e). Consistent with impaired gene activation, knockdown of H2A.Z in brown adipocytes resulted in compromised mitochondrial activity and reduced glucose uptake (Fig. 2f,g and Extended Data Fig. 5f). These results demonstrate that H2A.Z is required for gene activation in the thermogenic programme induced by β3-AR signalling, thus impacting the cellular metabolism of brown adipocytes. Taken together, these findings reveal a mechanism by which adrenergic signalling engages a specific histone variant to regulate thermogenic transcriptional programmes.

p18^{Hamlet}/SRCAP complex mediates H2A.Z nucleosome incorporation in response to β3-AR signalling to regulate gene activation

We then investigated how β3-AR signalling regulates H2A.Z to drive transcriptional activation. In mammals, the SNF2-related CREBBP activator protein (SRCAP) complex functions as a loading machinery for H2A.Z nucleosome deposition[30]. However, how β3-AR signalling modulates the SRCAP complex to control H2A.Z deposition remains unknown. Znhit1 (p18^{Hamlet})[30], a subunit of the complex, has been reported as a substrate of p38 MAPK signalling under ultraviolet irradiation[31]. We detected increased threonine phosphorylation of p18^{Hamlet} in both immortalized and primary brown adipocytes after β3-AR stimulation (Fig. 2h). Using the Group-based Prediction System (GPS), we identified threonine residues, Thr64 and Thr103 (Fig. 2h), as the putative targets of p38 MAPK, which is activated by β3-AR stimulation in brown adipocytes[32]. Through single or dual mutation of these two sites, we found that the phosphorylation of Thr103 in p18^{Hamlet} was required for its interaction with other subunits in the complex, including ARP6 and YL1, after β3-AR stimulation (Fig. 2i). YL1 is the subunit known to directly interact with H2A.Z and mediate its deposition[33]. Notably, the interaction between YL1 and H2A.Z was augmented by β3-AR stimulation (Fig. 2j). Loss of p18^{Hamlet} impeded thermogenic gene activation after stimulation (Fig. 2k,l), which was restored by wild-type (WT) p18^{Hamlet} but not by the Thr103 mutant (Extended Data Fig. 5g). The deficiency in gene activation was attributed to the impaired chromatin incorporation of H2A.Z into the regulatory DNA regions of those thermogenic genes, as revealed by H2A.Z ChIP–qPCR (Fig. 2m).

Altogether, these results unveil a non-canonical pathway by which β3-AR signalling regulates thermogenic gene expression; it involves increasing the phosphorylation of p18^{Hamlet}, thereby facilitating the assembly of the SRCAP complex, which promotes H2A.Z deposition to trigger gene activation in the thermogenic programme (Fig. 2n).

Fig. 2 | The p18^{Hamlet}/SRCAP complex-mediated H2A.Z nucleosome incorporation is required for gene activation and cellular metabolism. **a**, Schematic illustrating lentiviral shRNA-mediated H2A.Z knockdown in mature mouse brown adipocytes, with non-targeting shRNA serving as a control. **b**, Left: H2A.Z expression in the control (Ctrl) and H2A.Z knockdown (KD) adipocytes. $N = 6$ technical replicates per group. Right: H2A.Z protein levels assessed by immunoblotting. Relative abundance was determined using ImageJ, normalized to each corresponding H3 signal and the first control sample (set as 1.0), and labelled underneath. **c**, Expression of β3-AR stimulation-upregulated genes in control and H2A.Z KD adipocytes following vehicle or 1 μM CL316,243 treatment for 4 h. $N = 6$ technical replicates per group, except for *Ppargc1a* (vehicle-treated Ctrl), where $n = 5$. **d**, GSEA for β3-AR stimulation-upregulated genes ($n = 693$) after H2A.Z KD. A negative enrichment score in the *y* axis signifies the downregulation of β3-AR-upregulated genes after H2A.Z KD. The vertical black lines on the *x* axis represent β3-AR-upregulated genes ranked by their fold changes in gene expression after H2A.Z KD. $N = 3$ biological replicates per group for RNA-seq. **e**, GSEA for Thermogenesis pathway after H2A.Z KD with β3-AR stimulation. $N = 3$ biological replicates per group for RNA-seq. For more functional pathway analysis, see Extended Data Fig. 5e. **f**, Oxygen consumption rate (OCR) in the control and H2A.Z KD adipocytes pretreated with 1 μM CL316,243 overnight. OCR was measured following sequential addition of Oligomycin (OA, ATP production respiration), FCCP (maximal respiration) and antimycin A (AA, non-mitochondrial respiration). OCR was normalized to the protein content. $N = 10$ technical replicates for control group and $n = 7$ for KD group. **g**, Glucose uptake in control and H2A.Z KD adipocytes following overnight 1 μM CL316,243 pretreatment. $N = 3$ technical replicates per group. **h**, Phosphorylation of p18^{Hamlet} after β3-AR stimulation in immortalized (left) and primary (right) brown adipocytes. The relative phosphorylation level of p18^{Hamlet} was determined using ImageJ, normalized to each corresponding immunoprecipitated total p18^{Hamlet} and the vehicle-treated sample (set as 1.0), and labelled underneath. Bottom: predicted Thr phosphorylation sites for p18^{Hamlet} according to GPS 3.0. **i**, Co-immunoprecipitation for v5-tagged p18^{Hamlet} WT or mutants in adipocytes treated with 1 μM CL316,243 for 30 min. The levels of the interacting proteins ARP6 and YL1 in both the total lysate and the anti-v5-immunoprecipitate were analysed by immunoblotting. The relative abundance of YL1 or ARP6 in the anti-v5-immunoprecipitate was determined using ImageJ, normalized to each corresponding immunoprecipitated v5-p18^{Hamlet} and v5-p18^{Hamlet} WT sample (set as 1.0), and labelled underneath. **j**, Endogenous YL1 was immunoprecipitated and the level of H2A.Z was analysed by immunoblotting in both the total lysate and the anti-YL1 immunoprecipitate. The relative abundance of H2A.Z in the immunoprecipitate was determined using ImageJ, normalized to each corresponding immunoprecipitated YL1 and the vehicle-treated sample (set as 1.0), and labelled underneath. **k**, Protein level of p18^{Hamlet} in both control and siRNA-mediated p18^{Hamlet} knockdown adipocytes. The relative abundance of p18^{Hamlet} was determined using ImageJ, normalized to each corresponding Tubulin signal and the first control sample (set as 1.0), and labelled underneath. **l**, Expression of BAT selective and thermogenic genes in both control and siRNA-mediated p18^{Hamlet} knockdown adipocytes following vehicle or 1 μM CL316,243 treatment for 4 h. $N = 6$ technical replicates per group. NS, not significant. **m**, H2A.Z chromatin incorporation at indicated loci was assessed by H2A.Z ChIP–qPCR in control and shRNA-mediated p18^{Hamlet} knockdown adipocytes following vehicle or 1 μM CL316,243 treatment for 4 h. Rabbit IgG was used as a negative control for ChIP. $N = 3$ technical replicates per group for RT–qPCR. **n**, A model illustrating how β3-AR signalling mediates H2A.Z nucleosome deposition via the p18^{Hamlet}/SRCAP complex. In **b**, **c** and **f**–**m**, the data shown are from one of two biological replicates with similar results, and error bars indicate the mean ± s.d. of technical replicates in each group. Differences were assessed with a two-sided unpaired *t*-test. *P* values > 0.05 were considered to be not significant (NS). Icons in **a** and **n** created in BioRender; Tseng, Y. https://biorender.com/iu0x6dt (2026).

https://doi.org/10.1038/s42255-026-01510-2

Knockdown of H2A.Z largely impedes the formation of dynamically gained loops in response to β3-AR signalling

Next, we sought to assess whether H2A.Z regulates β3-AR stimulation-induced gene activation through affecting chromatin looping. To this end, we performed Micro-C experiments in H2A.Z knockdown mouse brown adipocytes after β3-AR stimulation (Fig. 3a). Micro-C data from four highly reproducible biological replicates were used to analyse chromatin loops in H2A.Z knockdown brown adipocytes (Extended Data Fig. 6a and Supplementary Table 4). To evaluate the impact of H2A.Z knockdown on chromatin looping, we conducted a comparative analysis of Micro-C data from β3-AR-stimulated control and H2A.Z knockdown brown adipocytes (Fig. 3a). The β3-AR-stimulated control brown adipocytes were identical to the β3-AR-stimulated brown adipocytes presented in Fig. 1. Both vehicle-treated and β3-AR-stimulated brown adipocytes were pre-transduced with lentivirus expressing a non-targeting shRNA to serve as controls for gene knockdown and are henceforth referred to as vehicle-treated control adipocytes and β3-AR-stimulated control adipocytes (Fig. 3a). After H2A.Z knockdown, we observed that 7,748 chromatin loops exhibited decreased contact frequencies, while only a minority ($n = 760$) displayed increased frequencies (Extended Data Fig. 6b). Overall, the knockdown of H2A.Z in brown adipocytes predominantly disrupts chromatin loop formation.

We further assessed the effects of H2A.Z knockdown on β3-AR stimulation-mediated dynamic changes in chromatin loops. Strikingly, the contact frequencies of β3-AR stimulation-upregulated loops were substantially reduced by H2A.Z knockdown (Fig. 3b), as supported by the decreased averaged contact signal revealed by APA (Fig. 3b and Supplementary Table 4). More than 50% of the loops were identified as weakened loops after H2A.Z knockdown (Fig. 3b), with reduced probability scores of at least twofold determined by the Peakachu algorithm. In contrast, β3-AR stimulation-downregulated or unchanged loops were largely unaffected by H2A.Z knockdown, displaying comparable averaged contact signals between control and H2A.Z knockdown adipocytes after stimulation (Extended Data Fig. 6c). These findings suggest that H2A.Z is primarily required for the formation of dynamically gained, rather than lost, chromatin loops in response to β3-AR stimulation. We further classified β3-AR stimulation-upregulated loops into E-P, P-P and P-other loops using the definitions we set in Fig. 1c (Extended Data Fig. 6d). The contact frequencies for all three types

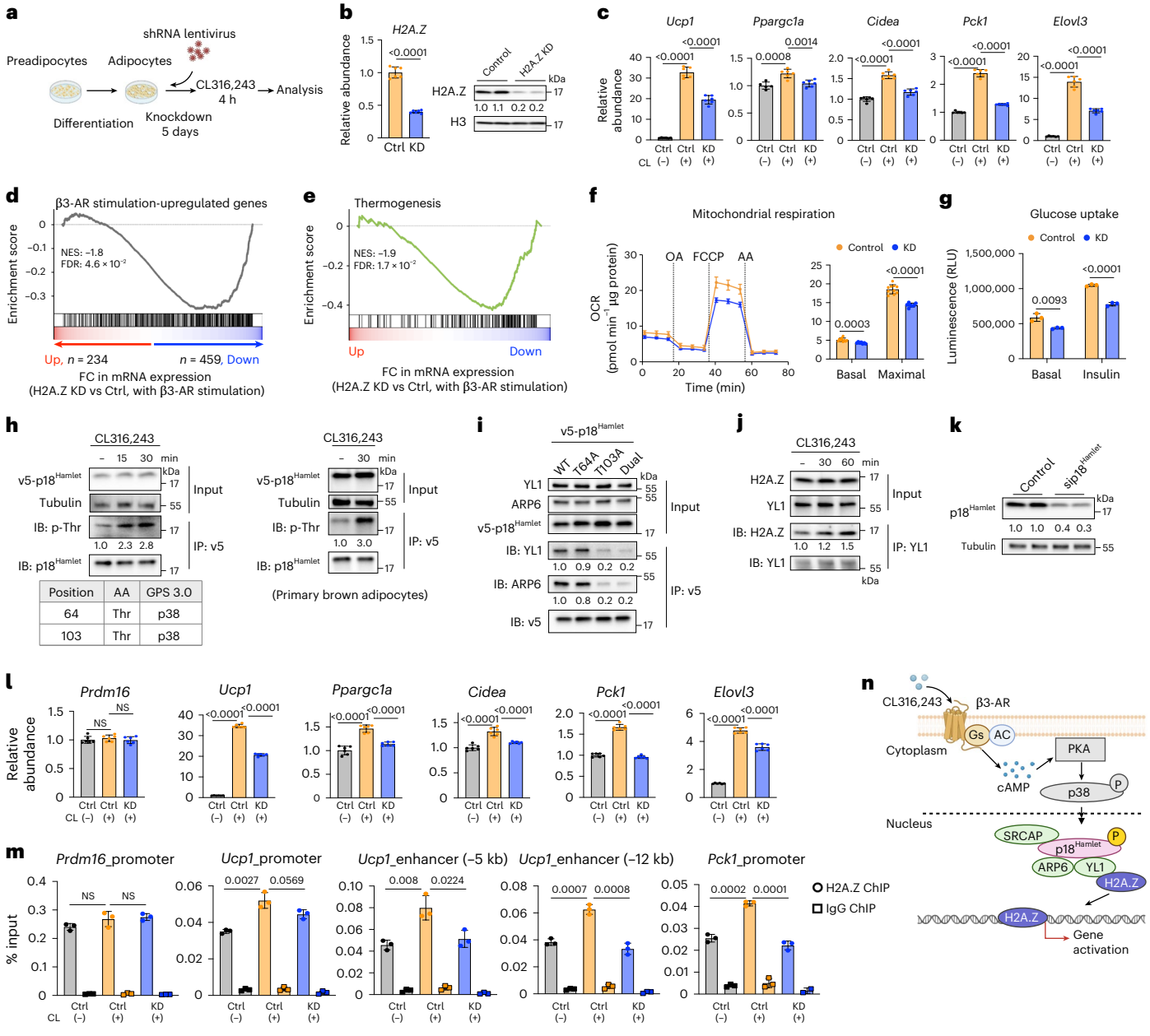

https://doi.org/10.1038/s42255-026-01510-2

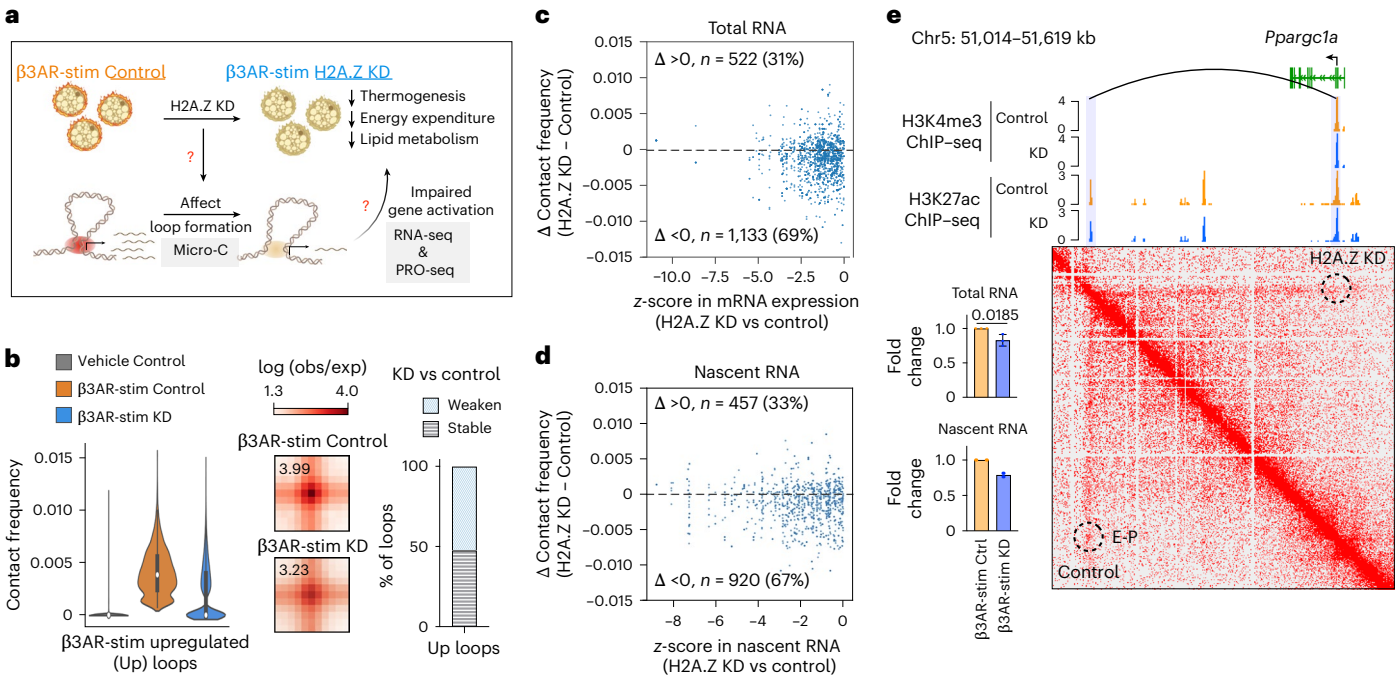

Fig. 3 | Knockdown of H2A.Z impairs dynamically gained loop formation induced by β3-AR stimulation. a, Scheme outlining the questions addressed in the figure. Is H2A.Z required for the dynamic changes in chromatin loops in response to acute β3-AR stimulation? Are chromatin loops affected by H2A.Z knockdown coupled to impaired gene activation in the thermogenic programme? Micro-C, RNA-seq and PRO-seq techniques are utilized to address these questions in β3-AR-stimulated control (β3AR-stim Control) and H2A.Z KD (β3AR-stim H2A.Z KD) mouse brown adipocytes. **b**, Left: violin plot showing contact frequencies of β3-AR stimulation (β3AR-stim)-upregulated (Up) loops (n = 7,600) in vehicle-treated control (vehicle Control; grey), β3-AR-stimulated control (β3AR-stim Control; orange) and β3-AR-stimulated H2A.Z knockdown (β3AR-stim KD; blue) brown adipocytes. Violin plot shows median (dot), 25–75th percentiles (bar) and 1.5 times the IQR (whiskers). Middle: averaged contact signals (APA) plotted for β3-AR stimulation-upregulated loops in the control and H2A.Z KD adipocytes. Right: bar plot showing the percentage of weakened (Weaken) and unaffected (Stable) loops by H2A.Z knockdown. **c**,**d**, Distribution of delta contact frequencies (Δ contact frequency) of promoter-anchored loops associated with genes exhibiting decreased expression (**c**) or transcription (**d**) after H2A.Z knockdown. Loops with negative delta values displayed decreased contact frequencies after H2A.Z knockdown. **e**, Snapshot of Micro-C contact maps comparing chromatin interactions at the *Ppargc1a* locus in the β3-AR-stimulated control (Control, bottom-left triangle) and β3-AR-stimulated H2A.Z knockdown (H2A.Z KD, upper-right triangle) brown adipocytes. Gene annotations are shown at the top (exons in dark green). H3K4me3 and H3K27ac ChIP–seq tracks are included to facilitate the visualization of promoter and enhancer regions, respectively. The ChIP–seq data shown are from one of two biological replicates with similar results. Bar plots showing the fold changes in *Ppargc1a* expression and transcription quantified by RNA-seq and PRO-seq, respectively. Error bar represents the mean ± s.d. of three biological replicates of RNA-seq per condition. P_{adj} value, two-sided Wald test implemented in DESeq2. The *Ppargc1a*-associated E-P loop is highlighted by a black arched line, and the interacting enhancer and promoter are highlighted by transparent light-purple boxes in the chromatin tracks. E-P loops in the contact maps are highlighted by circles. Micro-C contact maps and ChIP–seq were visualized using Juicebox software. Icon in **a** created in BioRender; Tseng, Y. https://biorender.com/iu0x6dt (2026).

of chromatin loops were substantially reduced by H2A.Z knockdown, with 44.6% weakened loops for E-P loops, 50.7% for P-P loops and 51.9% for P-other loops (Extended Data Fig. 6d and Supplementary Table 4). Taken together, these findings demonstrate that H2A.Z knockdown markedly impedes the formation of dynamically gained chromatin loops induced by β3-AR signalling during thermogenesis, providing the genome-wide evidence that a histone variant is required for chromatin interaction reorganization. The presence of H2A.Z-independent loops suggests that additional factors likely contribute to β3-AR-induced chromatin loop formation (Extended Data Fig. 6e).

Given that dynamically gained chromatin loops after β3-AR stimulation are coupled with gene activation in the thermogenic programme (Fig. 1d,e), we next asked whether the reduction in dynamically gained loop formation due to H2A.Z knockdown impacts gene activation. We observed that the attenuation of E-P loop formation by H2A.Z knockdown coincided with decreased expression and transcription of associated genes (Extended Data Fig. 6f). Of the 459 genes exhibiting reduced expression after H2A.Z knockdown (Fig. 2d), 300 were linked to promoter-anchored chromatin loops (Supplementary Table 4). Notably, the contact frequencies of these loops were substantially reduced by H2A.Z knockdown, with approximately 70% of the loops displaying a decreased contact frequency (Fig. 3c). A similar reduction in contact frequencies was also observed for promoter-anchored loops associated with genes showing decreased transcription after H2A.Z knockdown (Fig. 3d). These findings suggest that the decreases in gene expression and transcription resulting from H2A.Z knockdown are largely associated with weakened chromatin loop formation. Examination of Micro-C profiles at the *Ppargc1a* locus confirmed this effect (Fig. 3e). The β3-AR stimulation-upregulated E-P loop associated with *Ppargc1a* was attenuated by H2A.Z knockdown, accompanied by reduced *Ppargc1a* expression and transcription in response to β3-AR stimulation (Fig. 3e). Similarly, H2A.Z knockdown also diminished the contact frequency of E-P interaction at the *Ucp1* locus, coinciding with decreased *Ucp1* expression and transcription (Extended Data Fig. 6g).

Beyond promoter-anchored genes, we also observed that β3-AR stimulation-upregulated E-P loops were coupled with increased enhancer RNA (eRNA) transcription (Extended Data Fig. 6h). Conversely, attenuation of these loops after H2A.Z knockdown was accompanied by a decreased level of these bidirectionally transcribed eRNAs (Extended Data Fig. 6h), as exemplified at the *Ucp1* locus (Extended Data Fig. 6i).

Taken together, these findings demonstrate that H2A.Z is primarily required for the formation of dynamically gained loops after β3-AR stimulation in brown adipocytes. Its knockdown largely attenuates

dynamic loop formation, coupled with impeded gene activation in the thermogenic programme, thereby inhibiting the thermogenic activity of brown adipocytes.

H2A.Z-enhanced chromatin accessibility is coupled with increased chromatin loop formation after β3-AR stimulation

Next, we sought to elucidate how H2A.Z is associated with the formation of dynamically gained loops in response to β3-AR stimulation. Given that H2A.Z incorporation mediates nucleosome rearrangement and dynamics[28,34], we hypothesized that β3-AR stimulation-induced H2A.Z deposition increases chromatin accessibility at loop anchors, thus facilitating the recruitment of looping mediators to support dynamic loop formation. To test this hypothesis, ATAC-seq was performed to assess chromatin accessibility under different conditions. We observed that over 70% of the identified H2A.Z ChIP–seq peaks overlapped with ATAC-seq peaks in β3-AR-stimulated control adipocytes (Fig. 4a), indicating that H2A.Z signals were highly associated with open chromatin regions. After positioning the H2A.Z signals based on the overlapped ATAC-seq peaks, we observed that H2A.Z signals formed well-positioned peaks, flanking the open chromatin regions (Fig. 4b). Furthermore, the open chromatin regions marked by H2A.Z exhibited higher DNA accessibility, as evidenced by greater ATAC-seq signals compared to those in the non-H2A.Z-overlapped regions (Fig. 4c).

To assess whether H2A.Z supports β3-AR stimulation-induced chromatin loop formation by modulating chromatin accessibility, we examined H2A.Z-dependent loops that were upregulated after β3-AR stimulation but weakened by H2A.Z knockdown (Fig. 3b). In response to β3-AR stimulation, these loops exhibited increased DNA accessibility at their H2A.Z-occupied loop anchors (Fig. 4d). This increment was attenuated by H2A.Z knockdown, coinciding with reduced loop strength (Fig. 4d), suggesting a high concordance between the changes in chromatin accessibility and the changes in loop strength. Similar findings were also observed for H2A.Z-occupied E-P loops (Extended Data Fig. 7a). Examination of ATAC-seq and chromatin loops at the *Ppargc1a* and *Pde4d* loci confirmed these effects, that is, differential chromatin accessibility was positively coupled with differential loop contact frequencies (Extended Data Fig. 7b). Over 60% of H2A.Z-dependent E-P loops and approximately 50% of P-P loops showed H2A.Z binding at their anchors, with increased signal after β3-AR stimulation (Extended Data Fig. 7c,d). Consistent with this, more than 70% of H2A.Z-occupied loops were promoter-anchored loops (Extended Data Fig. 7e). Around 44% of H2A.Z-dependent loops lacking direct H2A.Z occupancy were connected to H2A.Z-occupied loops and showed coordinated interaction changes (Extended Data Fig. 7f).

We next aimed to identify looping mediators whose recruitment is facilitated by H2A.Z-enhanced chromatin accessibility to strengthen loop formation after β3-AR stimulation. We first assessed the involvement of CTCF and cohesin complex, given their well-established roles in chromatin loop formation and maintenance[14]. To this end, we performed ChIP–seq for CTCF and SMC1, a component of the cohesin complex, in brown adipocytes with or without β3-AR stimulation. To our surprise, their overall occupancy at H2A.Z-occupied anchors remained largely unchanged after β3-AR stimulation (Extended Data Fig. 7g). We found that CTCF and SMC1 were less enriched at the anchors of β3-AR stimulation-upregulated loops compared to unchanged loops in β3-AR-stimulated brown adipocytes (Extended Data Fig. 7h). Their occupancy was also generally lower at upregulated loop anchors (Extended Data Fig. 7i). Although the functional importance of this difference remains unclear[35], these observations suggest the distinct features between dynamically gained and unchanged loops.

Growing evidence indicates that the Mediator complex bridges chromatin interactions in multiple biological systems[36,37]. Harms et al.[38] demonstrated that MED1, a Mediator subunit, is involved in determining BAT identity. These findings prompted us to assess whether H2A.Z facilitates Mediator recruitment to loop anchors to promote chromatin loop formation during thermogenesis. To test this, we performed ChIP–seq for MED1 and found that 47.1% of H2A.Z-occupied E-P loops, 25.7% of P-P loops and 20.6% of P-O loops exhibited MED1 binding at their anchors. Notably, MED1 occupancy at H2A.Z-occupied anchors increased after β3-AR stimulation (Fig. 4e). Correlation analysis revealed that, in response to β3-AR signalling, increased MED1 occupancy was positively associated with enhanced chromatin accessibility (Fig. 4f). Conversely, H2A.Z knockdown reduced MED1 occupancy after stimulation, positively correlated with decreased ATAC-seq signals (Fig. 4g). These concordant changes in chromatin accessibility and MED1 recruitment were exemplified at the *Ucp1* locus (Fig. 4h). Furthermore, knockdown of MED1 in brown adipocytes led to impaired E-P loop formation at the *Ucp1* locus and decreased *Ucp1* expression following β3-AR stimulation (Fig. 4i,j). A similar reduction in *Ucp1*-associated E-P loop formation was also observed in $p18^{Hamlet}$ knockdown brown adipocytes after β3-AR stimulation (Extended Data Fig. 7j).

Altogether, these findings indicate that β3-AR signalling induces dynamic loop formation, in part by promoting H2A.Z nucleosome deposition, which enhances DNA accessibility at loop anchors. Our proof-of-principle evidence further suggests that increased chromatin accessibility facilitates the recruitment of the Mediator complex, thereby contributing, at least partially, to the formation of dynamically gained loops during thermogenesis (Fig. 4k). That said, our model does not exclude alternative mechanisms, including a potential role for H2A.Z in modulating enhancer activity (Extended Data Fig. 7k–m).

H2A.Z plays an essential role in the thermogenic function of BAT

To assess the in vivo physiological importance of the above findings, we generated BAT-specific H2A.Z-deficient mice using a combination of Cre-lox and CRISPR–Cas9 technology[39] (Fig. 5a). Specifically, the adeno-associated virus (AAV) expressing a gRNA targeting H2A.Z was administered into the BAT of mice generated by crossing conditional Cas9 knock-in mice with those expressing Ucp1-driven Cre (Fig. 5a). The Ucp1-Cre line was chosen due to high levels of *Ucp1* expression in brown adipocytes. As a control, a non-targeting gRNA was used (Fig. 5a). The effective genome editing at the expected sites was confirmed for four individual gRNAs targeting H2A.Z, with gRNA2 selected for subsequent experiments due to its high specificity (Extended Data Fig. 8a). The reduction in H2A.Z in BAT was observed at both the mRNA and protein levels (Fig. 5b). We then examined the metabolic phenotypes of H2A.Z-deficient mice (Fig. 5c). Female control and H2A.Z-deficient mice had the same body weight and percentages of body fat (Extended Data Fig. 8b,c). The two groups also displayed comparable levels of food intake as well as fasting glucose and insulin levels (Extended Data Fig. 8d,e). We next exposed the control and H2A.Z-deficient mice to acute cold exposure (5 °C), a condition where the sympathetic nervous system is activated, leading to the release of noradrenaline to stimulate β3-AR signalling in brown adipocytes for heat production[5]. Notably, H2A.Z-deficient mice exhibited impaired cold tolerance, as revealed by lower body temperature during cold challenge (Fig. 5d), demonstrating the essential role of H2A.Z in maintaining body temperature in response to β3-AR activation in vivo. Furthermore, the reduction of H2A.Z in BAT decreased its maximal thermogenic capacity (Fig. 5e and Extended Data Fig. 8f). That is, in response to noradrenaline stimulation, H2A.Z-deficient mice exhibited lower levels of energy expenditure and oxygen consumption (Fig. 5e and Extended Data Fig. 8f). Collectively, these results substantiate the critical role of H2A.Z in mediating the thermogenic capacity of BAT in response to β3-AR stimulation in mice. Moreover, H2A.Z-deficient mice showed impaired glucose tolerance and reduced insulin sensitivity compared to control mice (Fig. 5f,g), suggesting that H2A.Z is involved in the regulation of systemic metabolism. Similar phenotypes were also

https://doi.org/10.1038/s42255-026-01510-2

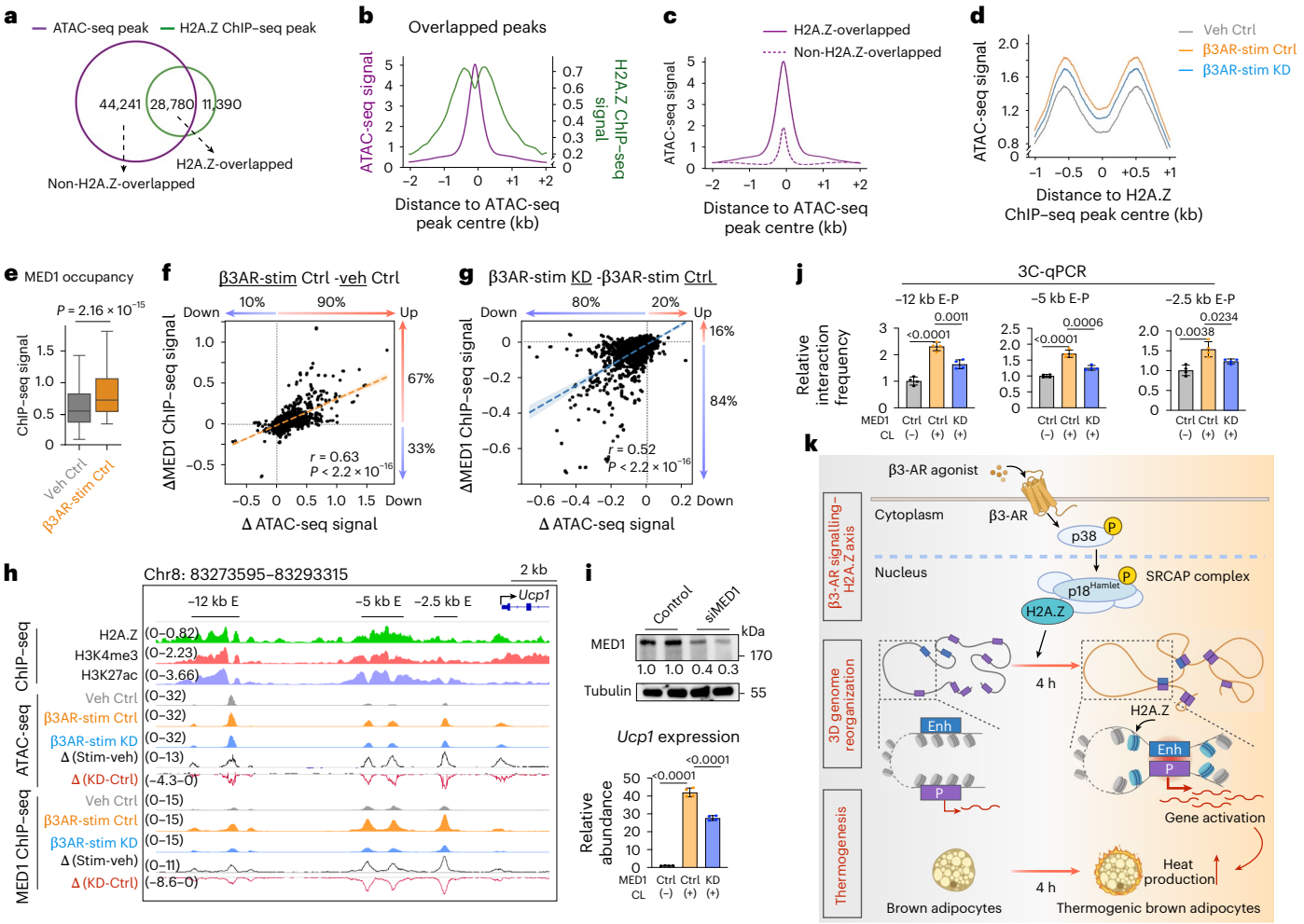

Fig. 4 | H2A.Z-enhanced chromatin accessibility is coupled with increased chromatin loop formation after β3-AR stimulation. a, Venn diagram showing the overlap between H2A.Z ChIP–seq peaks and ATAC-seq peaks in β3-AR-stimulated control adipocytes. **b**, Composite plot showing the averaged ATAC-seq (left *y* axis, purple line) and H2A.Z ChIP–seq (right *y* axis, green line) signals at overlapping peaks, centred on ATAC-seq peak summits. **c**, Composite plot depicting averaged ATAC-seq signals overlapped with H2A.Z peaks (solid purple line) or not overlapped with H2A.Z peaks (dashed purple line) in β3-AR-stimulated control adipocytes. **d**, Composite plot showing the averaged ATAC-seq signals at H2A.Z-occupied anchors of dependent loops across different conditions: vehicle-treated control (grey), β3-AR-stimulated control (orange) and β3-AR-stimulated H2A.Z KD (blue) adipocytes. ATAC-seq signals are shown in the ±1-kb region flanking H2A.Z peak centres. **e**, Box plot showing MED1 ChIP–seq signal intensities at H2A.Z-occupied anchors of dependent loops. *P* value, two-sided Wilcoxon test. Box plot shows the median (centre line), 25–75th percentiles (box) and 1.5 times the IQR (whiskers). **f**, Scatterplot showing the distribution of delta ATAC-seq signals (Δ ATAC-seq signal) against delta MED1 ChIP–seq signals (Δ MED1 ChIP–seq signal) at H2A.Z-occupied anchors of dependent loops after β3-AR stimulation. Positive values indicate increased signal after β3-AR stimulation. Pearson correlation coefficient (*r*) and two-sided *P* value were computed using the Python SciPy.stats.pearsonr function. The error band is the 95% confidence interval of the estimated regression mean in the regplot function in the seaborn Python package. **g**, Scatterplot showing the distribution of delta ATAC-seq signals (Δ ATAC-seq signal) against delta MED1 ChIP–seq signals (Δ MED1 ChIP–seq signal) at H2A.Z-occupied anchors of dependent loops after H2A.Z knockdown (β3AR-stim KD). Negative values indicate decreased signal mediated by H2A.Z knockdown. *r*, two-sided *P* value and error band were defined in the same way as in **f**. **h**, A representative example (*Ucp1* locus) showing coordinated changes in ATAC-seq and MED1 ChIP–seq signals in vehicle-treated control (grey), β3-AR-stimulated control (orange) and β3-AR-stimulated H2A.Z KD (blue) adipocytes. The promoter and three upstream enhancer regions (−12 kb, −5 kb, and −2.5 kb) are annotated with H3K4me3 and H3K27ac ChIP–seq tracks. Data were visualized using Integrative Genomics Viewer (IGV), and shown from one of two or three biological replicates with similar results. Differential (delta, Δ) tracks were generated using IGV subtract function: black Δ tracks represent β3AR-stim Ctrl minus veh Ctrl (stim-veh); red Δ tracks represent β3AR-stim KD minus β3AR-stim Ctrl (KD-Ctrl). **i**, Top: MED1 protein levels in the control and MED1 knockdown (siRNA targeting *Med1*, siMED1) adipocytes. The relative abundance of MED1 protein was determined using ImageJ, normalized to each corresponding Tubulin signal and the first control sample (set as 1.0), and labelled underneath. Bottom: *Ucp1* expression in control (Ctrl) and MED1 knockdown adipocytes following vehicle or 1 μM CL316,243 treatment for 4 h. *N* = 4 technical replicates per group. **j**, 3C-qPCR analysis of three *Ucp1*-associated E-P loops in control and MED1 knockdown adipocytes following vehicle or 1 μM CL316,243 treatment for 4 h. Interaction frequencies were normalized to the interaction frequency between two consecutive HindIII fragments at the *Rplp0* locus. *N* = 4 technical replicates per group. **k**, A model illustrating the β3-AR signalling–SRCAP complex–H2A.Z deposition–chromatin accessibility–loop-formation pathway underlying gene activation during thermogenesis. In **i** and **j**, the data shown are from one of two biological replicates with similar results, and error bars indicate the mean ± s.d. of technical replicates in each group. Differences were assessed with a two-sided unpaired *t*-test. Icon in **k** created in BioRender; Tseng, Y. https://biorender.com/iu0x6dt (2026).

https://doi.org/10.1038/s42255-026-01510-2

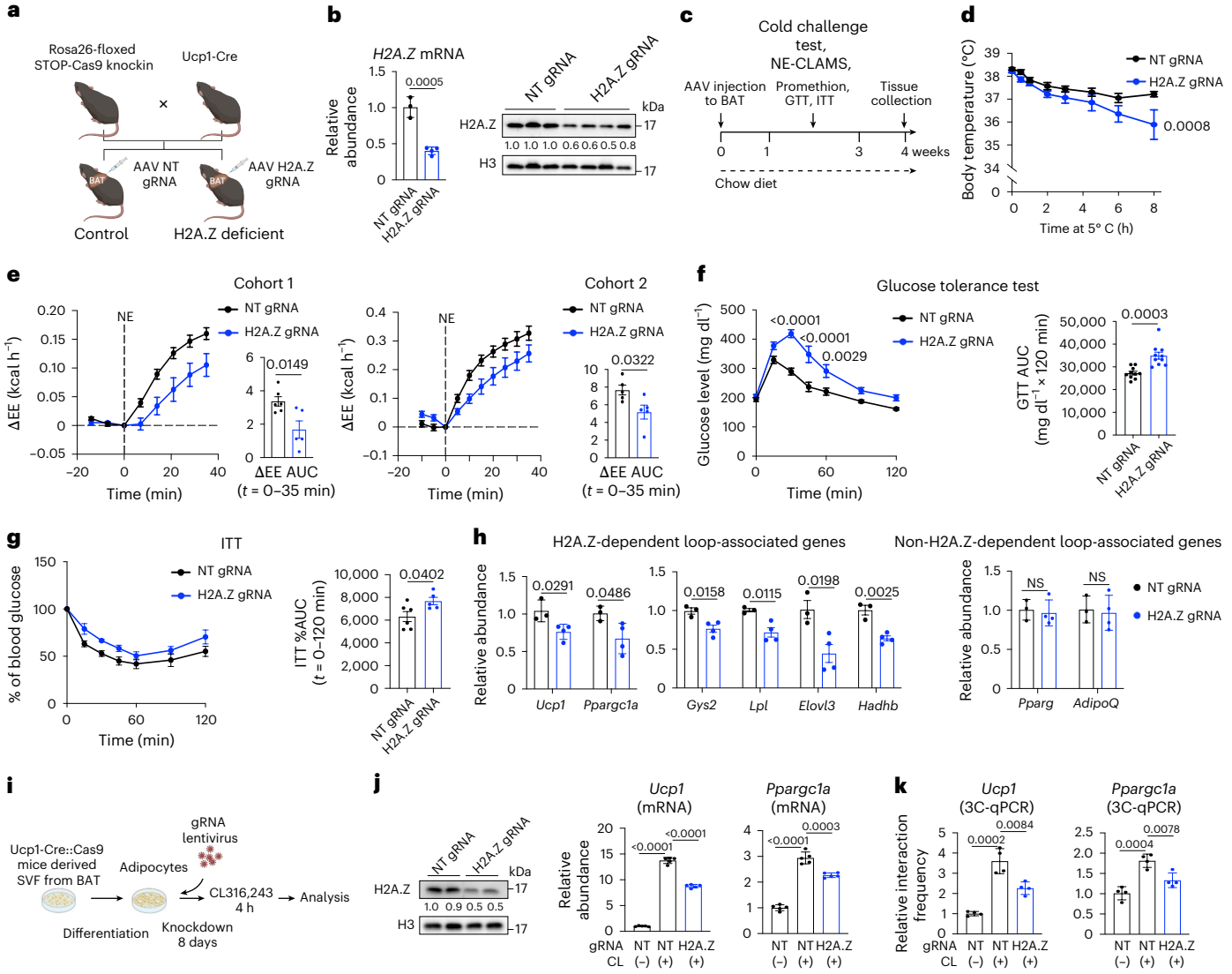

Fig. 5 | H2A.Z reduction impedes the thermogenic function of BAT. **a**, Schematic showing the generation of BAT-specific H2A.Z-deficient mice using a combination of Cre-lox and CRISPR–Cas9 technology. Rosa26-floxed STOP-Cas9 knock-in mice were crossed with Ucp1-Cre mice to enable BAT-specific Cas9 expression. AAVs expressing a non-targeting (NT) gRNA or a gRNA targeting H2A.Z were then injected into both lobes of BAT to generate control or BAT-specific H2A.Z-deficient mice. **b**, H2A.Z expression and protein level in control and H2A.Z-deficient mice. The relative abundance of H2A.Z protein was determined using ImageJ, normalized to each corresponding H3 signal and the first NT gRNA sample (set as 1.0), and labelled underneath. $N = 3$ mice for NT gRNA group and $n = 4$ for H2A.Z gRNA group. **c**, Experimental design for metabolic phenotyping of chow-fed control and H2A.Z-deficient mice. NE, noradrenaline; CLAMS, Comprehensive Lab Animal Monitoring System; Promethion, Sable Systems' Promethion system; GTT, glucose tolerance test; ITT, insulin tolerance test. **d**, The core body temperature of the female control and H2A.Z-deficient mice that were challenged at 5 °C for 8 h. $N = 12$ mice per for NT gRNA group and $n = 11$ mice for H2A.Z gRNA group, combined from two cohorts. **e**, Energy expenditure (EE) measured by indirect calorimetry in female control and H2A.Z-deficient mice that were stimulated with an intraperitoneal (i.p.) injection of noradrenaline (1 mg per kg body weight). The bar plot shows the quantification of the area under the curve (AUC). Left: EE was measured using CLAMS. $N = 6$ mice for NT gRNA group and $n = 5$ for H2A.Z gRNA group. Right: EE was measured using a Sable Systems' Promethion system. $N = 5$ mice per group. **f**, GTT results for the female control and H2A.Z-deficient mice. Bar plot showing the quantification of the AUC. $N = 10$ mice per group, combined from two cohorts. **g**, ITT results for the female control and H2A.Z-deficient mice. Bar plot showing the quantification of the percentage AUC. $N = 6$ mice for NT gRNA group and $n = 5$ for H2A.Z gRNA group. **h**, Expression of H2A.Z-dependent loop-associated genes and non-H2A.Z-dependent loop-associated genes in BAT from female control and H2A.Z-deficient mice that were challenged at 5 °C for 8 h before tissue collection. $N = 3$ mice for NT gRNA group and $n = 4$ mice for H2A.Z gRNA group. **i**, Schematic of H2A.Z knockdown via gRNA lentivirus in primary brown adipocytes derived from stromal vascular fraction (SVF) isolated from BAT of Ucp1-Cre::Cas9 mice. A non-targeting gRNA was used as control. **j**, Left: H2A.Z protein levels in control (NT gRNA) and H2A.Z knockdown (H2A.Z gRNA) primary adipocytes. The relative abundance of H2A.Z protein was determined using ImageJ, normalized to each corresponding H3 signal and the first NT gRNA sample (set as 1.0), and labelled underneath. Right: expression of *Ucp1* and *Ppargc1a* in control (NT gRNA) and H2A.Z knockdown (H2A.Z gRNA) primary brown adipocytes following vehicle or 1 μM CL316,243 treatment for 4 h. $N = 5$ technical replicates per group for RT–qPCR. **k**, 3C-qPCR analysis of E-P loops associated with *Ucp1* or *Ppargc1a* in control (NT gRNA) and H2A.Z knockdown (H2A.Z gRNA) primary adipocytes following vehicle or 1 μM CL316,243 treatment for 4 h. Interaction frequencies were normalized to the interaction frequency between two consecutive HindIII (*Ucp1*) or NdeI (*Ppargc1a*) fragments at the *Rplp0* locus. $N = 4$ technical replicates per group for qPCR. In **b** and **h**, error bars in bar plots indicate the mean ± s.d. of biological replicates in each group. In **d**–**g**, error bars indicate the mean ± s.e.m. of biological replicates in each group. In **j** and **k**, the data shown are from one of two biological replicates with similar results, and error bars indicate the mean ± s.d. of technical replicates in each group. For the line charts in **d**–**g**, statistical analysis was performed using a two-way analysis of variance (ANOVA). For the bar plots in **b**, **e**–**h**, **j** and **k**, differences were assessed with a two-sided unpaired *t*-test. *P* value > 0.05. Icons in **a** and **i** created in BioRender; Tseng, Y. https://biorender.com/iu0x6dt (2026).

detected in the male H2A.Z-deficient mice (Extended Data Fig. 8g–n), indicating that H2A.Z plays a key role in the thermogenic functions of BAT in both sexes.

We next evaluated the role of H2A.Z in regulating gene expression in vivo. In line with the effects of H2A.Z knockdown in in vitro differentiated brown adipocytes, after cold exposure, reduction of H2A.Z in BAT decreased the expression of H2A.Z-dependent loop-associated genes, such as genes involved in thermogenesis (*Ucp1* and *Ppargc1a*), as well as genes involved in fuel utilization (*Gys2*, *Lpl*, *Elovl3* and *Hadhb*; Fig. 5h). Reduction of H2A.Z had no detectable impact on the expression of non-H2A.Z-dependent loop-associated genes, such as the adipogenic markers *Pparg* and *Adipoq* (Fig. 5h). A similar effect of H2A.Z knockdown on *Ucp1* and *Ppargc1a* expression was also observed in primary brown adipocytes (Fig. 5i,j). Notably, these gene expression changes were positively correlated with alterations in the associated E-P loops (Fig. 5k). Taken together, these results highlight the essential role of H2A.Z in regulating thermogenic gene expression in vivo in response to β3-AR signalling.

H2A.Z strengthens dynamically gained chromatin loops during thermogenesis in primary human brown adipocytes

To expand our understanding of chromatin looping during thermogenesis and to investigate the involvement of H2A.Z in dynamic loop formation in humans, we performed Micro-C assays in primary human brown adipocytes during the thermogenic programme and after H2A.Z knockdown (Fig. 6a). Thermogenesis was acutely activated (4 h) using forskolin (FSK), a natural compound that directly activates adenylate cyclase to mimic β3-AR stimulation[40]. RNA-seq analysis comparing vehicle-treated control and FSK-treated control human brown adipocytes revealed that FSK treatment upregulated genes involved in key brown adipocyte functions such as thermogenesis, glucose homeostasis and lipolysis (Extended Data Fig. 9a). Consistent with the regulatory role of H2A.Z in thermogenic gene activation in mice, H2A.Z knockdown in primary human brown adipocytes also led to downregulation of essential thermogenic pathways (Extended Data Fig. 9b,c). In line with gene expression changes, H2A.Z knockdown resulted in reduced mitochondrial activity and impaired glucose uptake in human brown adipocytes (Extended Data Fig. 9d,e).

Micro-C data from four highly reproducible replicates were pooled to analyse chromatin interactions in primary human brown adipocytes (Extended Data Fig. 9f), yielding ~1.1 billion valid read pairs per condition (Supplementary Table 5). Consistent with observations in mouse brown adipocytes, Micro-C analysis in human adipocytes revealed rapid chromatin loop reorganization following 4 h of FSK treatment, with 19,474 upregulated and 24,920 downregulated loops identified using the same criteria applied in the mouse data analysis (Fig. 6b and Supplementary Table 5). APA revealed that the upregulated loops exhibited a greater averaged contact signal in FSK-treated brown adipocytes, whereas downregulated loops showed a lower averaged contact signal (Fig. 6b). To classify promoter-anchored loops, we defined active enhancers by integrating H3K27ac ChIP–seq data from primary human brown adipocytes with annotated enhancers from the ENCODE SCREEN in humans. Correlation analysis revealed that chromatin loops with increased contact frequency, particularly dynamically gained E-P loops, were associated with elevated expression of target genes during thermogenesis (Fig. 6c). Functional enrichment analysis revealed that these target genes were involved in key brown adipocyte functions such as thermogenesis and lipolysis (Fig. 6d). Taken together, these cross-species findings reveal consistent patterns of chromatin loop dynamics associated with thermogenic gene activation in both mouse and human brown adipocytes, establishing rapid loop reorganization as a core feature of thermogenesis.

To determine whether H2A.Z is also required for the formation of dynamically gained loops during thermogenesis in humans, we compared Micro-C data from FSK-treated control and H2A.Z knockdown primary human brown adipocytes (Fig. 6a). Notably, H2A.Z knockdown markedly attenuated the formation of FSK treatment-upregulated loops, with 59.6% of them identified as weakened loops after H2A.Z knockdown (Fig. 6e and Supplementary Table 5). In contrast, loops that were downregulated by FSK treatment were largely unaffected by H2A.Z knockdown (Extended Data Fig. 9g), suggesting a conserved role for H2A.Z in promoting loop formation instead of disruption during thermogenesis in both species. Moreover, integrative analysis of gene expression and chromatin loop changes revealed that the majority (74.3%) of loops associated with genes downregulated by H2A.Z knockdown exhibited reduced contact frequency in H2A.Z

Fig. 6 | Consistent chromatin loop dynamics in primary human brown adipocytes during thermogenesis. a, Schematic outlining the study system. Primary SVF isolated from human deep neck biopsy was differentiated into mature brown adipocytes. Thermogenesis was acutely activated (4 h) with 10 μM FSK. Micro-C was performed under vehicle-treated control (Veh_Ctrl), FSK-treated control (FSK_Ctrl) and FSK-treated H2A.Z knockdown (FSK_KD) conditions to determine chromatin loop changes during thermogenesis and the impact of H2A.Z knockdown. **b**, Left: violin plot showing contact frequencies of upregulated, downregulated and unchanged loops in FSK-treated (orange) versus vehicle-treated (grey) primary human brown adipocytes. Violin plot shows median (dot), 25–75th percentiles (box) and 1.5 times the IQR (whiskers). Right: averaged contact signals (APA) plotted with loops sorted by Up, Down or No categories. **c**, Rank-ordered distribution of delta loop contact frequency (Δ contact frequency) against gene expression changes ($\log_2$FC) for the E-P, P-P and P-other loops after FSK treatment. The associated gene for each high-confidence P-anchored loop was determined by the identification of the TSS located ±5 kb around the loop anchor. The distribution of $\log_2$FC in gene expression for each loop type was smoothed by LOESS regression. The error bands indicate the fitted curve ± s.e.m. with a 95% confidence interval. **d**, Functional enrichment analysis for upregulated genes associated with dynamically gained promoter-anchored loops in response to FSK treatment. Selected brown adipocyte-related terms are shown. The *x* axis shows the statistical significance ($-\log_2$ adjusted *P* value, $-\log_2(P_{adj})$). GSEA was performed using Enrichr (one-sided Fisher's exact test with Benjamini–Hochberg correction). **e**, Left: violin plot showing contact frequencies of FSK treatment-upregulated loops ($n = 19{,}474$) across three conditions. Violin plot shows median (dot), 25–75th percentiles (bar) and 1.5 times the IQR (whiskers). Middle: averaged contact signals (APA) plotted for FSK treatment-upregulated loops in the FSK-treated contro and FSK-treated H2A.Z knockdown adipocytes. Right: bar plot showing the percentage of weakened (Weaken) and unaffected (Stable) loops after H2A.Z knockdown. **f**, Distribution of delta contact frequencies (Δ contact frequency) of promoter-anchored loops associated with genes exhibiting decreased expression after H2A.Z knockdown with FSK treatment. Loops with negative delta values displayed decreased contact frequencies after H2A.Z knockdown. **g**, Snapshots of Micro-C contact maps comparing chromatin interactions at the *FABP5* locus in the vehicle-treated control, FSK-treated control and FSK-treated H2A.Z knockdown human brown adipocytes. Gene annotations are shown at the top (exons in dark green). RNA-seq data showing gene expression levels in the same region of contact maps, displayed below gene annotation. The RNA-seq data shown are from one of three biological replicates with similar results. Bar plot on the right showing the fold change in *FABP5* expression quantified by RNA-seq. Error bar represents the mean ± s.d. of three biological replicates in each condition. P_{adj} value, two-sided Wald test. The black bar in the RNA-seq track from FSK_Ctrl adipocytes annotates the enhancer region, and *FABP5*-associated E-P loop is highlighted by a black arched line. E-P loops in the contact maps are highlighted by circles. Micro-C contact maps and RNA-seq tracks were visualized using Juicebox software. **h**, Correlation between *ACTR6* or *VPS72* and BMI in human abdominal subcutaneous white adipose tissue (scWAT; $n = 770$). Correlations were assessed using two-sided Spearman's rank correlation; Spearman's *r* and *P* values are shown. **i**, Fold enrichment of the number of GWAS SNPs that overlap with H2A.Z-occupied anchors of dependent loops over that of non-trait-associated SNPs. SNP enrichment was determined using a one-sided Fisher's exact test with Benjamini–Hochberg correction. Icon in **a** created in BioRender; Tseng, Y. https://biorender.com/iu0x6dt (2026).

https://doi.org/10.1038/s42255-026-01510-2

knockdown adipocytes (Fig. 6f). Their associated genes were involved in critical brown adipocyte functions such as thermogenesis, glucose homeostasis and lipolysis (Extended Data Fig. 9h). The *FABP5* locus exemplified the concordance between chromatin looping and gene expression changes during thermogenesis and after H2A.Z knockdown in primary human brown adipocytes (Fig. 6g). *FABP5* encodes fatty acid binding protein 5, which plays a role in thermogenesis by regulating lipid metabolism[41]. Micro-C heat maps revealed a ~70-kb E-P loop connecting a downstream enhancer to the *FABP5* promoter, with increased contact frequency after FSK treatment and was accompanied by elevated *FABP5* expression (Fig. 6g). Whereas, H2A.Z knockdown attenuated the formation of this E-P loop, along with reduced *FABP5* expression (Fig. 6g). These results define a cross-species conserved role for H2A.Z in supporting dynamic loop formation and thermogenic gene activation in both human and mouse brown adipocytes.

Overall, we observed consistent patterns of chromatin loop dynamic changes and their association with gene activation during thermogenesis in both human and mouse brown adipocytes. This prompted us to investigate whether the identified chromatin loops are evolutionarily conserved. To address this, we identified shared chromatin loops between mouse and human brown adipocytes using AdaLiftOver, a computational tool that integrates both sequence and epigenomic similarities[42]. We found that 57.1% of the mouse loops identified using the LiftOver tool were conserved in human brown adipocytes (Supplementary Table 6). Functional enrichment analysis showed that the genes associated with conserved promoter-anchored loops were involved in thermogenesis, regulation of lipolysis, glucose homeostasis and fatty acid metabolic process (Extended Data Fig. 9i).

Next, we explored the potential link between H2A.Z and human obesity. No obesity-associated genetic variants (single-nucleotide polymorphisms or SNPs) were detected in the H2A.Z coding region. We then investigated whether H2A.Z nucleosome deposition might influence body weight. Analysis of microarray data from abdominal subcutaneous adipose tissue in 770 individuals with varying BMI[43] revealed a negative correlation between BMI and the expression of genes encoding H2A.Z loading machinery subunits, including *ACTR6* (ARP6) and *VPS72* (YL1; Fig. 6h). This finding suggests that H2A.Z nucleosome deposition may have a potential impact on body weight in humans.

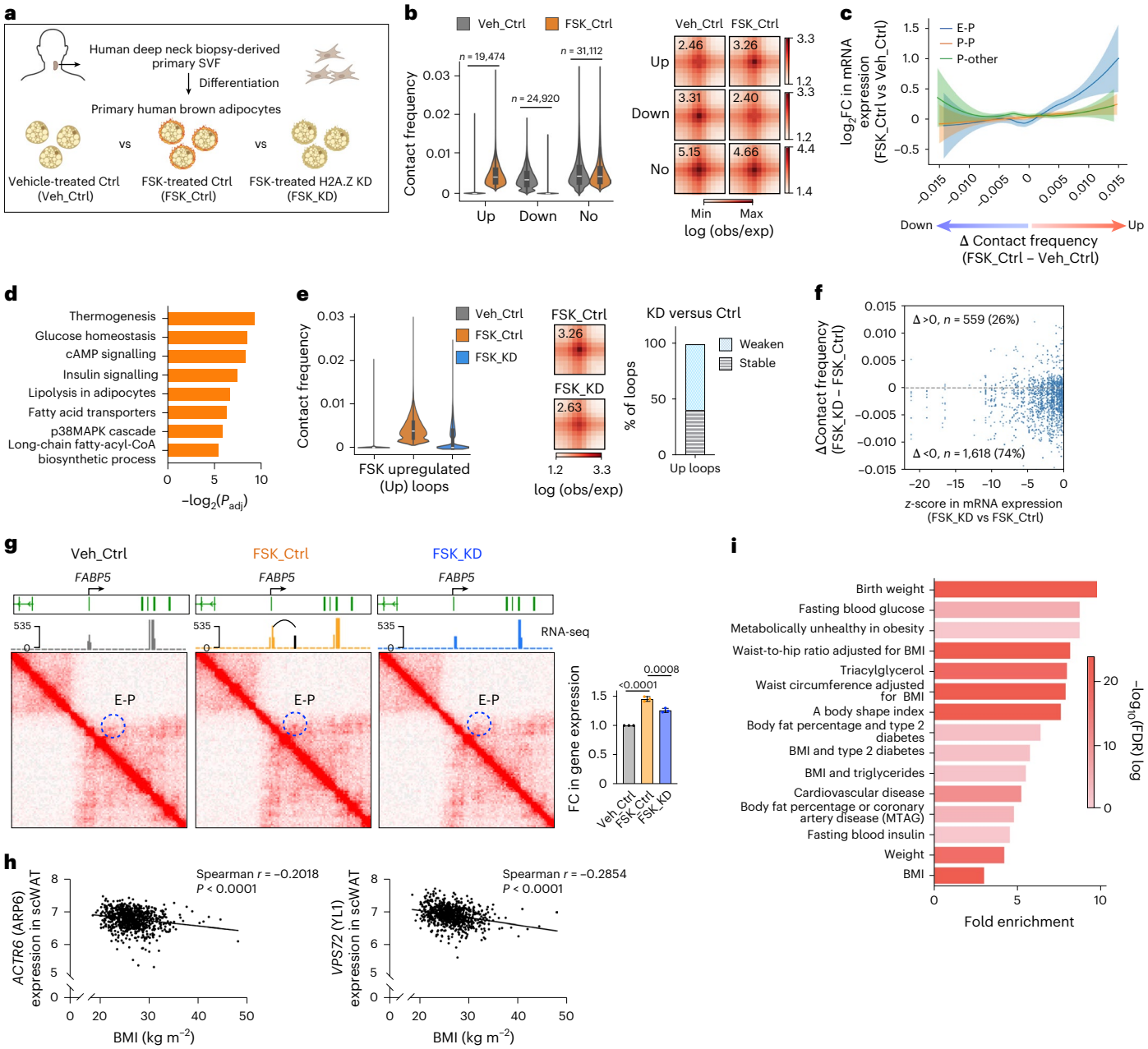

Lastly, we explored whether our unique datasets could help elucidate the genetic basis of obesity, given the tight association between brown fat activity and obesity. As most SNPs associated with complex traits identified by GWASs are located in non-coding regions of the genome, chromatin loop analysis may hold promise in understanding their target genes. Integration of publicly available GWAS datasets with our Micro-C maps from primary human brown adipocytes revealed that SNPs associated with obesity and its related metabolic disorders were enriched at anchors of H2A.Z-occupied loops (Fig. 6i). Approximately half of these SNPs reside in the non-promoter anchors. These findings suggest that H2A.Z-occupied chromatin loops may help elucidate the regulatory targets of these SNPs and are potentially relevant for these SNP-associated metabolic traits.

Discussion

The rising prevalence of obesity and its comorbidities is a major global health concern. BAT plays a crucial role in energy expenditure, fatty acid metabolism and glucose homeostasis, making it an appealing therapeutic target. Understanding the mechanisms that regulate BAT activity could provide insights into obesity pathophysiology and uncover therapeutic targets for obesity-related metabolic diseases. Our study presents the cross-species, high-resolution maps of 3D genome dynamics during adaptive thermogenesis, profiling both mouse and primary human brown adipocytes (Figs. 1 and 6). We show that rapid reorganization of chromatin loops is an evolutionarily conserved phenomenon tightly coupled to the transcriptional activation of thermogenic genes in humans and mice (Figs. 1d,e and 6c), suggesting loop reorganization as a fundamental feature of thermogenesis. The multi-omics resource of our study provides a unique and integrative view of the transcriptomic and epigenomic landscape of thermogenic adipocytes. This enabled the discovery of *cis*-regulatory elements (that is, enhancers for thermogenic genes; Figs. 1g–j and 6g), expanding the catalogue of functional elements controlling energy metabolism and offering targets for further investigations into the molecular mechanisms underlying thermoregulation.

The analyses of Micro-C data from both mouse and human brown adipocytes exposed to a mere 4-h β3-AR stimulation reveal rapid changes of chromatin loops, with ~50% of loops exhibiting altered strength (Figs. 1b and 6b). These findings uncover the remarkable plasticity of the 3D genome in response to acute hormonal signalling, establishing a biological paradigm: loop reorganization as a rapid, hormone-responsive feature layer in energy metabolism. Importantly, our results reveal a positive correlation between dynamically gained loops and the activation of genes implicated in thermogenesis (Figs. 1d–f and 6c,d). However, this concordant relationship is not observed for dynamically lost loops and their associated genes (Figs. 1d,e and 6c). This discrepancy parallels the findings of previous studies in cellular differentiation[35,44], highlighting the specificity of chromatin loop changes in driving cellular programmes.

Although transcription factors and architectural proteins are known to contribute to chromatin loop formation and maintenance, our data unveil an additional pathway for the classic β3-AR hormonal signalling. Contrary to the conventional mechanism that centres on direct activation of transcription factors, our findings reveal a distinct route involving the histone variant H2A.Z. Specifically, we identify a non-canonical axis, β3-AR → SRCAP complex → H2A.Z → chromatin accessibility → loop formation, that connects hormonal signalling to 3D genome reorganization (Figs. 2h–n and 4). Our study provides the genome-wide evidence that a histone variant is required for strengthening chromatin interactions. As a histone variant, H2A.Z is unlikely to function as a canonical looping factor that directly mediates chromatin loop formation; instead, our observations suggest that H2A.Z is associated with a permissive chromatin environment. Our data further demonstrate that the recruitment of the Mediator complex to loop anchors is facilitated by H2A.Z (Fig. 4e–j), expanding the current understanding of how chromatin accessibility is translated into higher-order genome architecture. Interestingly, H2A.Z depletion reduces the dynamically gained loops but leaves the dynamically lost loops unaffected, revealing an asymmetric role in loop dynamic changes. Together, the discovery that the β3-AR–SRCAP–H2A.Z axis modulates chromatin looping reveals a cross-species conserved dimension of hormone-responsive genome regulation.

We present a model in which H2A.Z contributes to the formation of dynamically gained loops by enhancing chromatin accessibility at loop anchors (Fig. 4k). That said, our model does not exclude alternative mechanisms. H2A.Z may also be involved in the strengthening of chromatin interactions by modulating enhancer activity. H3K27ac, a mark of active enhancers, has been shown to positively correlate with chromatin loop dynamics in some biological contexts[45]. To test this possibility in our system, we analysed H3K27ac ChIP–seq data from mouse brown adipocytes with or without β3-AR stimulation. We observed a subtle but statistically significant increase in H3K27ac occupancy at enhancer anchors of H2A.Z-occupied loops after stimulation (Extended Data Fig. 7k). A subset (24%) of these E-P loops showed upregulated H3K27ac signals (Extended Data Fig. 7l), which was decreased after H2A.Z knockdown (Extended Data Fig. 7m), coinciding with the observed loop dynamics. Overall, our study delineates one mechanism by which H2A.Z is involved in loop formation by enhancing chromatin accessibility at loop anchors. However, this mechanism is not necessarily mutually exclusive with other mechanisms; instead, they might function simultaneously and cooperatively.

Our study provides mechanistic insight into how H2A.Z contributes to the formation of H2A.Z-occupied loops. However, a proportion of H2A.Z-dependent loops lack direct H2A.Z occupancy, a phenomenon less common in promoter-anchored loops (Extended Data Fig. 7c,e). This aligns with the predominant localization of H2A.Z at enhancers and promoters[28]. Similar indirect effects have been reported in other biological systems[46]. One possible explanation involves the presence of interconnected chromatin interactions[17,35], where depletion of core regulators disrupts looping networks[47]. Supporting this, we found that loops connected to H2A.Z-occupied loops within networks exhibited similar interaction frequency changes, increasing after β3-AR stimulation but attenuated by H2A.Z knockdown (Extended Data Fig. 7f). These concordant changes were not observed in randomly selected control loops (Extended Data Fig. 7f). Approximately 44% of H2A.Z-dependent loops that lack direct H2A.Z occupancy were connected to H2A.Z-occupied loops. These findings highlight the complexity of 3D genome reconfiguration.

Given the tissue-specific and cell-type-specific nature of chromatin loops, it is essential to generate 3D genome maps in physiologically relevant systems to interpret the genetic basis of obesity pathogenesis. BAT is a central regulator of adaptive thermogenesis, and its dysfunction is tightly linked to obesity and metabolic disease. By obtaining primary human brown adipocytes from deep neck depots, a rare and valuable resource, we present the 3D genome maps in this physiologically relevant context. Integrative analysis of our Micro-C data from primary human brown adipocytes with publicly available GWAS data identified SNPs associated with obesity and related metabolic disorders are enriched in H2A.Z-occupied loops (Fig. 6i). This finding implies that H2A.Z-occupied chromatin loops may represent a mechanism through which genetic variants may influence the expression of target genes implicated in obesity and metabolic disorders, offering translational insights into the genetic basis of metabolic disease.

Methods

Mice

The Rosa26-floxed STOP-Cas9 knock-in mice (strain 26175) and Ucp1-Cre mice (strain 024670) were purchased from the Jackson Laboratory. Unless otherwise stated, mice were housed in a temperature-controlled environment (22 °C) with a 12-h light–dark

cycle and fed with chow diet (LabDiet, 5020). At the time of AAV injection, both male and female mice were 12–16 weeks of age. All experimental procedures involving animals were performed in compliance with all relevant ethical regulations applied to the use of small rodents, and with the approval by the Institutional Animal Care and Use Committee at the Joslin Diabetes Center.

Cell lines

Mouse brown preadipocytes (WT-1), generated from a female mouse using SV40 T antigen[48], were cultured in high-glucose DMEM with 10% FBS. For differentiation, confluent preadipocytes were treated for 2 days with induction medium supplemented with 10% FBS, 20 nM insulin, 1 nM triiodothyronine (T3), 0.125 mM indomethacin, 5 µM dexamethasone and 0.5 mM IBMX, followed by 4 days in differentiation medium with 2% FBS, 20 nM insulin and 1 nM T3. Medium was replaced every other day.

Primary human brown preadipocytes (B158) were isolated from the deep neck region as previously described[49]. The SVF was isolated from a 52-year-old male donor with normal BMI and no diabetes, malignant tumour or abnormal thyroid hormone levels at the time of thyroid surgery. Tissue collection was approved by the Medical Research Council of Hungary (20571-2/2017/EKU) followed by the EU Member States' Directive 2004/23/EC on presumed consent practice for tissue collection. All experiments were carried out in accordance with the approved ethical regulations and the guidelines of the Helsinki Declaration. Written informed consent was obtained from the participant before the surgical procedure. For differentiation, confluent preadipocytes were cultured for 21 days in DMEM/F-12 medium supplemented with 10% FBS, 33 µM biotin, 0.5 µM human insulin, 17 µM pantothenate, 0.1 µM dexamethasone, 2 nM T3, 500 µM IBMX, 30 µM indomethacin, 10 µg ml^{-1} transferrin and 1 µM rosiglitazone.

Human immortalized brown preadipocytes (A41), generated using human telomerase reverse transcriptase[50], were cultured in high-glucose DMEM with 10% FBS. Differentiation was performed as for primary human preadipocytes, except without transferrin and rosiglitazone.

RNA-seq and analysis

Total RNA from mouse adipocytes was isolated using Direct-zol RNA Miniprep kits (Zymo Research, R2050). Ribosomal RNA was depleted using the RiboCap rRNA Depletion Kit for Human/Mouse/Rat (LEXOGEN, 144), and libraries were prepared with the CORALL RNA-Seq V2 Library Prep Kit (LEXOGEN, 171). Three biological replicates were generated per condition and sequenced using a NextSeq 500 Instrument (Illumina). Total RNA from primary human brown adipocytes was isolated using the same kit. mRNA libraries were prepared and sequenced by Novogene using a NovaSeq X plus Instrument (Illumina).

The raw RNA-seq reads were trimmed using Trim Galore (version 0.6.6) and mapped to the genome (mm10 or hg38) using STAR[51] (version 2.7.9a). A gene-level read count matrix was generated using GENCODE gene annotations (version M23 for mouse and version 38 for human) and imported into DESeq2 (version 1.32.0)[52] for differential expression analysis with paired comparisons for three biological replicates. GSEA[53] was performed using the fgsea package[54] (version 1.18.0) in R, with KEGG pathway annotation[55] based on the $\log_2$ fold changes across all expressed genes, and the plots were generated using the gseapy package[56] (version 1.0.6).

PRO-seq and analysis

PRO-seq was performed as previously described[21]. Mouse brown adipocytes were washed and incubated on ice for 5 min in swelling buffer (10 mM Tris-HCl pH 8.0, 2 mM $MgCl_2$, 3 mM $CaCl_2$). Cells were scraped, filtered (100 µm) and pelleted, and then resuspended in buffer W (10 mM Tris-HCl pH 8.0, 5 mM $MgCl_2$, 10 mM KCl, 250 mM sucrose, 1 mM EGTA, 10% glycerol, freshly added 0.5 mM dithiothreitol (DTT) and RNase inhibitor). Cells were lysed with buffer W containing 0.5% NP-40 and 0.05% Tween-20 for 5 min on ice, filtered (40 µm), centrifuged and washed with buffer W. Pellets were resuspended in freezing buffer (50 mM Tris-HCl pH 8.0, 40% glycerol, 5 mM $MgCl_2$, 1.1 mM EDTA) supplemented with DTT and RNase inhibitor. Permeabilization was confirmed by Trypan blue staining. Aliquots of $1–2 \times 10^6$ permeabilized cells in 200 µl freezing buffer were snap-frozen in liquid nitrogen and stored at −80 °C. All subsequent steps were performed by the Nascent Transcriptomics Core at Harvard Medical School. Libraries were sequenced on an Illumina NovaSeq X Plus.

The PRO-seq data preprocessing was done by the Nascent Transcriptomics Core at Harvard Medical School. All custom scripts described herein are available on the AdelmanLab GitHub repository (https://github.com/AdelmanLab/NIH_scripts/). In brief, dual 6-nucleotide-long unique molecular identifiers (UMIs) were extracted and reads were adaptor-trimmed, UMI-trimmed and processed to preserve mate orientation before alignment to a combined mouse (primary) and *Drosophila* (spike-in) genome using Bowtie2, retaining properly paired reads. Reads were separated by genome, deduplicated with UMI-tools, and converted to strand-swapped 3′-end bedGraphs at single-nucleotide resolution, then normalized using DESeq2 size factors and merged across replicates. Filtered Ensembl (GRCm38.99) annotations were used to quantify PRO-seq signal from the TSS to +150 nucleotides, generate depth-normalized bigWigs and identify active TSSs with proTSScall, defining one dominant TSS per gene based on highest TSS-proximal signal. Reads were summed from the TSS to the transcription end site for each active gene, and differential expression was determined using DESeq2 (Wald test) with default size factors.

eRNA analysis was performed using 5′ PRO-seq signals as described previously[57]. eRNA peaks were called separately on forward and reverse strands with HOMER (v4.11.1), including an additional intergenic-only peak calling to recover promoter-proximal enhancers. Peaks overlapping annotated TSSs or gene bodies within ±2 kb, or with signal <0.2 reads per million, were removed. Peaks from both rounds were pooled and deduplicated. Convergent peaks within 1 kb were merged, defining the enhancer centre as the midpoint; otherwise, the centre was set 180 base pairs (bp) upstream of the peak in the direction of transcription. Enhancer activity was quantified using strand-specific PRO-seq signal within ±1 kb of enhancer centres, and average signals were calculated for intergenic enhancers.

Micro-C

Micro-C was performed using the Dovetail Micro-C kit (Dovetail Genomics, 21006) with modifications. Mouse brown adipocytes were crosslinked in PBS with 3 mM disuccinimidyl glutarate (DSG) for 10 min followed by 1% formaldehyde for 10 min at room temperature with rotation. Cells were pelleted (3,000*g*, 5 min), washed, resuspended in nuclease digest buffer and digested with an appropriate amount of MNase at 22 °C for 15 min. For primary human brown adipocytes, nuclei were isolated with lysis buffer (10 mM Tris-HCl pH 8.0, 10 mM NaCl, 1 mM $MgCl_2$, 0.1% NP-40, protease inhibitors), fixed with 3 mM DSG (35 min) and 1% formaldehyde (10 min), quenched with 375 mM Tris-HCl pH 7.5, and digested with an appropriate amount of MNase at 37 °C for 20 min in MNase buffer (10 mM Tris-HCl pH 7.5, 50 mM NaCl, 5 mM $MgCl_2$, 1 mM $CaCl_2$, 0.2% NP-40, protease inhibitors). MNase digestion was optimized to yield 40–70% mononucleosomes. The following steps were performed according to the manufacturer's protocol. Four biological replicates were generated for mouse samples and two biological replicates for human samples (each with two technical replicates). Mouse libraries were sequenced on an Illumina NextSeq 500, and human libraries were sequenced on an Illumina NovaSeq X Plus.

Micro-C data processing

The raw Micro-C sequencing reads were trimmed using Trim Galore (version 0.6.6) and mapped to the genome (mm10 or hg38) using BWA MEM[58] (version 0.7.17-r1188). BAM files were imported into the

pairtools software to generate read pairs representing valid contacts between two chromatin regions. Read pairs from four replicates in each condition were merged for downstream analysis. Any read pairs with a mapping quality score of less than five and with distances shorter than 100 bp (for example, unligated mononucleosome) were excluded[20]. The resulting valid read pairs were converted into a contact matrix, stored in COOL files using the COOLER package[59] (version 0.9.1), or as an HIC file using the JUICER software[60] (version 1.22.01). Contact matrices were then normalized using iterative correction (ICE) in COOL files or Knight–Ruiz in HIC files. The reproducibility analysis of Micro-C replicates was performed using HiCRep[61] (version 0.2.6) on COOL files.

Chromatin loop analysis

Chromatin loops were identified from 5-kb-resolution Micro-C COOL files using Peakachu[19] (downloaded 14 July 2023) with pre-trained high-confidence models downloaded from their website (high-confidence.250million.5 kb.w6.pkl for the mouse, and the high-confidence.700million.5 kb.w6.pkl for the human), and applying a loop probability cut-off of 0.95 to remove low-confidence calls. To detect differential loops between conditions, we took the union of bins with probability > 0.95 in either condition and defined loops as differential if their probability scores changed by more than twofold. We then selected the most confident non-redundant results using the Peakachu pool function. To link loops with transcriptional regulation, we focused on loops with at least one anchor overlapping promoters (±5 kb from TSS) and classified them as enhancer–promoter, promoter–promoter or promoter–other using H3K27ac ChIP–seq data integrated with ENCODE SCREEN[62] enhancers and GENCODE (vM23) annotations. Loops were defined as H2A.Z-occupied loops if the anchors overlapped with H2A.Z ChIP–seq peaks. Loops were defined as CTCF-bound if both anchors overlapped with CTCF ChIP–seq peaks that were also co-bound by SMC1. Loops were defined as SMC1-bound if both anchors overlapped with SMC1 ChIP–seq peaks.

Compartment and TAD analysis

The A/B compartment analysis was performed using the cooltools package[63] (version 0.5.4) at 10-kb genomic resolution. Genes were assigned to the compartment region if the ±2-kb flanking region of the gene's TSS overlaps with the identified compartment region. Gene expression changes in $\log_2$ fold change were compared between A-to-B switched, B-to-A switched and stable compartments. The TADs were identified using the ArrowHead algorithm implemented in JUICER (version 1.22.01) at 5-kb, 10-kb and 100-kb genomic resolutions. Boundary strength analysis was performed with window sizes of 50 kb and 100 kb for boundary scanning, using the cooltools package (version 0.5.4). Boundaries were considered differential if the boundary strength changed by more than twofold between two conditions.

Functional enrichment analysis

Enrichr (https://maayanlab.cloud/Enrichr/)[64], an online GSEA tool, was used to perform functional enrichment analysis. WikiPathways, KEGG and GO Biological Process were applied to define terms.

3C-qPCR

3C-qPCR was performed as previously described[65]. Cells were crosslinked in PBS with 3 mM DSG (10 min) and 1% formaldehyde (10 min) at room temperature, quenched with 0.125 M glycine, washed and resuspended in 1× buffer 2 (NEB) containing 1% SDS (362 µl buffer + 38 µl SDS), and then incubated at 65 °C for 10 min. SDS was quenched with Triton X-100, and chromatin was digested overnight at 37 °C with 400 U restriction enzyme (HindIII for *Slc16a1* and *Ucp1* E-P loops; NdeI for *Ppargc1a*). Digestion was terminated with SDS and incubation at 65 °C for 30 min. Samples were diluted in ligation mix containing 372.5 µl of 20% Triton X-100, 375 µl of 1 M Tris-HCl, pH 7.5, 74.5 µl of 1 M $MgCl_2$, 75 µl of 1 M DTT, 80 µl of 10 mg ml^{-1} BSA, 80 µl of 100 mM ATP and 3,000 U of T4 DNA ligase, and ligated at room temperature for 2 h. After overnight reverse crosslinking, DNA was purified and analysed by qPCR. Interaction frequencies were calculated using the $2^{-\Delta\Delta Ct}$ method and normalized to the interaction frequency between two consecutive HindIII or NdeI fragments at the *Rplp0* locus, serving as an internal control for digestion and ligation efficiency. Primer sequences are listed in Supplementary Table 7.

Deletion of enhancer DNA fragment with CRISPR–Cas9

Enhancer fragments were deleted using CRISPR–Cas9-dual gRNA system. For each locus, 3 µl of each 120 µM gRNA (*Slc16a1*: CATGA ATGTCAGGCGTGAAG, TAGCTTTACCTCGGCTCCCC; *Ppargc1a*: TAGTTGGTCAGTAAGCGGTA, GCCTGAGATTTAGTAAAGCG; *Ucp1*: GAA-GACAGTCAGTAGAGCAA, CCACTCAGTTTCTGAGAAGG) was combined with 4 µl of 20 µM Cas9 in 100 µl nucleofection solution and delivered into 0.6×10^6 preadipocytes using programme CM137. Genomic DNA was collected 5 days later, and fragment deletion was assessed by PCR using primers listed in Supplementary Table 7.

RNA extraction and RT–qPCR

Total RNA from cultured cells were extracted using Direct-zol RNA Miniprep kits (Zymo Research, R2050). BAT was homogenized in TRIzol using the Bullet Blender Homogenizer (Next Advance) and supernatants were collected for subsequent RNA extraction. cDNA was synthesized using the High-Capacity cDNA Reverse Transcription Kit (Applied Biosystems, Thermo Fisher Scientific, 4368814) with random hexamers. The relative expression of genes was normalized to ARBP mRNA (mouse) or 18S ribosomal RNA (human), respectively. Primer sequences are listed in Supplementary Table 7.

enChIP and analysis

enChIP was performed as described[27] with minor modifications. Mouse brown adipocytes expressing 3×FLAG-dCas9 (Addgene, plasmid no. 51240, a gift from H. Fujii's laboratory) were nucleofected with vectors (Addgene, plasmid no. 41824, a gift from G. Church's laboratory) encoding five gRNAs targeting the *Ucp1* regulatory region (Supplementary Table 7) or a GFP gRNA control, followed by treatment with vehicle or 1 µM CL316,243 for 4 h. Formaldehyde-crosslinked cells were lysed, nuclei isolated and chromatin sheared to 100–500 bp by sonication. FLAG-tagged chromatin complexes were immunoprecipitated with anti-FLAG M2 magnetic beads overnight at 4 °C, washed with low-salt, high-salt, lithium chloride and TBS buffers, and eluted with 3×FLAG peptide. Eluted proteins were TCA-precipitated, reduced, alkylated, trypsin-digested, TMT-labelled and analysed by LC–MS (Thermo Fisher Scientific Center for Multiplexed Proteomics, Harvard Medical School). Three biological replicates per condition were analysed. Peptide intensities were normalized to dCas9 within each immunoprecipitation and to the GFP gRNA control to account for background binding. Protein enrichment was calculated as fold change between CL316,243-treated and vehicle samples. Identified proteins are listed in Supplementary Table 3.

Knockdown of H2A.Z1 and $p18^{Hamlet}$ in mature adipocytes via lentiviral shRNA

Gene-targeting or non-targeting control shRNAs (Supplementary Table 7) were cloned into the pLKO.1-TRC vector (Addgene, plasmid no. 10878, a gift from D. Root) and packaged into lentivirus. Day-6 mouse adipocytes or day-21 primary human adipocytes were infected, and knockdown efficiency was assessed 5 days later by qRT–PCR and/or western blotting.

Reverse siRNA transfection in mature adipocytes

Mouse H2A.Z1-targeting siRNA (Horizon, L-042994-01-0005), $p18^{Hamlet}$-targeting siRNA (Horizon, L-053282-01-0005), $p18^{Hamlet}$ UTR-targeting siRNA for rescue experiment (GGACAGAGAGAGG

GAGAAAUU), MED1-targeting siRNA (Horizon, L-040964-01-0005) or a non-targeting control (Horizon, D-001810-10-05) were introduced into mature mouse brown adipocytes by reverse transfection. For each well of a collagen-coated (50 μg ml^{-1}) 24-well plate, 3.5 μl of 10 μM siRNA and 3 μl Lipofectamine RNAiMAX were separately diluted in Opti-MEM, combined and incubated for 20 min before plating. Adipocytes were trypsinized and counted, and 4.5×10^5 cells in 250 μl medium were added per well (final siRNA concentration, 100 nM). Cells were harvested 3 days after transfection.

Construction of p18^{Hamlet} expression plasmids

Synthesized full-length p18^{Hamlet} WT or mutant (T64A, T103A or dual) cDNAs with an N-terminal V5 tag were cloned into the pLVX vector (Takara Bio, PT4002-5) using EcoRI and BamHI. Mutant sequences and primer sets are provided in Supplementary Table 7.

Western blotting

Cells were lysed in RIPA buffer (Boston BioProducts, BP-115) supplemented with protease and phosphatase inhibitors (Millipore Sigma, P8340, P5726, P0044). BAT was homogenized using a Bullet Blender (Next Advance), centrifuged (16,000*g*, 10 min, 4 °C) and supernatants collected. Protein concentration was determined by BCA assay (Thermo Fisher Scientific, 23225). Lysates were denatured in 1× Laemmli buffer (Bio-Rad, 1610747), separated on 4–20% Mini-PROTEAN TGX precast gels and transferred to 0.22-μm nitrocellulose membranes. Membranes were incubated overnight at 4 °C with primary antibodies (Reporting Summary) diluted in TBST with 1% BSA, followed by horseradish peroxidase-conjugated secondary antibodies diluted in TBST with 1% milk. Signals were detected using SuperSignal West Femto substrate (Thermo Fisher Scientific, 34094) and imaged on a Bio-Rad ChemiDoc system.

Bioenergetic profiling

Mitochondrial respiration was assessed using a Seahorse Extracellular Flux Analyzer (Seahorse Bioscience). Adipocytes were pretreated overnight with 1 μM CL316,243 (mouse) or 10 μM FSK (human). On the day of the assay, cells were incubated in serum-free DMEM containing 25 mM glucose and 1 mM pyruvate, and OCR was measured following sequential injection of oligomycin (2 μM; ATP-linked respiration), FCCP (2 μM; maximal respiration) and antimycin A (2 μM; non-mitochondrial respiration). OCR values were normalized to protein content.

Immunoprecipitation and co-immunoprecipitation

Immortalized or primary brown adipocytes expressing V5-tagged WT or mutant p18^{Hamlet} were treated with 1 μM CL316,243 for the indicated times, washed with ice-cold PBS, lysed in NP-40 buffer containing protease and phosphatase inhibitors, sonicated (QSONICA Q500, 30% amplitude, 30 s) and clarified by centrifugation (13,000*g*, 10 min, 4 °C). Protein concentration was determined by BCA assay. In total, 100 μg lysate was incubated with V5-Trap magnetic agarose (Proteintech) according to the manufacturer's instructions and eluted in Laemmli buffer by boiling.

For YL1 co-immunoprecipitation, lysates were incubated with YL1 antibody (Abcam, ab112055) for 2 h at 4 °C, followed by Dynabeads Protein G for 30 min, washed, and eluted by boiling in Laemmli buffer. Samples were analysed by western blotting.

ChIP

ChIP was performed in mouse and primary human brown adipocytes using MNase digestion or sonication depending on the target. For histone ChIP in mouse adipocytes, MNase-ChIP was used. Cells were crosslinked with 1% formaldehyde (10 min), quenched with glycine, permeabilized in PBS containing 0.1% Triton X-100 and protease inhibitors, and digested with MNase at 37 °C for 10 min to yield ~70% mononucleosomes. Digested chromatin was extracted in ChIP buffer (50 mM Tris pH 8.0, 150 mM NaCl, 1% Triton X-100, 0.1% sodium deoxycholate, 5 mM EDTA, 1 mM PMSF, 1× protease inhibitor cocktail), clarified and incubated overnight at 4 °C with antibodies against H2A.Z (Abcam, ab4174), H3K4me3 (Millipore Sigma, 07-473), H3K27ac (Active Motif, 39133) or control IgG (Cell Signaling, 2729).

For CTCF ChIP, cells were crosslinked with 1% formaldehyde (10 min). For SMC1 and MED1 ChIP, cells were first crosslinked with DSG (2 mM, 45 min) followed by formaldehyde. Chromatin was lysed (50 mM Tris pH 7.5, 1% SDS, 0.25% sodium deoxycholate and 1× protease inhibitor cocktail) on ice for 10 min, diluted (50 mM Tris pH 7.5, 0.1% SDS, 150 mM NaCl, 1.84% Triton X-100 and 1× protease inhibitor cocktail) and sonicated (Branson SFX250, 50% amplitude, 3.5 min) to shear DNA, and then incubated overnight with antibodies against CTCF (Cell Signaling, 3418S), SMC1 (Thermo Fisher Scientific, A300-055A) or MED1 (Invitrogen, PA5-36114).

For H2A.Z and H3K27ac ChIP–seq in primary human brown adipocytes, nuclei were isolated, fixed with formaldehyde, sonicated (40% amplitude, 3.5 min) and incubated with antibodies against H2A.Z (Active Motif, 39943) or H3K27ac (Active Motif, 39133) overnight.

Immune complexes were captured with Dynabeads Protein G, washed sequentially with low-salt, high-salt, lithium chloride and TE buffers, and eluted. Crosslinks were reversed by RNase A and proteinase K digestion, and DNA was purified using AMPure XP beads. ChIP DNA was used for qPCR or library preparation. Two or three replicates were generated for ChIP–seq under each condition and sequenced on Illumina platforms: NextSeq 500 (mouse H3K27ac, H3K4me3), HiSeq 2500 (mouse H2A.Z) or NovaSeq X Plus (CTCF, SMC1, MED1 and human H2A.Z, H3K27ac).

CUT&RUN

Primary brown adipocytes were isolated from BAT of mice housed at thermoneutrality or 5 °C for 4 h. Cells were fixed with 1% formaldehyde (15 min), washed in HEPES-based buffer containing spermidine and protease inhibitors, and immobilized on ConA-coated magnetic beads. Beads were incubated overnight at 4 °C with H2A.Z antibody (Abcam, ab4174) or rabbit IgG in digitonin-containing buffer, washed, and incubated with Protein A/G–MNase (700 ng μl^{-1}) for 1 h at 4 °C. After additional washes, MNase digestion was initiated with $CaCl_2$ at 0 °C for 30 min and stopped with EDTA/EGTA-containing buffer supplemented with RNase A and glycogen, followed by incubation at 37 °C for 30 min. Released DNA fragments were purified for downstream analysis. Three biological replicates per condition were prepared. Libraries were constructed and sequenced by BGI Genomics on a BGISEQ-500 platform.

ATAC-seq

ATAC-seq was performed using the ATAC-Seq Kit (Active Motif, 53150) with modifications. Mouse brown adipocytes were treated with vehicle or 1 μM CL316,243 for 4 h; DNase I (200 U ml^{-1}) was added 30 min before harvest to remove extracellular DNA. Cells were washed with ice-cold PBS, scraped and counted, and 50,000 cells were pelleted (500*g*, 5 min, 4 °C). Nuclei were isolated, tagmented at 37 °C for 30 min with agitation, and DNA was purified by column clean-up for library preparation. Two biological replicates per condition were sequenced on an Illumina NextSeq 500.

ChIP–seq, CUT&RUN and ATAC-seq analysis

The raw reads from ChIP–seq, CUT&RUN and ATAC-seq data were preprocessed using the CHIPS pipeline[66], which includes read trimming, genome mapping (mm10 or hg38), peak calling and quality control. For H2A.Z ChIP–seq and ATAC-seq data, particularly, BAM files with deduplicated reads were imported into DANPOS2 software[67] for genome-wide peak identification. The pyBigWig package (version 0.3.20) extracted signals from BigWig files based on the genomic intervals of interest to generate density plots for ChIP–seq and ATAC-seq. Motif analyses were performed using Homer (v4.11.1) on the given peak centres with the options --size 600 -bits.

AAV administration to BAT

Isoform-specific gRNAs targeting H2A.Z1 or a non-targeting control were cloned into the pAAV-gRNA vector (Addgene, plasmid no. 89060, a gift from W. Lagor). AAV2/AAV8 serotype particles were prepared by the Boston Children's Hospital Viral Core. AAV administration to BAT was performed as previously described[39]. Twelve- to sixteen-week-old Ucp1-Cre/Cas9 knock-in mice were anaesthetized with 2.5% isoflurane, the interscapular BAT was surgically exposed, and AAV2/AAV8 was injected directly into each lobe (1×10^{11} genome copies per lobe).

Seven days after AAV administration, genomic DNA was extracted from BAT. The gRNA-targeted genomic regions were amplified by PCR, and the products were subjected to Sanger sequencing. Primer sequences are listed in Supplementary Table 7.

Cold tolerance test

For cold tolerance tests, mice were individually housed and placed in a chamber (Carno Products & Services) set at an ambient temperature of 5 °C for 8 h. The mice had free access to food and water during cold exposure. Rectal temperature was measured at the indicated time points using an aRET-3 rectal probe (Physitemp).

Glucose and insulin tolerance tests

Glucose uptake in cultured adipocytes was measured using the Glucose Uptake-Glo Assay (Promega, J1341). For in vivo glucose tolerance tests, mice were fasted for 6 h with free access to water, and baseline blood glucose was measured from the tail. Glucose (2 g per kg body weight, i.p.) was administered, and blood glucose was measured at the indicated time points. For insulin tolerance tests, mice were similarly fasted and injected with insulin (1 U per kg body weight, i.p.), followed by glucose measurements over time. Glucose concentrations were determined using an Infinity Blood Glucose Meter (US Diagnostics). Glucose clearance and insulin sensitivity were assessed by calculating the AUC.

Indirect calorimetry

For maximal thermogenic capacity measurement, mice were injected i.p. with pentobarbital (65 mg per kg body weight). Basal energy expenditure and oxygen consumption (VO_2) were measured for 20 min before an i.p. injection of noradrenaline (1 mg per kg body weight). Energy expenditure and VO_2 in mice were measured using either a Columbus Instruments' Oxymax-CLAMS or a Sable Systems' Promethion system according to the guidelines.

Body composition analysis

For body composition analysis, mice were anaesthetized with 2% isoflurane and scanned using dual-energy X-ray absorptiometry.

Measurement of blood parameters

Plasma insulin level was determined by the Ultra-Sensitive Mouse Insulin ELISA kit (Crystal Chem, 90080). Insulin resistance was assessed by calculating the Homeostatic Model Assessment of Insulin Resistance ((fasting glucose × fasting insulin)/405).

Chromatin loop conservation analysis

Mouse loop anchors were first lifted over to the human genome using AdaLiftOver[42]. Conservation was quantified by comparing the mouse-liftovered loop anchors with human loops identified from our human Micro-C data. A mouse loop was defined as conserved if both anchors were successfully liftovered and the corresponding human genomic regions formed a loop. Specifically, a pair of mouse-liftovered anchors was defined as a loop in humans if any human loop was detected within a 20,000-bp window for each liftovered anchor.

Integration of GWAS with chromatin loops

Human GWAS (hg38) data were downloaded from the UCSC Table Browser[68], focusing on significant associations with $P < 1 \times 10^{-8}$. For each chromatin loop anchor (±100-kb window), lead SNPs with the highest association in GWAS were identified and expanded to include variants in strong linkage disequilibrium ($R^2 > 0.8$) using the LDlink API (the EUR population was used due to the predominance of European GWAS data). Enrichment of trait-associated SNPs at loop anchors was assessed using Fisher's exact test against non-trait SNPs as background, with fold enrichment calculated and P values adjusted by Benjamini–Hochberg false discovery rate correction.

Chromatin loop connectivity analysis

To define a pair of connected loops, we required that any anchors of the two loops either overlapped at the same genomic location or were directly adjacent with no gaps between them. This analysis identified two loops with a direct connection. Multiple loop connections were further identified based on these direct connections, allowing us to detect indirect connections between two loops through intermediate loops. Both direct and indirect loop connections were used in the downstream analysis.

Statistical analyses

Statistical analyses were performed in Python (v3.8), R (v4.1.0) and GraphPad Prism (v8.0 and v10). Group comparisons used unpaired two-sided t-tests or Wilcoxon rank-sum tests, with two-way ANOVA for time-course data; GWAS SNPs in loop enrichment were assessed by Fisher's exact test, gene-set enrichment by fgsea (v.1.18.0) permutation tests, differential expression by DESeq2 (two-sided Wald test, negative binomial distribution-based model) and correlations by Pearson and Spearman correlation. ChIP–seq, ATAC-seq and CUT&RUN peaks were called with MACS2 or DANPOS2 (Poisson distribution-based models), and Micro-C data were ICE-normalized, which assumes equal visibility across loci. For analyses using t-tests, data distribution was assumed to be normal, but this was not formally tested. Both male and female mice were used for experiments. No statistical methods were used to predetermine sample sizes, but our sample sizes for mouse studies are similar to those reported in previous publications[69,70]. Mice were randomly assigned at the time of weaning and AAV injection to minimize any potential bias. Although primary investigators were not blinded in most studies, certain analyses (for example, sequencing and mouse metabolic measurements) were conducted by personnel unaware of sample groupings. All samples were processed and analysed using standardized pipelines, and data were excluded only for documented technical errors or non-concordant technical replicates.

Reporting summary

Further information on research design is available in the Nature Portfolio Reporting Summary linked to this article.

Data availability

All sequencing data were deposited at NCBI's Gene Expression Omnibus and are publicly available as the date of publication via the following accession numbers.

- Raw and analysed Micro-C in mouse brown adipocytes: GSE261416
- Raw and analysed RNA-seq in mouse brown adipocytes: GSE261413
- Raw and analysed PRO-seq in mouse brown adipocytes: GSE301361
- Raw and analysed ChIP–seq for H2A.Z, H3K27ac and H3K4me3 in mouse brown adipocytes: GSE261412
- Raw and analysed ATAC-seq in mouse brown adipocytes: SE261410
- Raw and analysed CUT&RUN in mouse brown adipocytes: GSE301360
- Raw and analysed ChIP–seq for CTCF, SMC1 and MED1 in mouse brown adipocytes: GSE301366
- Raw and analysed Micro-C in human brown adipocytes: GSE301370
- Raw and analysed RNA-seq in human brown adipocytes: GSE301359
- Raw and analysed ChIP–seq in human brown adipocytes: GSE301368

Source data are provided with this paper.

Code availability

All original code is publicly available on GitHub via https://github.com/zhengrongbin/brown_adipo_loop_H2AZ_paper/.

References

1. Shamsi, F., Wang, C. H. & Tseng, Y. H. The evolving view of thermogenic adipocytes—ontogeny, niche and function. *Nat. Rev. Endocrinol.* **17**, 726–744 (2021).
2. van Marken Lichtenbelt, W. D. et al. Cold-activated brown adipose tissue in healthy men. *N. Engl. J. Med.* **360**, 1500–1508 (2009).
3. Becher, T. et al. Brown adipose tissue is associated with cardiometabolic health. *Nat. Med.* **27**, 58–65 (2021).
4. Tseng, Y. H., Cypess, A. M. & Kahn, C. R. Cellular bioenergetics as a target for obesity therapy. *Nat. Rev. Drug Discov.* **9**, 465–482 (2010).
5. Lowell, B. B. & Spiegelman, B. M. Towards a molecular understanding of adaptive thermogenesis. *Nature* **404**, 652–660 (2000).
6. Inagaki, T., Sakai, J. & Kajimura, S. Transcriptional and epigenetic control of brown and beige adipose cell fate and function. *Nat. Rev. Mol. Cell Biol.* **17**, 480–495 (2016).
7. Sambeat, A., Gulyaeva, O., Dempersmier, J. & Sul, H. S. Epigenetic regulation of the thermogenic adipose program. *Trends Endocrinol. Metab.* **28**, 19–31 (2017).
8. Yi, D., Nguyen, H. P. & Sul, H. S. Epigenetic dynamics of the thermogenic gene program of adipocytes. *Biochem. J.* **477**, 1137–1148 (2020).
9. Zheng, H. & Xie, W. The role of 3D genome organization in development and cell differentiation. *Nat. Rev. Mol. Cell Biol.* **20**, 535–550 (2019).
10. Jerkovic, I. & Cavalli, G. Understanding 3D genome organization by multidisciplinary methods. *Nat. Rev. Mol. Cell Biol.* **22**, 511–528 (2021).
11. Hsieh, T. S. et al. Resolving the 3D landscape of transcription-linked mammalian chromatin folding. *Mol. Cell* **78**, 539–553 (2020).
12. Krietenstein, N. et al. Ultrastructural details of mammalian chromosome architecture. *Mol. Cell* **78**, 554–565 (2020).
13. Lieberman-Aiden, E. et al. Comprehensive mapping of long-range interactions reveals folding principles of the human genome. *Science* **326**, 289–293 (2009).
14. Dixon, J. R. et al. Topological domains in mammalian genomes identified by analysis of chromatin interactions. *Nature* **485**, 376–380 (2012).
15. Schoenfelder, S. & Fraser, P. Long-range enhancer-promoter contacts in gene expression control. *Nat. Rev. Genet.* **20**, 437–455 (2019).
16. Batut, P. J. et al. Genome organization controls transcriptional dynamics during development. *Science* **375**, 566–570 (2022).
17. Madsen, J. G. S. et al. Highly interconnected enhancer communities control lineage-determining genes in human mesenchymal stem cells. *Nat. Genet.* **52**, 1227–1238 (2020).
18. Keipert, S. et al. Two-stage evolution of mammalian adipose tissue thermogenesis. *Science* **384**, 1111–1117 (2024).
19. Salameh, T. J. et al. A supervised learning framework for chromatin loop detection in genome-wide contact maps. *Nat. Commun.* **11**, 3428 (2020).
20. Hsieh, T. S. et al. Enhancer-promoter interactions and transcription are largely maintained upon acute loss of CTCF, cohesin, WAPL or YY1. *Nat. Genet.* **54**, 1919–1932 (2022).
21. Mimoso, C. A. & Goldman, S. R. PRO-seq: precise mapping of engaged RNA Pol II at single-nucleotide resolution. *Curr. Protoc.* **3**, e961 (2023).
22. Petersen, C. et al. MCT1 and MCT4 expression and lactate flux activity increase during white and brown adipogenesis and impact adipocyte metabolism. *Sci. Rep.* **7**, 13101 (2017).
23. Puigserver, P. et al. A cold-inducible coactivator of nuclear receptors linked to adaptive thermogenesis. *Cell* **92**, 829–839 (1998).
24. Wang, C. H. et al. CRISPR-engineered human brown-like adipocytes prevent diet-induced obesity and ameliorate metabolic syndrome in mice. *Sci. Transl. Med.* **12**, eaaz8664 (2020).
25. Inoue, S. I. et al. Short-term cold exposure induces persistent epigenomic memory in brown fat. *Cell Metab.* **36**, 1764–1778 (2024).
26. Xue, P. et al. A distal enhancer with ETV4 binding is critical for UCP1 expression and thermogenesis in brown fat. *Genes Dev.* **39**, 13–14 (2025).
27. Shamsi, F. et al. FGF6 and FGF9 regulate UCP1 expression independent of brown adipogenesis. *Nat. Commun.* **11**, 1421 (2020).
28. Colino-Sanguino, Y., Clark, S. J. & Valdes-Mora, F. The H2A.Z-nuclesome code in mammals: emerging functions. *Trends Genet.* **38**, 273–289 (2022).
29. Tang, Q. Q., Otto, T. C. & Lane, M. D. Mitotic clonal expansion: a synchronous process required for adipogenesis. *Proc. Natl Acad. Sci. USA* **100**, 44–49 (2003).
30. Cuadrado, A. et al. Essential role of p18Hamlet/SRCAP-mediated histone H2A.Z chromatin incorporation in muscle differentiation. *EMBO J.* **29**, 2014–2025 (2010).
31. Cuadrado, A. et al. A new p38 MAP kinase-regulated transcriptional coactivator that stimulates p53-dependent apoptosis. *EMBO J.* **26**, 2115–2126 (2007).
32. Cao, W. et al. p38 mitogen-activated protein kinase is the central regulator of cyclic AMP-dependent transcription of the brown fat uncoupling protein 1 gene. *Mol. Cell. Biol.* **24**, 3057–3067 (2004).
33. Liang, X. et al. Structural basis of H2A.Z recognition by SRCAP chromatin-remodeling subunit YL1. *Nat. Struct. Mol. Biol.* **23**, 317–323 (2016).
34. Li, S., Wei, T. & Panchenko, A. R. Histone variant H2A.Z modulates nucleosome dynamics to promote DNA accessibility. *Nat. Commun.* **14**, 769 (2023).
35. Phanstiel, D. H. et al. Static and dynamic DNA loops form AP-1-bound activation hubs during macrophage development. *Mol. Cell* **67**, 1037–1048 (2017).
36. Kagey, M. H. et al. Mediator and cohesin connect gene expression and chromatin architecture. *Nature* **467**, 430–435 (2010).
37. Ramasamy, S. et al. The Mediator complex regulates enhancer-promoter interactions. *Nat. Struct. Mol. Biol.* **30**, 991–1000 (2023).
38. Harms, M. J. et al. PRDM16 binds MED1 and controls chromatin architecture to determine a brown fat transcriptional program. *Genes Dev.* **29**, 298–307 (2015).
39. Tsuji, T., Zhang, Y. & Tseng, Y. H. Generation of brown fat-specific knockout mice using a combined Cre-LoxP, CRISPR-Cas9 and adeno-associated virus single-guide RNA system. *J. Vis. Exp.* https://doi.org/10.3791/65083 (2023).
40. Min, S. Y. et al. Human 'brite/beige' adipocytes develop from capillary networks, and their implantation improves metabolic homeostasis in mice. *Nat. Med.* **22**, 312–318 (2016).
41. Syamsunarno, M. R. et al. Fatty acid binding protein 4 and 5 play a crucial role in thermogenesis under the conditions of fasting and cold stress. *PLoS ONE* **9**, e90825 (2014).
42. Dong, C., Shen, S. & Keles, S. AdaLiftOver: high-resolution identification of orthologous regulatory elements with Adaptive liftOver. *Bioinformatics* **39**, btad149 (2023).
43. Civelek, M. et al. Genetic regulation of adipose gene expression and cardio-metabolic traits. *Am. J. Hum. Genet.* **100**, 428–443 (2017).

44. Bond, M. L. et al. Chromatin loop dynamics during cellular differentiation are associated with changes to both anchor and internal regulatory features. *Genome Res.* **33**, 1258–1268 (2023).
45. Siersbaek, R. et al. Dynamic rewiring of promoter-anchored chromatin loops during adipocyte differentiation. *Mol. Cell* **66**, 420–435 (2017).
46. Dall'Agnese, A. et al. Transcription factor-directed re-wiring of chromatin architecture for somatic cell nuclear reprogramming toward trans-differentiation. *Mol. Cell* **76**, 453–472 (2019).
47. Sanalkumar, R. et al. Highly connected 3D chromatin networks established by an oncogenic fusion protein shape tumor cell identity. *Sci. Adv.* **9**, eabo3789 (2023).
48. Tseng, Y. H., Kriauciunas, K. M., Kokkotou, E. & Kahn, C. R. Differential roles of insulin receptor substrates in brown adipocyte differentiation. *Mol. Cell. Biol.* **24**, 1918–1929 (2004).
49. Arianti, R. et al. Upregulation of inhibitor of DNA binding 1 and 3 is important for efficient thermogenic response in human adipocytes. *Sci Rep.* **14**, 28272 (2024).
50. Xue, R. et al. Clonal analyses and gene profiling identify genetic biomarkers of the thermogenic potential of human brown and white preadipocytes. *Nat. Med.* **21**, 760–768 (2015).
51. Dobin, A. et al. STAR: ultrafast universal RNA-seq aligner. *Bioinformatics* **29**, 15–21 (2013).
52. Love, M. I., Huber, W. & Anders, S. Moderated estimation of fold change and dispersion for RNA-seq data with DESeq2. *Genome Biol.* **15**, 550 (2014).
53. Subramanian, A. et al. Gene set enrichment analysis: a knowledge-based approach for interpreting genome-wide expression profiles. *Proc. Natl Acad. Sci. USA* **102**, 15545–15550 (2005).
54. Korotkevich, G. et al. Fast gene set enrichment analysis. Preprint at *bioRxiv* https://doi.org/10.1101/060012 (2021).
55. Kanehisa, M., Furumichi, M., Sato, Y., Ishiguro-Watanabe, M. & Tanabe, M. KEGG: integrating viruses and cellular organisms. *Nucleic Acids Res.* **49**, D545–D551 (2021).
56. Fang, Z., Liu, X. & Peltz, G. GSEApy: a comprehensive package for performing gene set enrichment analysis in Python. *Bioinformatics* **39**, btac757 (2023).
57. Emmett, M. J. et al. Histone deacetylase 3 prepares brown adipose tissue for acute thermogenic challenge. *Nature* **546**, 544–548 (2017).
58. Li, H. & Durbin, R. Fast and accurate long-read alignment with Burrows–Wheeler transform. *Bioinformatics* **26**, 589–595 (2010).
59. Abdennur, N. & Mirny, L. A. Cooler: scalable storage for Hi-C data and other genomically labeled arrays. *Bioinformatics* **36**, 311–316 (2020).
60. Durand, N. C. et al. Juicer provides a one-click system for analyzing loop-resolution Hi-C experiments. *Cell Syst.* **3**, 95–98 (2016).
61. Yang, T. et al. HiCRep: assessing the reproducibility of Hi-C data using a stratum-adjusted correlation coefficient. *Genome Res.* **27**, 1939–1949 (2017).
62. Consortium, E. P. et al. Expanded encyclopaedias of DNA elements in the human and mouse genomes. *Nature* **583**, 699–710 (2020).
63. Open2C; Abdennur, N et al. Cooltools: enabling high-resolution Hi-C analysis in Python. *PLoS Comput. Biol.* **20**, e1012067 (2024).
64. Chen, E. Y. et al. Enrichr: interactive and collaborative HTML5 gene list enrichment analysis tool. *BMC Bioinformatics* **14**, 128 (2013).
65. Hagege, H. et al. Quantitative analysis of chromosome conformation capture assays (3C-qPCR). *Nat. Protoc.* **2**, 1722–1733 (2007).
66. Taing, L. et al. CHIPS: a Snakemake pipeline for quality control and reproducible processing of chromatin profiling data. *F1000Research* **10**, 517 (2021).
67. Chen, K. et al. DANPOS: dynamic analysis of nucleosome position and occupancy by sequencing. *Genome Res.* **23**, 341–351 (2013).
68. Buniello, A. et al. The NHGRI-EBI GWAS Catalog of published genome-wide association studies, targeted arrays and summary statistics 2019. *Nucleic Acids Res.* **47**, D1005–D1012 (2019).
69. Sugimoto, S. et al. Brown adipose tissue-derived MaR2 contributes to cold-induced resolution of inflammation. *Nat. Metab.* **4**, 775–790 (2022).
70. Tsuji, T. et al. Light-responsive adipose-hypothalamus axis controls metabolic regulation. *Nat. Commun.* **15**, 6768 (2024).

Acknowledgements

This work was supported in part by the US National Institutes of Health (NIH) grants R01DK132469, R01DK102898 and R01DK133528 (to Y.-H.T.), R01GM125632, R01GM138407, R01HL148338, R01HL133254 and R01CA278832 (to K.C.), K99HG013662 (to R.Z.), P30DK036836 and S10OD028568 (to Joslin Diabetes Center's Diabetes Research Center), National Research, Development and Innovation Office of Hungary grants PD146202 (to R.A.) and FK145866 (to E.K.), the János Bolyai Fellowship of the Hungarian Academy of Sciences (to E.K.), and the Charles A. King Trust Postdoctoral Research Fellowship programme from the Health Resource in Action (to Y.Z.). The funders had no role in study design, data collection and analysis, decision to publish or preparation of the paper.

Author contributions

Y.Z. designed the research, carried out most of the experiments, and wrote the paper. R.Z. analysed the next-generation sequencing data and co-wrote the paper. T.T. performed the AAV injection and analysed the metabolic phenotypes of the mice. C.-H.W. performed CUT&RUN and enChIP experiments. X.-Y.L. established the nuclei isolation protocol in primary human brown adipocytes. X.-Y.L. is supervised by C.R.K. and S.E.J. Y.-H.X. performed the next-generation sequencing for most of the samples. R.D. processed part of the raw next-generation sequencing data. Y.-H.X. and R.D. are supervised by M.N.R. J.D., M.D.L. and M.L. performed the enChIP experiment. M.L. is supervised by B.E. R.A., F.G. and E.K. isolated primary human brown preadipocytes. Y.-H.T. and K.C. directed the research and co-wrote the paper. All authors read and edited the paper.

Competing interests

The authors declare no competing interests.

Additional information

Extended data is available for this paper at https://doi.org/10.1038/s42255-026-01510-2.

Supplementary information The online version contains supplementary material available at https://doi.org/10.1038/s42255-026-01510-2.

Correspondence and requests for materials should be addressed to Kaifu Chen or Yu-Hua Tseng.

Peer review information *Nature Metabolism* thanks the anonymous reviewers for their contribution to the peer review of this work. Primary Handling Editor: Revati Dewal, in collaboration with the *Nature Metabolism* team.

[1]Section on Integrative Physiology and Metabolism, Research Division, Joslin Diabetes Center, Harvard Medical School, Boston, MA, USA. [2]Basic and Translational Research Division, Department of Cardiology, Boston Children's Hospital, Boston, MA, USA. [3]Department of Pediatrics, Harvard Medical School, Boston, MA, USA. [4]Broad Institute of MIT and Harvard, Cambridge, MA, USA. [5]Department of Pathology, Massachusetts General Hospital and Harvard Medical School, Charlestown, MA, USA. [6]Novo Nordisk Foundation Center for Basic Metabolic Research, Faculty of Health and Medical Sciences, University of Copenhagen, Copenhagen, Denmark. [7]Laboratory of Cell Biochemistry, Department of Biochemistry and Molecular Biology, Faculty of Medicine, University of Debrecen, Debrecen, Hungary. [8]Department of Surgery, Faculty of Medicine, University of Debrecen, Debrecen, Hungary. [9]Department of Pathology, Dana-Farber Cancer Institute, Boston, MA, USA. [10]Harvard Stem Cell Institute, Harvard University, Cambridge, MA, USA. [11]Division of Nutrition, Harvard Medical School, Boston, MA, USA. [12]These authors contributed equally: Yang Zhang, Rongbin Zheng. ✉e-mail: kaifu.chen@childrens.harvard.edu; yu-hua.tseng@joslin.harvard.edu

https://doi.org/10.1038/s42255-026-01510-2

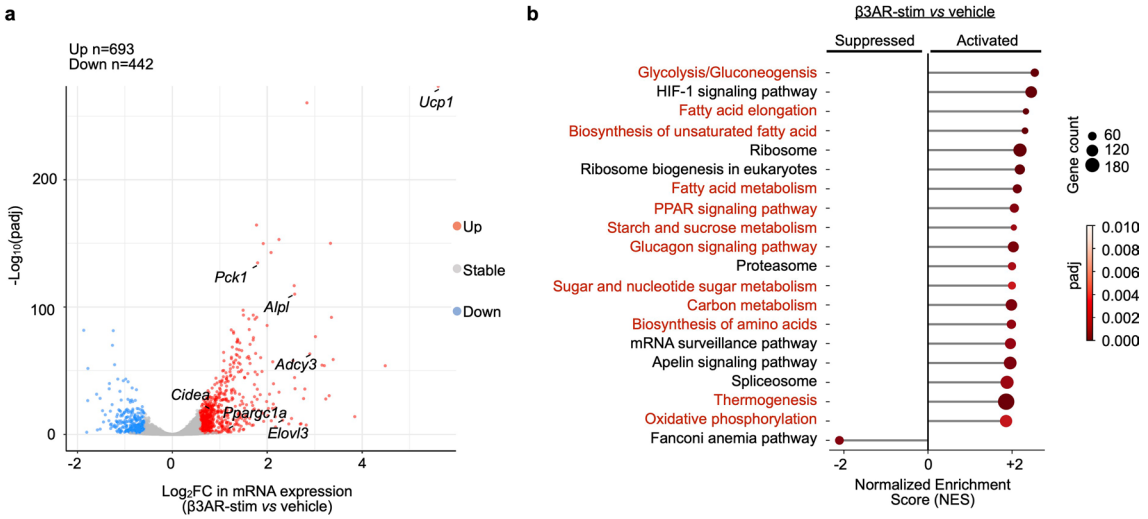

Extended Data Fig. 1 | β3-AR stimulation induces gene activation during thermogenesis. a, Volcano plot showing changes in gene expression profiled by RNA-seq in vehicle-treated (vehicle) and β3-AR-stimulated (β3AR-stim) brown adipocytes. Differences were assessed with two-sided Wald test implemented in DESeq2. Differentially expressed genes were defined with a fold change (FC) > 1.5 and an adjusted *p*-value (padj) < 0.05. β3-AR stimulation-mediated upregulated (Up) genes are labeled in red, and downregulated (Down) genes are labeled in blue. **b**, Gene Set Enrichment Analysis (GESA) of the top functional pathways (KEGG pathways) with positive or negative enrichment in response to β3-AR stimulation. Pathways related to the key functions of brown adipocytes are highlighted in red. P values were estimated using an adaptive multi-level split Monte Carlo scheme implemented in the fgsea R package.

https://doi.org/10.1038/s42255-026-01510-2

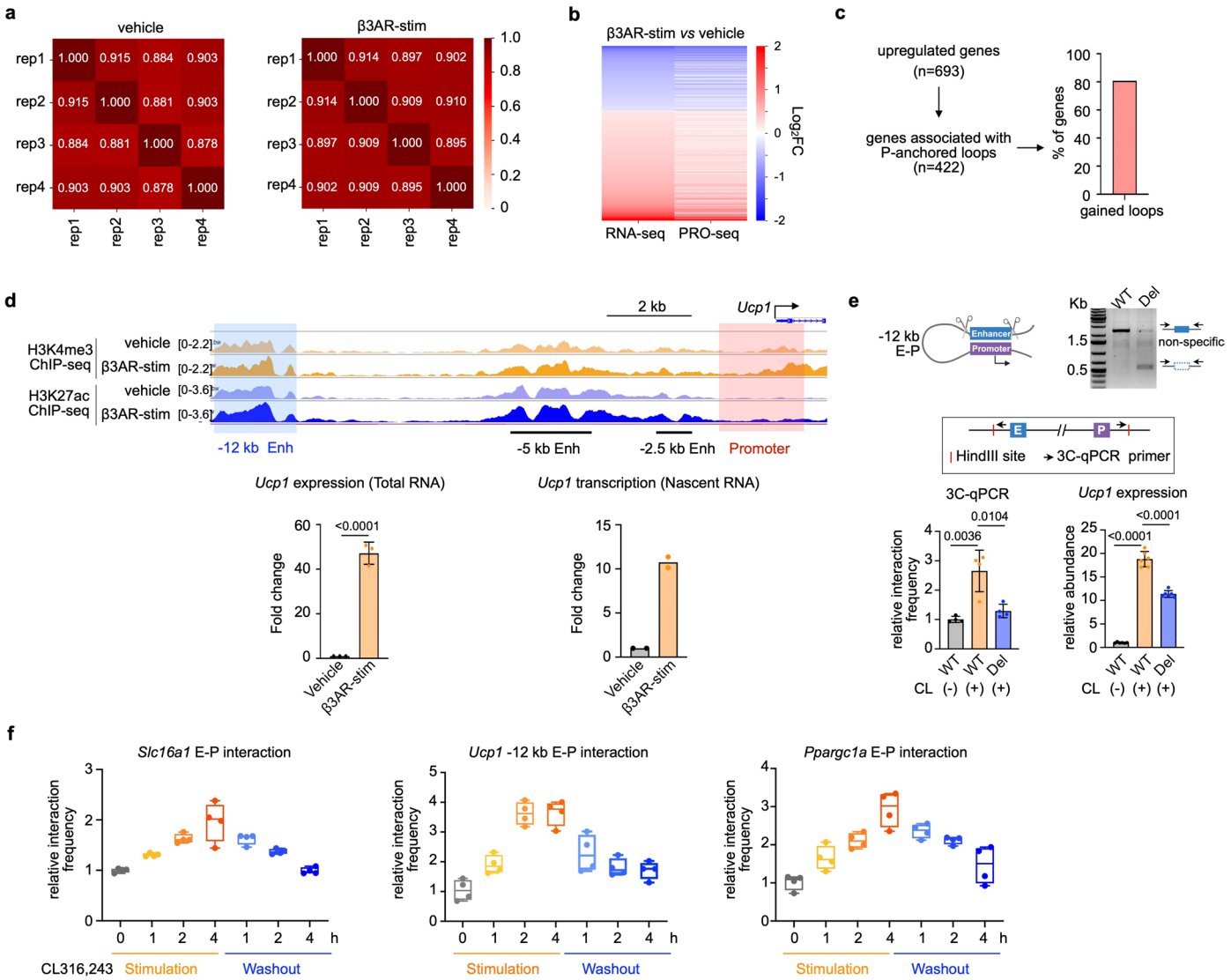

Extended Data Fig. 2 | β3-AR stimulation induces changes in chromatin loops. **a**, Heatmaps showing reproducibility of Micro-C interaction frequencies among four biological replicates for either vehicle-treated (vehicle) or β3-AR-stimulated (β3AR-stim) brown adipocytes. The reproducibility score was determined by HiCrep. **b**, Heatmaps showing correlation of RNA-seq and PRO-seq data from vehicle-treated (vehicle) and β3-AR-stimulated (β3AR-stim) brown adipocytes. Differentially expressed gene in RNA-seq and PRO-seq data were sorted by Log_2 fold change (Log_2FC) in RNA-seq. **c**, Left, number of β3-AR stimulation-upregulated genes associated with promoter-anchored loops. Right, bar plot showing the proportion of the 422 upregulated genes linked to dynamically gained loops in response to β3-AR stimulation. **d**, Top, chromatin tracks for H3K4me3 and H3K27ac ChIP-seq signals at the *Ucp1* locus. The −12 kb enhancer (Enh) and promoter of *Ucp1* are highlighted with transparent light blue and light red boxes, respectively. Bar plots at the bottom showing the fold change in *Ucp1* expression and transcription quantified by RNA-seq and PRO-seq, respectively. Error bar represents the mean ± s.d. of three biological replicates of RNA-seq per condition. *P* adjust (*padj*), two-sided Wald test implemented in DESeq2. **e**, The CRISPR/Cas9-dual gRNA system was used to delete the −12 kb enhancer associated with *Ucp1*. Top, genomic DNA PCR followed by agarose gel electrophoresis. WT, wild type. Del, deletion. Bottom left, the interaction frequency of E-P loop was assessed by 3C-qPCR in adipocytes were treated with vehicle or 1 μM CL316,243 (CL) for 4 h before analysis. $N = 4$ technical replicates per group. Bottom right, expression of *Ucp1* in different conditions. $N = 6$ technical replicates per group. Error bars indicate the mean ± s.d. of technical replicates in each group. Differences were assessed with two-sided unpaired *t* test. **f**, 3C-qPCR analysis of E-P loops associated with *Slc16a1* (left), *Ucp1* (middle), and *Ppargc1a* (right) at different time points during CL316,243 treatment and after remove CL316,243 from the medium. $N = 4$ technical replicates per group. Box plots show the median (center line), 25th–75th percentiles (box) and whiskers indicating the minimum and maximum values; all data points are shown. In **e** and **f**, the data shown are from one of two biological replicates with similar results.

https://doi.org/10.1038/s42255-026-01510-2

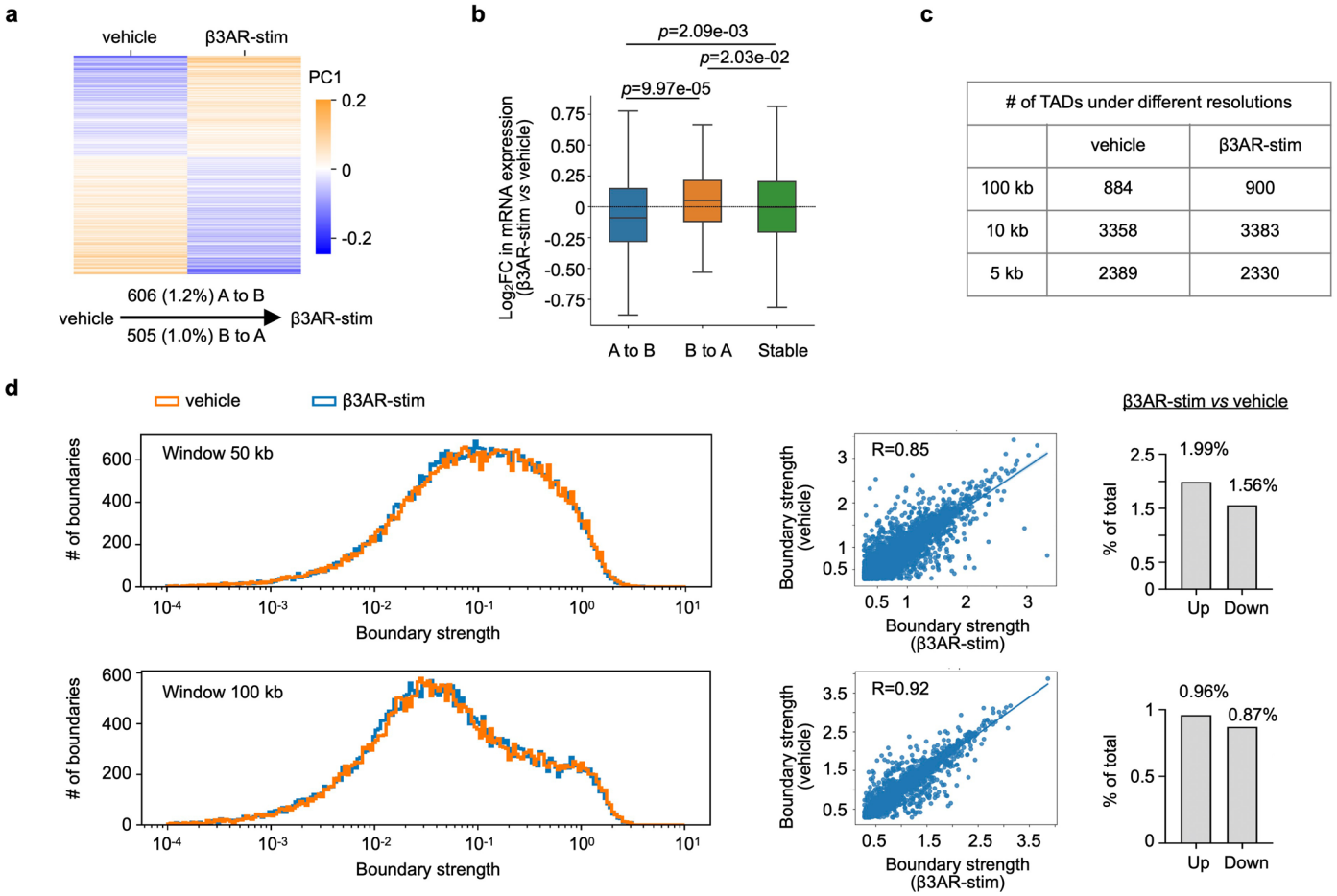

Extended Data Fig. 3 | Compartments and TADs analysis during thermogenesis. a, Heatmap showing switched compartments in vehicle-treated (vehicle) and β3-AR-stimulated (β3AR-stim) brown adipocytes. The compartments were identified by cooltool package using Micro-C data at 50 kb resolution. The eigenvalues of the first principal component (PC1) values were used to determine the A/B compartment status of a given region, where positive PC1 values represent A compartment regions (orange) and negative values represent B compartment regions (blue). The number and percentage of switched compartments are listed at the bottom of the panel. **b**, Distribution of log_2 fold-change (log_2FC) in gene expression for genes that change compartment status ('A to B' ($n = 179$) or 'B to A' ($n = 132$)) or that remain unchanged (stable, $n = 12738$) upon β3-AR stimulation. p value, two-sided wilcoxon test. Boxplot shows median (center line), 25th-75th percentiles (box) and 1.5 x IQR (whiskers). **c**, Number of TADs detected at different resolutions in vehicle-treated (vehicle) and β3-AR-stimulated (β3AR-stim) brown adipocytes. The TAD was identified by HeadArrow algorithm using Micro-C data at different resolutions. **d**, Left, distribution of boundary strength for TADs in both vehicle-treated (vehicle) and β3-AR-stimulated (β3AR-stim) brown adipocytes. Middle, correlation of TAD boundary strength between two conditions. Right, bar plots showing the percentage of boundaries with altered strength (fold change > 2). The boundary strength was computed by cooltool package using Micro-C data at 10 kb resolution.

https://doi.org/10.1038/s42255-026-01510-2

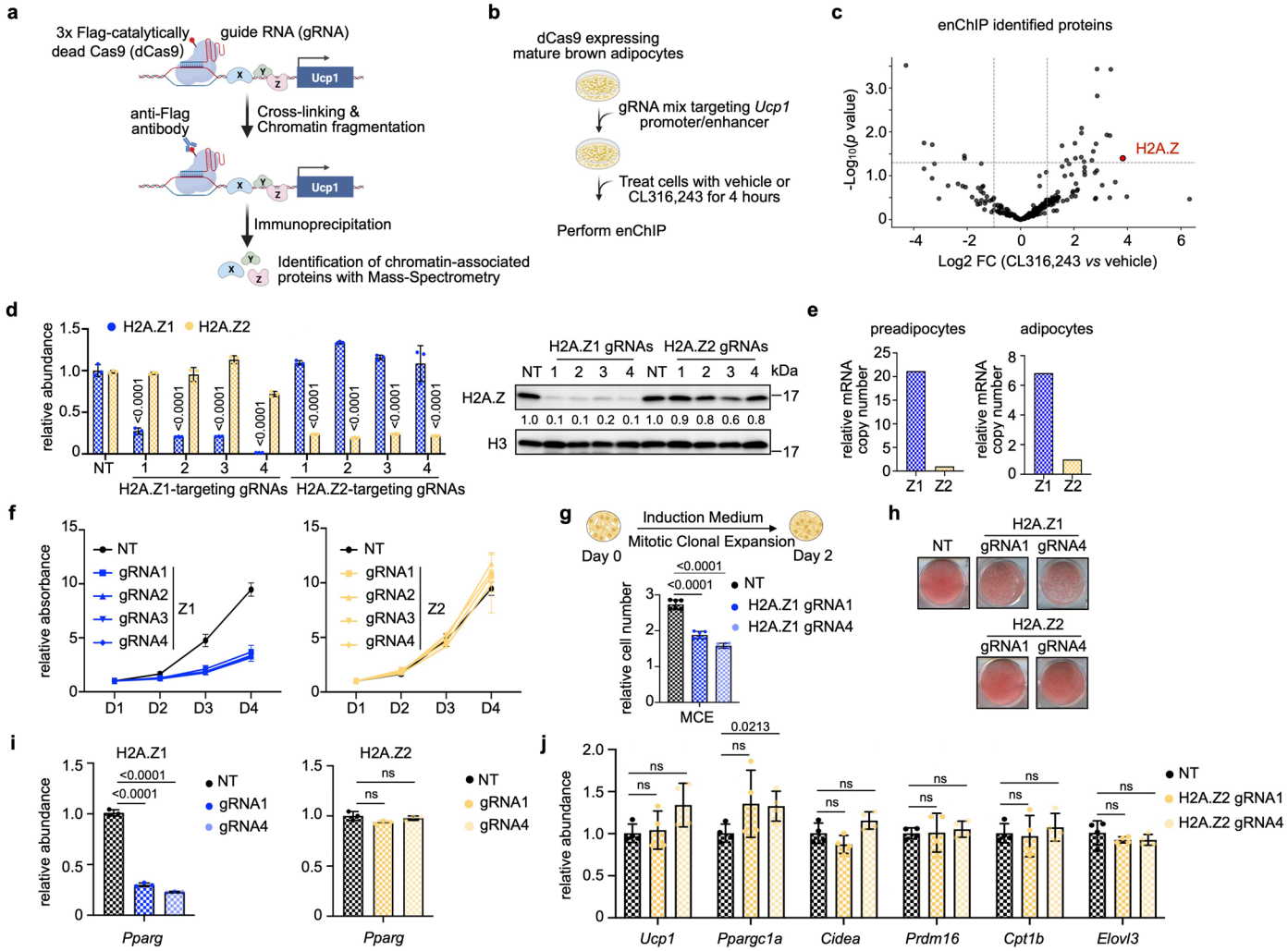

Extended Data Fig. 4 | Knockdown of H2A.Z1, but not H2A.Z2, impairs adipogenesis. a, Schematic showing the workflow of CRISPR-based engineered DNA-binding molecule-mediated chromatin immunoprecipitation (enChIP). **b**, Scheme of the experimental design for enChIP in brown adipocytes treated with either vehicle or 1 μM CL316,243 for 4 h. $N = 3$ biological replicates per group. **c**, Volcano plot showing changes in protein abundance profiled by mass spectrometry analysis of purified proteins from enChIP in vehicle-treated (vehicle) and CL316,243-treated (CL316,243) brown adipocytes. β3-AR stimulation-enriched proteins were defined with a Log2 fold change (Log2 FC) > 1 and a p-value < 0.05. Statistical significance was determined using a two-sided Student's t-test, with p-values adjusted using the Benjamini-Hochberg. **d**, Expression and protein levels of H2A.Z1 and H2A.Z2 in non-targeting (NT) control and isoform-specific CRISPR/gRNA-mediated knockdown adipocytes. $N = 3$ technical replicates per group for qRT-PCR analysis. The relative abundance of H2A.Z protein was determined using ImageJ, normalized to each corresponding H3 signal and the NT control (set as 1.0), and labeled underneath. **e**, Relative mRNA copy number of H2A.Z1 and H2A.Z2 in brown preadipocytes and mature adipocytes. **f**, Growth curve of non-targeting (NT) control preadipocytes and isoform-specific CRISPR/gRNA-mediated H2A.Z1 or H2A.Z2 knockdown preadipocytes. The number of cells was determined by crystal violet staining. $N = 3$ technical replicates per group. **g**, H2A.Z1 knockdown mediated by isoform-specific CRISPR/gRNAs impairs mitotic clonal expansion (MCE) during adipocyte differentiation. Top, schematic showing the MCE process. Bottom, the relative cell number was determined by crystal violet staining after MCE. $N = 6$ technical replicates per group. **h**, Oil Red O staining for the non-targeting (NT) control and isoform-specific CRISPR/gRNA-mediated H2A.Z1 or H2A.Z2 knockdown adipocytes. **i**, Expression levels of adipogenic marker (Pparg) in the non-targeting (NT) control and isoform-specific CRISPR/gRNA-mediated H2A.Z1 (left, gRNA1 and gRNA4) or H2A.Z2 (right, gRNA1 and gRNA4) knockdown adipocytes. $N = 3$ technical replicates per group. **j**, Expression of thermogenic genes in the non-targeting (NT) control and H2A.Z2 knockdown (gRNA1 and gRNA4) adipocytes. $N = 4$ technical replicates per group. In **d**-**j**, the data shown are from one of two biological replicates with similar results. In **d**, **g**, **i**, and **j**, the error bars indicate the mean ± s.d. of technical replicates in each group. Differences were assessed with two-sided unpaired t test. p value > 0.05 (NS, not significant). Icons in **a**, **b** and **g** created in BioRender; Tseng, Y. https://biorender.com/iu0x6dt (2026).

https://doi.org/10.1038/s42255-026-01510-2

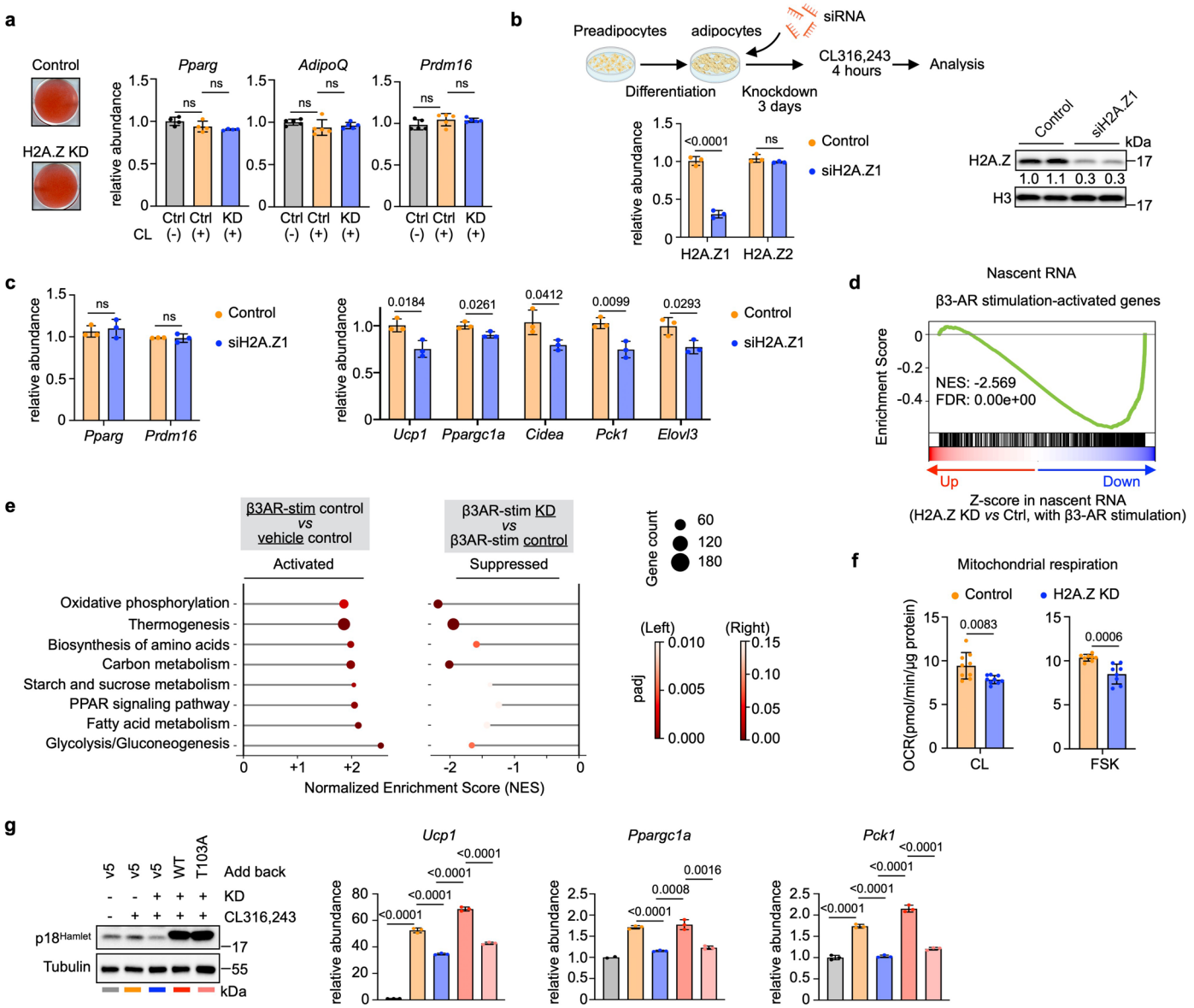

Extended Data Fig. 5 | Knockdown of H2A.Z1 impairs gene activation in the thermogenic program. a, Left, Oil Red O staining of the control and shRNA-mediated H2A.Z knockdown (H2A.Z KD) in mature adipocytes. Right, expression levels of BAT adipogenic markers in the control (Ctrl) and H2A.Z KD adipocytes following vehicle or 1 μM CL316,243 (CL) treatment for 4 h. $N = 4$ technical replicates per group for *Pparg* and $n = 5$ technical replicates per group for *AdipoQ and Prdm16* qRT-PCR. **b**, Top, schematic showing the experimental design for knocking down H2A.Z1 in mature adipocytes using siRNA. Non-targeting siRNA was used as a control. Bottom left, expression levels of H2A.Z1 and H2A.Z2 in the control and siRNA-mediated H2A.Z1 knockdown (siH2AZ.1) adipocytes. $N = 3$ technical replicates per group. Bottom right, H2A.Z protein levels in the control and siH2A.Z1 adipocytes. The relative abundance of H2A.Z protein was determined using ImageJ, normalized to each corresponding H3 signal and the first control sample (set as 1.0), and labeled underneath. **c**, Expression of BAT adipogenic markers (left) and thermogenic genes (right) in control and siRNA-mediated H2A.Z1 knockdown adipocytes following vehicle or 1 μM CL316,243 (CL) treatment for 4 h. $N = 3$ technical replicates per group. **d**, Gene set enrichment analysis (GSEA) for genes exhibiting increased transcription upon β3-AR stimulation in H2A.Z knockdown adipocytes. A negative enrichment score in y-axis signifies the downregulation of genes in β3-AR stimulated H2A.Z knockdown adipocytes. $N = 2$ biological replicates per group for PRO-seq. **e**, Gene set enrichment analysis (GSEA) for pathways related to the key functions of brown adipocytes. Left, pathways pivotal for the thermogenic activity in brown adipocytes are upregulated upon β3-AR stimulation. Right, these pathways are downregulated by H2A.Z knockdown upon β3-AR stimulation. $N = 3$ biological replicates for RNA-seq. **f**, Oxygen consumption rate (OCR) in the control and H2A.Z knockdown (KD) adipocytes in response to β3-AR signaling (CL316,243, CL, $n = 9$ technical replicates per group; Forskolin, FSK, $n = 8$ technical replicates per group). Adipocytes were pretreated with 1 μM CL316,243 overnight before the Seahorse analysis. **g**, $p18^{Hamlet}$ knockdown (KD) rescue experiment. Left, protein level of $p18^{Hamlet}$ in control and $p18^{Hamlet}$ KD and add back groups. v5, empty vector expressing v5 tag. WT, wild type $p18^{Hamlet}$. T103A, $p18^{Hamlet}$ T103A mutant. Right, expression of *Ucp1*, *Ppargc1a*, and *Pck1* under differentiate conditions. $N = 3$ technical replicates per group for qRT-PCR, except for *Ppargc1a* (vehicle treated v5 group), where $n = 2$. In **a**-**c**, **f**, and **g**, the data shown are from one of two biological replicates with similar results, and the error bars indicate the mean ± s.d. of technical replicates in each group. Differences were assessed with two-sided unpaired *t* test. *p* value > 0.05 (not significant, ns). Icon in **b** created in BioRender; Tseng, Y. https://biorender.com/iu0x6dt (2026).

https://doi.org/10.1038/s42255-026-01510-2

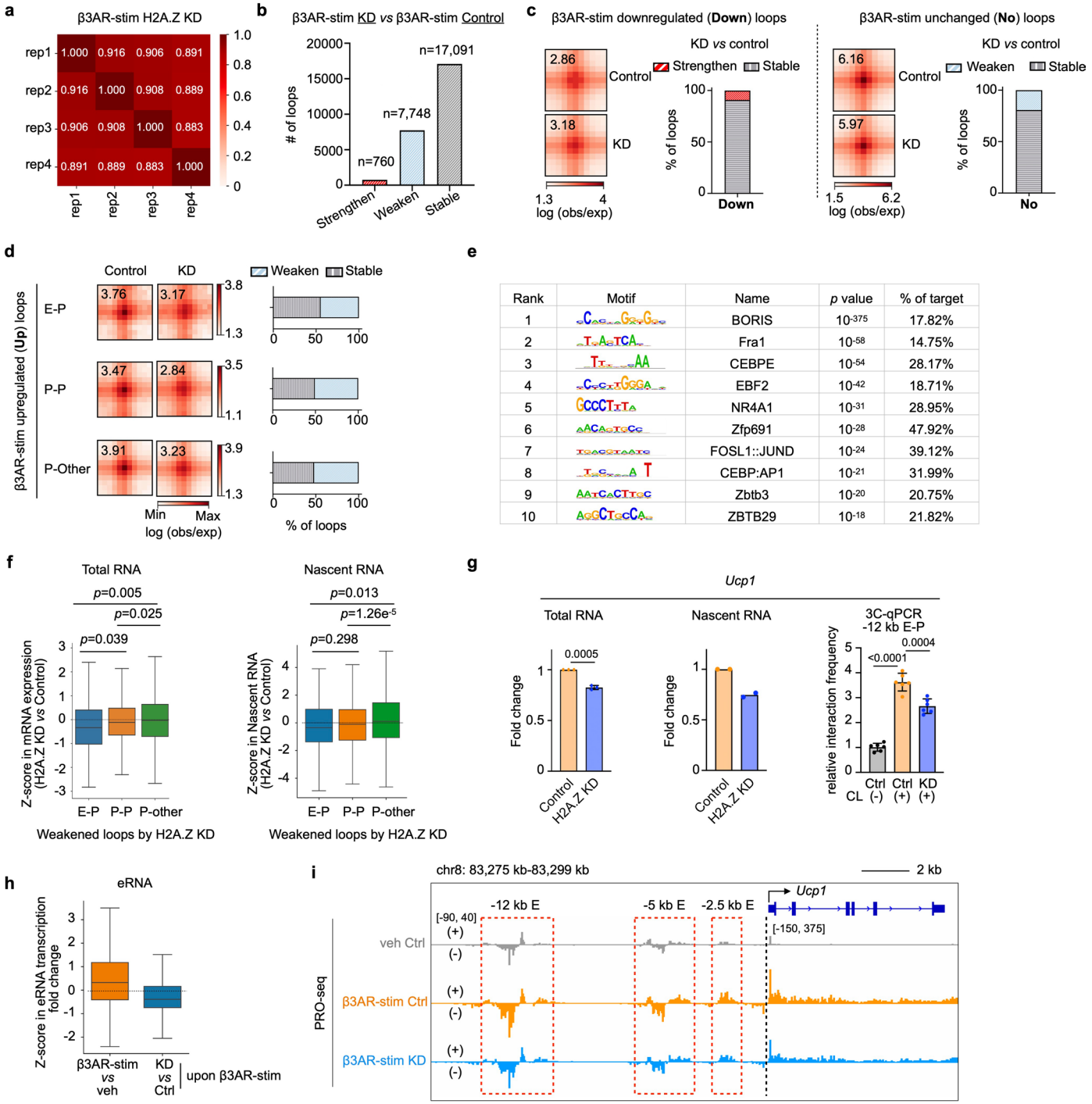

Extended Data Fig. 6 | See next page for caption.

https://doi.org/10.1038/s42255-026-01510-2

Extended Data Fig. 6 | Chromatin loop analysis in H2A.Z knockdown adipocytes in response to β3-AR stimulation. a, Heatmap showing reproducibility of Micro-C interaction frequencies among four biological replicates from β3-AR-stimulated H2A.Z knockdown mouse brown adipocytes. **b**, Number of loops that are strengthened (Strengthen, red), weakened (Weaken, blue), or unaffected (Stable, gray) by H2A.Z knockdown upon β3-AR stimulation. **c**, Averaged contact signals (aggregate peak analysis, APA) plotted for β3-AR stimulation downregulated (Down) (Left) or β3-AR stimulation unchanged (No) (Right) loops in the β3-AR-stimulated control and β3-AR-stimulated H2A.Z knockdown (KD) adipocytes. Bat plots showing the percentage of strengthened (Strengthen), weakened (Weaken), or unaffected (Stable) loops by H2A.Z knockdown. **d**, Left, averaged contact signals (aggregate peak analysis, APA) plotted for β3-AR stimulation-upregulated E-P, P-P, or P-other loops in β3-AR-stimulated control (Control) and β3-AR-stimulated H2A.Z knockdown (KD) brown adipocytes. Right, bar plots showing the percentages of weakened (Weaken) and unaffected (Stable) loops by H2A.Z knockdown for each category of loops. **e**, Motif analysis for non H2A.Z-dependent loop anchors. The top 10 motifs identified by HOMER are shown. **f**, Boxplots showing the distribution of z-scores for gene expression (left) and transcription (right) of genes associated with chromatin loops weakened by H2A.Z knockdown upon β3-AR stimulation. Genes were grouped based on loop type: E–P (n = 112 for expression, n = 116 for transcription), P–P (n = 1,099 for expression, n = 1,166 for transcription), or P–other (n = 909 for expression, n = 1,025 for transcription). p value, two-sided wilcoxon test. Boxplots show median (center line), 25th-75th percentiles (box) and 1.5 x IQR (whiskers). **g**, Two bar plots on the left showing the fold changes in *Ucp1* expression and transcription quantified by RNA-seq and PRO-seq, respectively. Error bar represents the mean ± s.d. of three biological replicates for RNA-seq. P adjust ($padj$), two-sided Wald test implemented in DESeq2. Bar plot on the right showing 3C-qPCR analysis of interaction frequency of −12 kb E-P loops in control (Ctrl) and H2A.Z knockdown (KD) adipocytes. Cells were treated with vehicle or 1 μM CL316,243 (CL) for 4 h before analysis. N = 6 technical replicates per group for qPCR. Error bar represents the mean ± s.d. of technical replicates in each condition. Differences were assessed with two-sided unpaired t test. **h**, Boxplot showing the distribution of z-scores in transcription changes of eRNAs (n = 333) associated E-P loops that were upregulated upon β3-AR stimulation (β3AR-stim) but weakened by H2A.Z knockdown (KD) in response to β3-AR signaling. Boxplots show median (center line), 25th-75th percentiles (box) and 1.5 x IQR (whiskers). **i**, Representative Integrative Genomics Viewer (IGV) tracks of *Ucp1* locus highlighting PRO-seq data in vehicle-treated control (veh Ctrl, gray), β3-AR-stimulated control (β3AR-stim Ctrl, orange), and β3-AR-stimulated H2A.Z KD (β3AR-stim KD, blue) adipocytes. The three upstream enhancers of *Ucp1* are highlighted with red rectangle. PRO-seq data from two biological replicates were combined and tracks feature adjusted y-axis scale.

https://doi.org/10.1038/s42255-026-01510-2

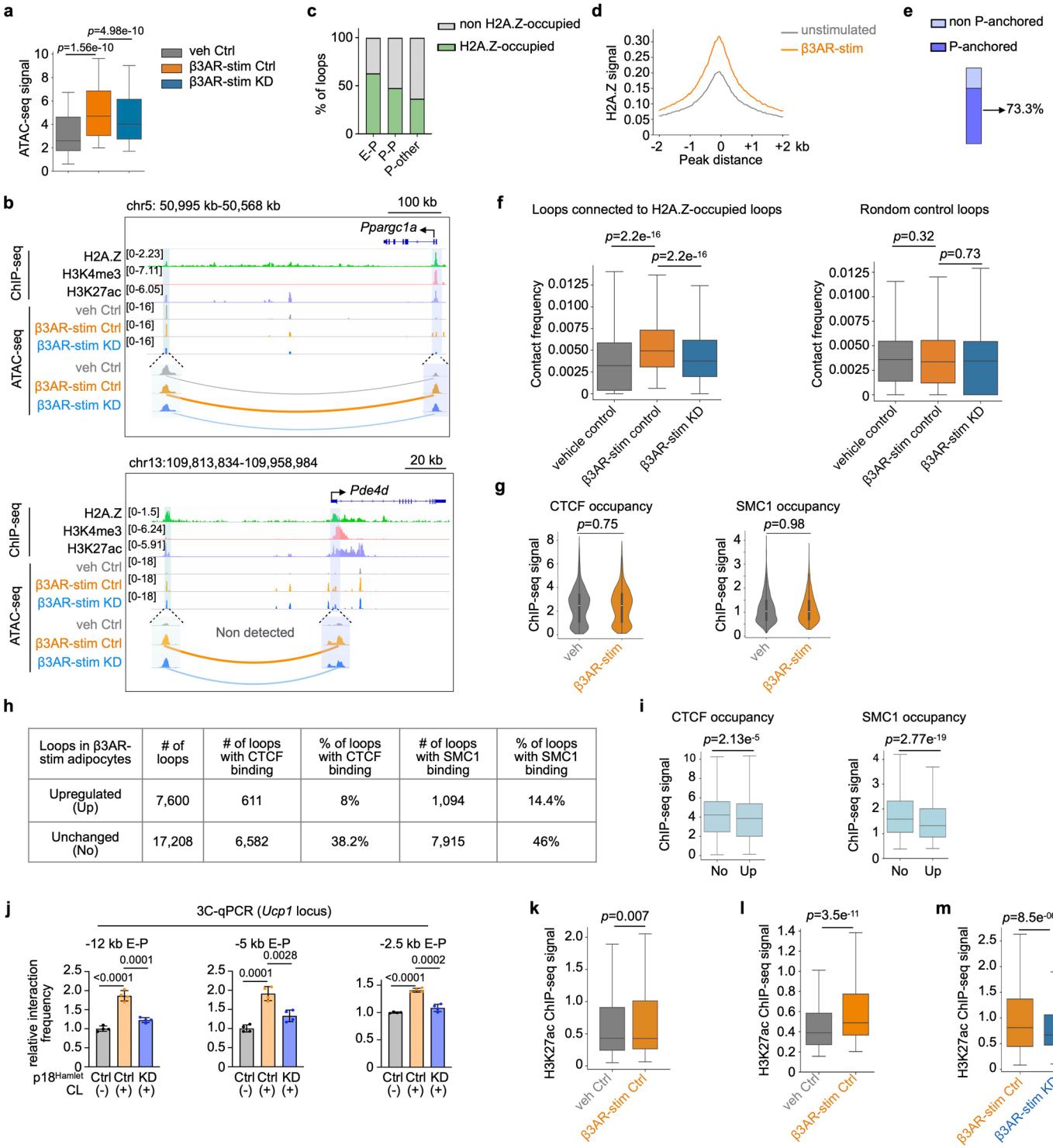

Loops in β3AR-stim adipocytes	# of loops	# of loops with CTCF binding	% of loops with CTCF binding	# of loops with SMC1 binding	% of loops with SMC1 binding
Upregulated (Up)	7,600	611	8%	1,094	14.4%
Unchanged (No)	17,208	6,582	38.2%	7,915	46%

Extended Data Fig. 7 | See next page for caption.

https://doi.org/10.1038/s42255-026-01510-2

Extended Data Fig. 7 | Decreased chromatin accessibility caused by H2A.Z knockdown is associated with weakened chromatin loop formation. **a**, Boxplot showing the averaged ATAC-seq signals (n = 39) at H2A.Z-occupied anchors of β3-AR-stimulated upregulated E-P loops linked to upregulated genes. **b**, Representative examples (*Ppargc1a* and *Pde4d* locus) showing coordinated changes in ATAC-seq signals and chromatin loops across three conditions. The colored arched lines represent differential chromatin loops in each condition, with varying thicknesses indicating relative contact frequencies based on the Micro-C data. The ChIP-seq and ATAC-seq data were visualized using Integrative Genomics Viewer (IGV), and the data shown are from one of two or three biological replicates with similar results. **c**, Bar plot showing the percentage of H2A.Z-dependent loops with H2A.Z binding (H2A.Z-occupied loops). **d**, Composite plot showing the averaged CUT&RUN H2A.Z signals at the anchors of H2A.Z-dependent loops from primary brown adipocytes isolated from mice with or without 4 h cold exposure, conditions corresponding to with or without activation of β3-AR signaling. **e**, Bar plot showing the percentage of promoter-anchored (P-anchored) loops for H2A.Z-occupoed loops. **f**, Left, boxplot showing contact frequency of loops (n = 10,746) connected to H2A.Z-occupied loops within networks in three conditions. Right, boxplot showing contact frequency of random selected loops (n = 1,000). **g**, Violin plots showing the distribution of co-bound CTCF and SMC1 signals (n = 1,966) at H2A.Z-occupied anchors of dependent loops in vehicle-treated (veh, gray) and β3-AR-stimulated (β3AR-stim, orange) adipocytes. **h**, Table showing the percentage of β3-AR stimulation-upregulated (Up) or unchanged (No) loops with CTCF (co-bound with SMC1) or SMC1 binding at both anchors in β3-AR-stimulated brown adipocytes. **i**, Boxplot showing CTCF (co-bound with SMC1) or SMC1 signal intensity at the anchors of their occupied β3-AR stimulation-upregulated (Up, n = 1,220) or unchanged (No, n = 6,862) loops in β3-AR-stimulated brown adipocytes. **j**, 3C-qPCR analysis of three *Ucp1*-assocaited E-P loops in control (Ctrl) and $p18^{Hamlet}$ knockdown (KD) adipocytes following vehicle or 1 μM CL316,243 (CL) treatment for 4 h. N = 4 technical replicates per group. Data shown are from one of two biological replicates with similar results, and error bars indicate the mean ± s.d. of technical replicates in each group. Differences were assessed with two-sided unpaired t test. **k**, Boxplot showing H3K27ac ChIP-seq signal (n = 197) intensities at the enhancer anchors of H2A.Z-occupied loops during thermogenesis. **l**, Boxplot showing β3-AR stimulation-upregulated (Log2 fold change>0) H3K27ac ChIP-seq signals (n = 115) at the enhancer anchors of H2A.Z-occupied loops during thermogenesis. **m**, Boxplot showing β3-AR stimulation-upregulated (Log2 fold change>0) H3K27ac ChIP-seq signals (n = 115) at the enhancer anchors of H2A.Z-occupied loops upon H2A.Z knockdown. In **a**, **f**, **g**, **i**, and **k**-**m**, p value, two-sided wilcoxon test. In **a, f, i** and **k**-**m**, Boxplot shows median (center line), 25th-75th percentiles (box) and 1.5 x IQR (whiskers). In **g**, Violin plots show median (dot), 25th-75th percentiles (bar) and 1.5 x IQR (whiskers).

https://doi.org/10.1038/s42255-026-01510-2

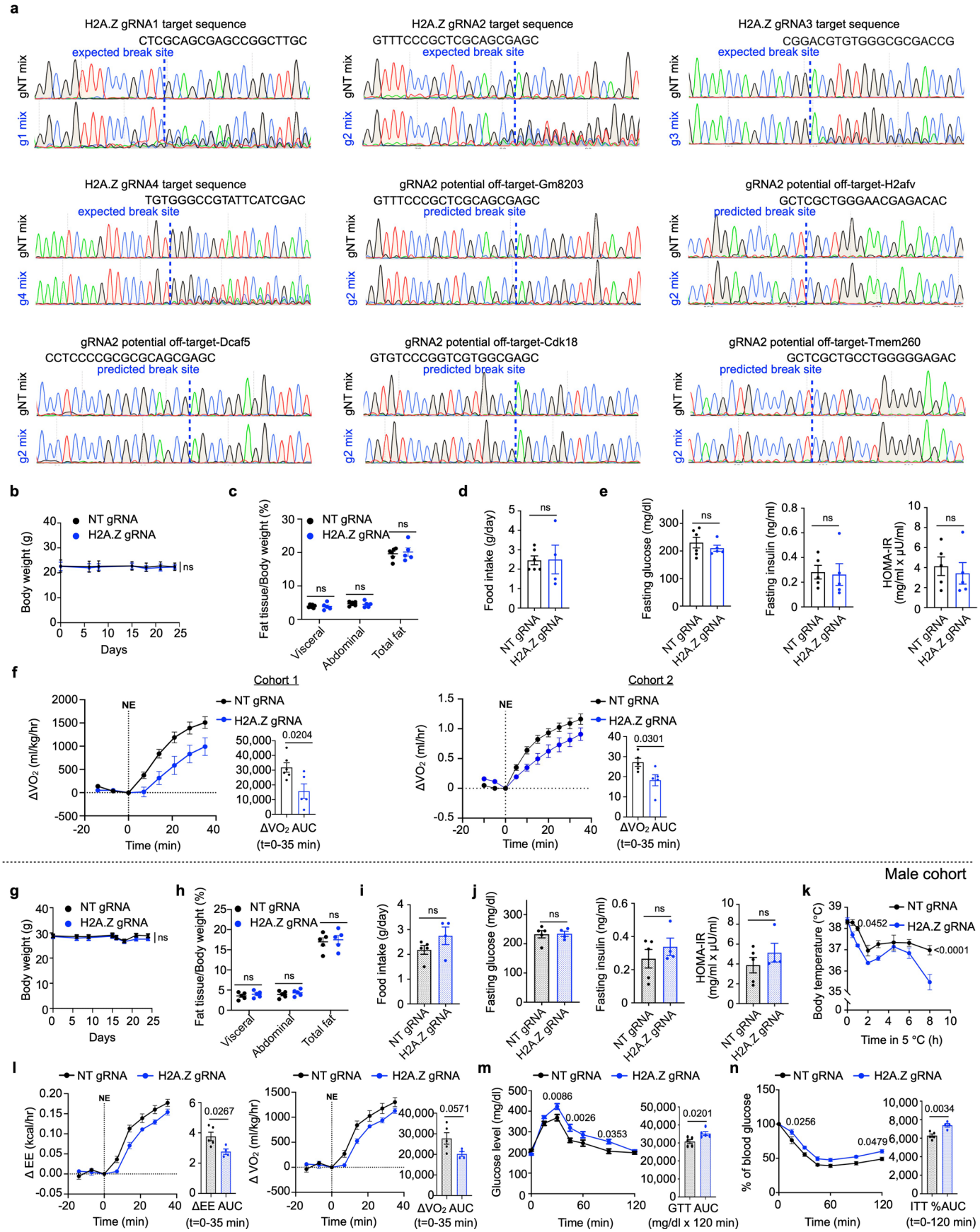

Extended Data Fig. 8 | See next page for caption.

https://doi.org/10.1038/s42255-026-01510-2

Extended Data Fig. 8 | H2A.Z is crucial for BAT thermogenic capacity. **a**, Snapshots of sanger sequencing results of genomic DNA PCR products from BAT received non-targeting control gRNA (gNT) or four individual gRNAs targeting H2A.Z (gRNA1-4). Genome editing was assessed at expected break sites for gRNA1-4. Additionally, for gRNA2, genome editing at potential off-target sites was also checked. **b**, Body mass of the female control and H2A.Z-deficient mice. $N = 6$ mice for NT gRNA and $n = 5$ mice for H2A.Z gRNA group. **c**, Percentages of fat mass of the female control and H2A.Z-deficient mice. $N = 6$ mice for NT gRNA and $n = 5$ mice for H2A.Z gRNA group. **d**, Food intake of the female control and H2A.Z-deficient mice $N = 6$ mice for NT gRNA and $n = 4$ mice for H2A.Z gRNA group. **e**, Left, fasting glucose levels in female control and H2A.Z-deficient mice. $N = 6$ mice for NT gRNA and $n = 5$ mice for H2A.Z gRNA group. Middle and right, fasting insulin and Homeostatic Model Assessment for Insulin Resistance (HOMA-IR) levels in female control and H2A.Z-deficient mice. $N = 5$ mice per group. **f**, Oxygen consumption (VO_2) was measured using CLAMS system (left) or Promethion system (right) in female control and H2A.Z-deficient mice that were stimulated with an intraperitoneal (i.p.) injection of NE (1 mg/kg). Bar plot showing the quantification of the area under the curve (AUC). $N = 6$ mice for NT gRNA and $n = 5$ mice for H2A.Z gRNA group for CLAMS system. $N = 5$ mice per group for Promethion system. **g**,**h**, Body mass (g) and percentages of fat mass (h) of male control and H2A.Z-deficient mice. $N = 5$ mice per group. **i**, Food intake of male control and H2A.Z-deficient mice. $N = 5$ mice for NT gRNA and $n = 4$ mice for H2A.Z gRNA group. **j**, Fasting glucose, fasting insulin, and HOMA-IR levels in male control and H2A.Z-deficient mice. $N = 5$ mice for NT gRNA and $n = 4$ mice for H2A.Z gRNA group. **k**, Core body temperature of the male control and H2A.Z-deficient mice that were challenged at 5°C for 8 h. $N = 5$ mice per group. **l**, Energy expenditure (EE) (left) and oxygen consumption (VO_2) (right) were measured by CLAMS system in male control and H2A.Z-deficient mice that were stimulated with an intraperitoneal (i.p.) injection of NE (1 mg/kg). Bar plot showing the quantification of the area under the curve (AUC) for EE and VO_2. $N = 5$ mice for NT gRNA and $n = 4$ mice for H2A.Z gRNA group. **m**, Glucose tolerance test (GTT) results for the male control and H2A.Z-deficient mice. Bar plot showing the quantification of the area under the curve (AUC) in the GTT. $N = 5$ mice per group. **n**, Insulin tolerance test (ITT) results for the male control and H2A.Z deficient mice. Bar plot showing the quantification of the % area under the curve (AUC) in the ITT. $N = 5$ mice for NT gRNA and $n = 4$ mice for H2A.Z gRNA group. In **b**-**n** error bars indicate the mean ± s.e.m. of biological replicates in each group. Two-way ANOVA test in **b**, **f, g**, and **k**-**n** line charts. Differences were assessed with two-sided unpaired *t* test in **c**-**f, h**-**j**, and **l**-**n** bar plots. *p* value > 0.05 (not significant, ns).

https://doi.org/10.1038/s42255-026-01510-2

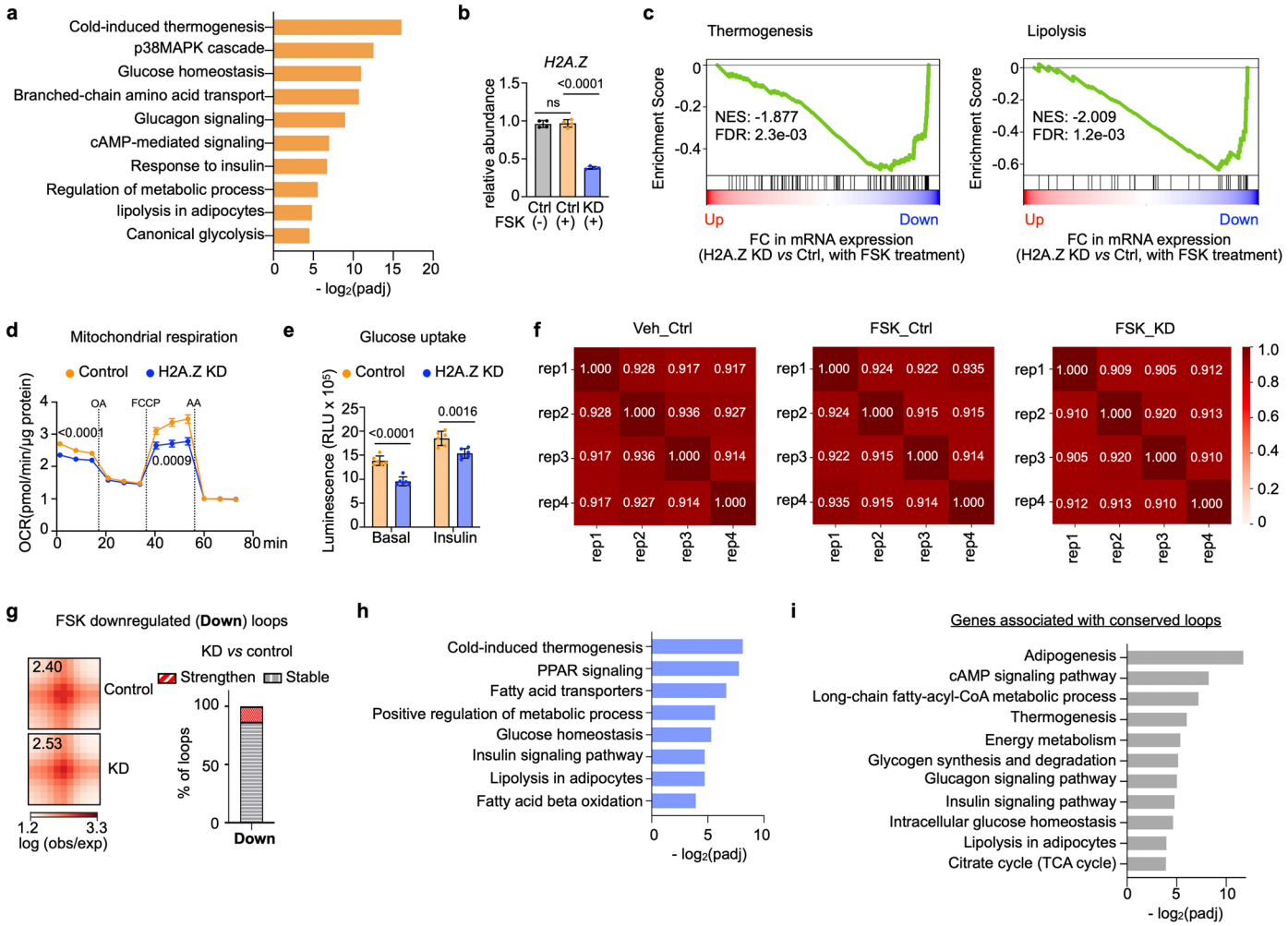

Extended Data Fig. 9 | H2A.Z is required for the formation of dynamically gained loops and gene activation during thermogenesis in human brown adipocytes. a, Functional enrichment analysis for forskolin (FSK) treatment-upregulated genes (log_2 fold changes > 0 and an adjusted *p*-value < 0.05) in primary human brown adipocytes. Selected brown adipocyte-related terms are shown. The x-axis shows the statistical significance (-log_2 adjusted *p* value, -log_2(padj)). **b**, Expression of H2A.Z in control (Ctrl) and H2A.Z knockdown (KD) primary human brown adipocytes. Adipocytes were treated with vehicle or 10 μM forskolin (FSK) for 4 h before analysis. *N* = 4 technical replicates per group for qRT-PCR. **c**, Gene set enrichment analysis (GSEA) for Thermogenesis and Lipolysis pathways upon H2A.Z knockdown with FSK treatment. Negative enrichment scores in y-axis signify the downregulation of the pathway upon H2A.Z knockdown. *N* = 3 biological replicates per group for RNA-seq. **d**, Oxygen consumption rate (OCR) in the control and H2A.Z knockdown (KD) human brown adipocytes in response to FCCP (uncoupler of mitochondrial oxidative phosphorylation, maximal respiration) stimulation. Oligomycin (OA, ATP production respiration). Antimycin A (AA, non-mitochondrial respiration). OCR was normalized to the protein content. Adipocytes were pretreated with 10 μM FSK overnight before the Seahorse analysis. *N* = 9 technical replicates per group. **e**, Glucose uptake in the control and H2A.Z knockdown (KD) human brown adipocytes. Adipocytes were pretreated with 10 μM FSK overnight before the experiment. *N* = 6 technical replicates per group. **f**, Heatmap showing reproducibility of Micro-C interaction frequencies among four replicates from vehicle-treated control (Veh_Ctrl), FSK-treated control (FSK_Ctrl), and FSK-treated H2A.Z knockdown (FSK_KD) primary human brown adipocytes. The reproducibility score was determined by HiCRep. **g**, Left, averaged contact signals (aggregate peak analysis, APA) plotted for FSK treatment downregulated (Down) loops in the control and H2A.Z KD adipocytes upon FSK treatment. Right, bar plot showing the percentage of strengthened (Strengthen) and unaffected (Stable) loops by H2A.Z knockdown. **h**, Functional enrichment analysis for H2A.Z knockdown-downregulated genes associated with loops showing reduced contact frequency upon knockdown. Selected brown adipocyte-related terms are shown. The x-axis shows the statistical significance (-log_2 adjusted *p* value, -log_2(padj)). **i**, Functional enrichment analysis for genes associated with conserved promoter-anchored chromatin loops. Selected brown adipocyte-related terms are shown. The x-axis shows the statistical significance (-log_2 adjusted *p* value, -log_2(padj)). In **b**, **d**, and **e**, the data shown are from one of two biological replicates with similar results, and error bars indicate the mean ± s.d. of technical replicates in each group. Differences were assessed with two-sided unpaired *t* test. *p* value > 0.05 (not significant, ns). In **a**, **h**, and **i**, gene set enrichment was performed using Enrichr (one-sided Fisher's exact test with Benjamini–Hochberg correction).

nature portfolio

Corresponding author(s): Yu-Hua Tseng, Kaifu Chen

Last updated by author(s): Feb 18, 2026

Reporting Summary

Nature Portfolio wishes to improve the reproducibility of the work that we publish. This form provides structure for consistency and transparency in reporting. For further information on Nature Portfolio policies, see our Editorial Policies and the Editorial Policy Checklist.

Statistics

For all statistical analyses, confirm that the following items are present in the figure legend, table legend, main text, or Methods section.

n/a	Confirmed	
☐	☒	The exact sample size (*n*) for each experimental group/condition, given as a discrete number and unit of measurement
☐	☒	A statement on whether measurements were taken from distinct samples or whether the same sample was measured repeatedly
☐	☒	The statistical test(s) used AND whether they are one- or two-sided *Only common tests should be described solely by name; describe more complex techniques in the Methods section.*
☒	☐	A description of all covariates tested
☐	☒	A description of any assumptions or corrections, such as tests of normality and adjustment for multiple comparisons
☐	☒	A full description of the statistical parameters including central tendency (e.g. means) or other basic estimates (e.g. regression coefficient) AND variation (e.g. standard deviation) or associated estimates of uncertainty (e.g. confidence intervals)
☐	☒	For null hypothesis testing, the test statistic (e.g. *F*, *t*, *r*) with confidence intervals, effect sizes, degrees of freedom and *P* value noted *Give P values as exact values whenever suitable.*
☒	☐	For Bayesian analysis, information on the choice of priors and Markov chain Monte Carlo settings
☒	☐	For hierarchical and complex designs, identification of the appropriate level for tests and full reporting of outcomes
☐	☒	Estimates of effect sizes (e.g. Cohen's *d*, Pearson's *r*), indicating how they were calculated

Our web collection on statistics for biologists contains articles on many of the points above.

Software and code

Policy information about availability of computer code

Data collection	The Micro-C, RNA-seq, ATAC-seq, and ChIP-seq for H3K27ac and H3K4me3 libraries generated in murine brown adipocytes were sequenced with a NextSeq 500 Instrument (Illumina). The ChIP-seq libraries for H2A.Z generated in murine brown adipocytes were sequenced with a HiSeq 2500 Instrument (Illumina). The CUT&RUN libraries for H2A.Z generated in primary murine brown adipocytes were sequenced by BGI Genomics (BGISEQ-500). The PRO-seq and ChIP-seq for CTCF, SMC1, and MED1 libraries generated in murine brown adipocytes were sequenced with a Novaseq X Plus Instrument (Illumina).The Micro-C, RNA-seq, and ChIP-seq for H3K27ac and H2A.Z libraries generated in primary human brown adipocytes were sequenced with a Novaseq X Plus Instrument (Illumina). qPCR: ABI Prism 7900 sequence-detection system Western blotting: Bio-Red ChemiDoc Imaging System Cell proliferation, Oil Red O and in vitro glucose uptake: GloMax Discover Microplate Reader (Promega) Seahorse: Seahorse Extracellular Flux Analyzer (Seahorse Bioscience Inc.) Core body temperature: aRET-3 rectal probe (Physitemp) Blood glucose: InfinityO Blood Glucose Meter (US Diagnostics) Indirect calorimetry: Columbus Instruments' Oxymax-Comprehensive Lab Animal Monitoring System (CLAMS) and Sable Systems' Promethion system Body composition analysis: dual-energy X-ray absorptiometry (DEXA)
Data analysis	GraphPad Prism (version 8.0 and 10); Image J (version 1.53) was used for quantification of of western blotting results; Micro-C analysis: Galore (version 0.6.6), BWA (version 0.7.17-r1188), pairtools (version 1.0.0), COOLER (version 0.9.1), JUICER (version 1.22.01), peakachu (downloaded at July 2023), BedTools (version 2.31.0), pybedtools (version 0.9.1); hicrep (version 0.2.6), AdaLiftOver (1.0.0) RNA-seq analysis: Galore (version 0.6.6), STAR (version 2.7.9a), deepTools (version 3.3.1), SamTools (version 1.16.1), DESeq2 (version 1.32.0), fgsea (version 1.18.0), gseapy (version 1.0.6);

ChIP-seq and ATAC-seq analysis: CHIPs pipeline (https://github.com/liulab-dfci/CHIPS), DANPOS2, BedTools (version 2.31.0), pybedtools (version 0.9.1), pyBigWig (version 0.3.20);
Functional enrichment analysis: Enrichr;
All the scripts used to generate the figures in this study can be found at https://github.com/zhengrongbin/brown_adipo_loop_H2AZ_paper

For manuscripts utilizing custom algorithms or software that are central to the research but not yet described in published literature, software must be made available to editors and reviewers. We strongly encourage code deposition in a community repository (e.g. GitHub). See the Nature Portfolio guidelines for submitting code & software for further information.

Data

Policy information about availability of data

All manuscripts must include a data availability statement. This statement should provide the following information, where applicable:

- Accession codes, unique identifiers, or web links for publicly available datasets
- A description of any restrictions on data availability
- For clinical datasets or third party data, please ensure that the statement adheres to our policy

The data generated in this study have been deposited at the Gene Expression Omnibus (GEO) under the series accession number of GSE261416 for Micro-C in murine brown adipocytes, GSE261413 for RNA-seq in murine brown adipocytes, GSE301361 for PRO-seq in murine brown adipocytes, GSE261412 for ChIP-seq of H2A.Z, H3K27ac, and H3K4me3 in murine brown adipocytes, GSE261410 for ATAC-seq in murine brown adipocytes, GSE301360 for CUT&RUN in murine brown adipocytes, GSE301366 for ChIP-seq of CTCF, SMC1, and MED1 in murine brown adipocytes, GSE301370 for Micro-C in human brown adipocytes, GSE301359 for RNA-seq in human brown adipocytes, and GSE301368 for ChIP-seq in human brown adipocytes.

Research involving human participants, their data, or biological material

Policy information about studies with human participants or human data. See also policy information about sex, gender (identity/presentation), and sexual orientation and race, ethnicity and racism.

Reporting on sex and gender	Not applicable
Reporting on race, ethnicity, or other socially relevant groupings	Not applicable
Population characteristics	Not applicable
Recruitment	Not applicable
Ethics oversight	Not applicable

Note that full information on the approval of the study protocol must also be provided in the manuscript.

Field-specific reporting

Please select the one below that is the best fit for your research. If you are not sure, read the appropriate sections before making your selection.

☒ Life sciences ☐ Behavioural & social sciences ☐ Ecological, evolutionary & environmental sciences

For a reference copy of the document with all sections, see nature.com/documents/nr-reporting-summary-flat.pdf

Life sciences study design

All studies must disclose on these points even when the disclosure is negative.

Sample size	No statistical methods were used to predetermine sample size. The sample size for our animal experiments in this study was based on our experience with experimental models, anticipated biological variables, and previous literatures. Sample numbers were described in the figure legends.
Data exclusions	All data were included in the analyses unless exclusion was required owing to documented technical errors during sample processing or non-concordant technical replicates.
Replication	All the biological experiments were repeated, at least, twice and reproduced. N values for replicates are reported throughout the manuscript. For Micro-C in murine brown adipocytes, four biological replicates were generated and combined for analysis for each condition. For Micro-C in primary human brown adipocytes, two biological replicates were generated for each condition, and for each biological replicate, two technical replicates (two libraries) were prepared, then four replicates were combined for analysis for each condition. For RNA-seq, three biological replicates were generated for each condition in murine and human brown adipocytes. For PRO-seq, two biological replicates were generated for each condition in murine brown adipocytes. For ATAC-seq, two biological replicates were generated for each condition in murine brown adipocytes. For histone marks (H3K4me3 and H3K27ac) ChIP-seq, two biological replicates were generated for b3-AR stimulated control and H2A.Z KD murine brown adipocytes, and single profiles were generated for vehicle-treated and b3-AR stimulated adipocytes and normalized by input background and IgG background, respectively. For H3K27ac ChIP-seq in primary human brown adipocytes, two technical replicates were generated for vehicle-treated and FSK-treated human brown adipocytes. For H2A.Z ChIP-seq, three biological

replicates were generated in b3-AR stimulated murine brown adipocytes and two technical replicates were generated for FSK-treated primary human brown adipocytes. For CTCF, SMC1, and MED1 ChIP-seq, two biological replicates were generated for each condition. For H2A.Z CUT&RUN, three biological replicates were generated for unstimulated and b3-AR stimulated primary murine brown adipocytes. For enChIP, three biological replicates were generated for vehicle treated and b3-AR stimulated murine brown adipocytes.

Randomization

Mice were randomly assigned at the time of weaning and AAV injection to minimize any potential bias.

Blinding

Although the primary investigators were not blinded for most of the studies, some of the sample analyses (such as sequencing, measurements of metabolic parameters in mice) were performed by other lab members or technicians of facilities who were not informed of the grouping during the analyses. All data collection and analysis were performed using standard sample preparation and bioinformatic pipelines in which all samples were treated equally.

Reporting for specific materials, systems and methods

We require information from authors about some types of materials, experimental systems and methods used in many studies. Here, indicate whether each material, system or method listed is relevant to your study. If you are not sure if a list item applies to your research, read the appropriate section before selecting a response.

Materials & experimental systems

n/a	Involved in the study
☐	☒ Antibodies
☐	☒ Eukaryotic cell lines
☒	☐ Palaeontology and archaeology
☐	☒ Animals and other organisms
☒	☐ Clinical data
☒	☐ Dual use research of concern
☒	☐ Plants

Methods

n/a	Involved in the study
☐	☒ ChIP-seq
☒	☐ Flow cytometry
☒	☐ MRI-based neuroimaging

Antibodies

Antibodies used

H2A.Z antibody (5 µg for ChIP-seq, 1:1000 for WB), Abcam, ab4171, lot#GR3402075-1; H2A.Z antibody (5 µg for ChIP-seq), Active Motif, 39943, lot#00913003; H3 antibody (1:1000 for WB), Abcam, ab1791, lot#GR3366670-1; v5 antibody (1:1000 for WB), Abcam, ab15828, lot#GR3397863-1; Tubulin antibody (1:1000 for WB), Cell Signaling, 2144, lot#9; ZNHIT1 (p18hamlet)antibody (1:1000 for WB), Invitrogen, PA5-53903, lot#WH3342448A; Phospho-Threonine (1:1000 for WB), Cell Signaling, 9381, lot#25; YL1 antibody (2µg for IP, 1:1000 for WB), Abcam, ab112055, lot#1024556-3; ACTR6 (ARP6) antibody (1:200 for WB), Santa Cruz, sc-514988, lot#H3121; H3K27ac antibody (5 µg for ChIP-seq), Active Motif, 39133, lot#31521015; H3K4me3 antibody (5 µg for ChIP-seq), Millipore Sigma, 07-473, lot#4022818; normal rabbit IgG (5 µg for ChIP-seq), Cell signaling, 2729, lot#10; anti-mouse IgG, HRP-linked antibody (1:2000 for WB), Cell signaling, 7076, lot#33; anti-rabbit IgG, HRP-linked antibody (1:2000 for WB), Cell signaling, 7074, lot#32; CTCF antibody (10 µl for ChIP-seq), Cell signaling, 3418S, lot#6; SMC1 antibody (5 µg for ChIP-seq), ThermoFisher Scientific, A300-055A, lot#6; MED1 antibody (5 µg for ChIP-seq, 1:1000 for WB), ThermoFisher Scientific, PA5-36114, lot#ZD4269742.

Validation

Antibodies applied for western blotting were validated based on the size of band (molecular weight), and the specificity of H2A.Z, ZNHIT1 (p18hamlet), and MED1 antibodies was further assessed by using samples from knockdown cells or tissues.
-H2A.Z antibody: Fig. 2b, 5b, 5j; Extended Data Fig. 4d, 5b
-H3 antibody: Fig. 2b, 5b, 5j; Extended Data Fig. 4d, 5b
-ZNHIT1 (p18hamlet) antibody: Fig. 2h, 2k; Extended Data Fig. 5g
-v5 antibody: Fig. 2h, 2i
-ACTR6 (ARP6) antibody: Fig. 2i
-YL1 antibody: Fig. 2i, 2j
-Phospho-Threonine: Fig. 2h
-Tubulin antibody: Fig. 2h, 2k, 4i; Extended Data Fig. 5g
-MED1 antibody: Fig.. 4i
Antibodies used for IP and ChIP-seq were validated by the manufacturer, tested by independent investigators (from published literature) or provided in this study.
ChIP-seq:
-H2A.Z antibody, https://www.abcam.com/products/primary-antibodies/histone-h2az-antibody-chip-grade-ab4174.html
-H2A.Z antibody,https://www.activemotif.com/catalog/details/39943
-H3K27ac antibody, https://www.activemotif.com/catalog/details/39133/histone-h3-acetyl-lys27-antibody-pab
-H3K4me3 antibody, https://www.emdmillipore.com/US/en/product/Anti-trimethyl-Histone-H3-Lys4-Antibody,MM_NF-07-473
-CTCF antibody, https://www.cellsignal.com/products/primary-antibodies/ctcf-d31h2-xp-rabbit-mab/3418?srsltid=AfmBOoqQPTJMyJAW05-Vn-aOArgnPIObfmT0djBsf4RyA6LnEBwfLHWS
-SMC1 antibody, https://www.thermofisher.com/antibody/product/SMC1-Antibody-Polyclonal/A300-055A
-MED1 antibody, https://www.thermofisher.com/antibody/product/TRAP220-Antibody-Polyclonal/PA5-36114
-Normal rabbit IgG, https://www.cellsignal.com/products/primary-antibodies/normal-rabbit-igg/2729
Immunoprecipitation (IP):
-YL1: https://www.abcam.com/products/primary-antibodies/yl1-antibody-ab112055.html

Eukaryotic cell lines

Policy information about cell lines and Sex and Gender in Research

Cell line source(s)	Cell lines used in the study include immortalized mouse brown preadipocytes (WT-1), stromal vascular fraction (SVF) isolated from BAT of C57BL/6J mice and UCP1-Cre::Cas9 mice, primary human brown preadipocytes isolated from the deep neck biopsy of a lean and metabolically healthy donor, immortalized human brown preadipocytes (A41 hBAT-SVF) and 293T Lenti-X cells. -WT-1 cells were derived from the stromal vascular fraction (SVF) of interscapular brown adipose tissue of a newborn female mouse. The SVF cells were immortalized by SV40 T antigen as described in PMID: 11113206 and PMID: 14966273. -Primary human brown preadipocytes were provided by our collaborator, Dr. Endre Kristóf. The Stromal Vascular Fraction was isolated from the deep neck adipose tissue biopsy from a 52-year-old male patient with normal body mass index did not have diabetes, malignant tumor, or abnormal thyroid hormone levels at the time of thyroid surgery. Tissue collection was approved by the Medical Research Council of Hungary (20571-2/2017/EKU) followed by the EU Member States' Directive 2004/23/EC on presumed consent practice for tissue collection. All experiments were carried out in accordance with the approved ethical regulations and the guidelines of the Helsinki Declaration. Written informed consent was obtained from the participant before the surgical procedure. -A41 hBAT-SVF were generated from the SVF of deep neck fat biopsies utilizing human telomerase reverse transcriptase (hTERT) as described in PMID: 26076036, PMID: 28244042, and PMID: 28469146. -293T Lenti-X cells were purchased from Takara and the catalog number is 632180.
Authentication	The immortalized A41 hBAT-SVF cells have been deposited to ATCC and authenticated by ATCC. The immortalized mouse brown preadipocytes (WT-1) have been deposited to Millipore Sigma and were authenticated by Millipore Sigma (#SCC255). Others were not authenticated.
Mycoplasma contamination	All the cell lines were routinely tested negative for mycoplasma contamination.
Commonly misidentified lines (See ICLAC register)	No commonly misidentified cell lines were used in the study.

Animals and other research organisms

Policy information about studies involving animals; ARRIVE guidelines recommended for reporting animal research, and Sex and Gender in Research

Laboratory animals	The Rosa26-floxed STOP-Cas9 knock-in mice (strain #: 26175), Ucp1-Cre mice (strain #: 024670), and C57BL/6J mice (strain: 000664) were purchased from the Jackson Laboratory.
Wild animals	The study did not involve wild animals.
Reporting on sex	Both male and female mice with 12-16 weeks of age were used for experiments and this was reported in the methodology.
Field-collected samples	No field collected samples.
Ethics oversight	All experimental procedures involving animals were performed in compliance with all relevant ethical regulations applied to the use of small rodents, and with the approval by the Institutional Animal Care and Use Committees (IACUC) at the Joslin Diabetes Center.

Note that full information on the approval of the study protocol must also be provided in the manuscript.

Plants

Seed stocks	Not applicable
Novel plant genotypes	Not applicable
Authentication	Not applicable

ChIP-seq

Data deposition

☒ Confirm that both raw and final processed data have been deposited in a public database such as GEO.

☒ Confirm that you have deposited or provided access to graph files (e.g. BED files) for the called peaks.

Data access links
May remain private before publication.

https://www.ncbi.nlm.nih.gov/geo/query/acc.cgi?acc=GSE261416; https://www.ncbi.nlm.nih.gov/geo/query/acc.cgi?acc=GSE261413; https://www.ncbi.nlm.nih.gov/geo/query/acc.cgi?acc=GSE301361; https://www.ncbi.nlm.nih.gov/geo/query/acc.cgi?acc=GSE261412; https://www.ncbi.nlm.nih.gov/geo/query/acc.cgi?acc=GSE261410; https://www.ncbi.nlm.nih.gov/geo/query/acc.cgi?acc=GSE301360; https://www.ncbi.nlm.nih.gov/geo/query/acc.cgi?acc=GSE301366; https://www.ncbi.nlm.nih.gov/geo/query/acc.cgi?acc=GSE301370; https://www.ncbi.nlm.nih.gov/geo/query/acc.cgi?acc=GSE301359; https://www.ncbi.nlm.nih.gov/geo/query/acc.cgi?acc=GSE301368

Files in database submission

IgG, vehicle BAs
input, vehicle BAs
H3K4me3, vehicle BAs
H3K27ac, vehicle BAs
IgG, β3-AR-stimulated BAs
input, β3-AR-stimulated BAs
H3K4me3, β3-AR-stimulated BAs
H3K27ac, β3-AR-stimulated BAs
H3K27ac, β3-AR-stimulated control BAs, rep1
H3K27ac, β3-AR-stimulated control BAs, rep2
H3K4me3, β3-AR-stimulated control BAs, rep1
H3K4me3, β3-AR-stimulated control BAs, rep2
IgG, β3-AR-stimulated control BAs
H3K27ac, β3-AR-stimulated H2A.Z KD BAs, rep1
H3K27ac, β3-AR-stimulated H2A.Z KD BAs, rep2
H3K4me3, β3-AR-stimulated H2A.Z KD BAs, rep1
H3K4me3, β3-AR-stimulated H2A.Z KD BAs, rep2
IgG, β3-AR-stimulated H2A.Z KD BAs
H2A.Z, β3-AR-stimulated BAs, rep1
H2A.Z, β3-AR-stimulated BAs, rep2
H2A.Z, β3-AR-stimulated BAs, rep3
IgG for H2A.Z rep1
IgG for H2A.Z rep2
IgG for H2A.Z rep3
Input for CTCF, vehicle-treated control BAs-rep1
Input for CTCF, vehicle-treated control BAs-rep2
Input for CTCF, β3-AR-stimulated control BAs, rep1
Input for CTCF, β3-AR-stimulated control BAs, rep2
CTCF, vehicle-treated control BAs-rep1
CTCF, vehicle-treated control BAs-rep2
CTCF, β3-AR-stimulated control BAs, rep1
CTCF, β3-AR-stimulated control BAs, rep2
Input for SMC1 and MED1, vehicle-treated control BAs-rep1
Input for SMC1 and MED1, vehicle-treated control BAs-rep2
Input for SMC1 and MED1, β3-AR-stimulated control BAs-rep1
Input for SMC1 and MED1, β3-AR-stimulated control BAs-rep2
Input for MED1, β3-AR-stimulated H2A.Z KD BAs-rep1
Input for MED1, β3-AR-stimulated H2A.Z KD BAs-rep2
SMC1, vehicle-treated control BAs-rep1
SMC1, vehicle-treated control BAs-rep2
SMC1, β3-AR-stimulated control BAs-rep1
SMC1, β3-AR-stimulated control BAs-rep2
MED1, β3-AR-stimulated H2A.Z KD BAs-rep1
MED1, β3-AR-stimulated H2A.Z KD BAs-rep2
MED1, vehicle-treated control BAs-rep1
MED1, vehicle-treated control BAs-rep2
MED1, β3-AR-stimulated control BAs-rep1
MED1, β3-AR-stimulated control BAs-rep2
Input, vehicle-treated control human BAs-rep1
Input, vehicle-treated control human BAs-rep2
H3K27ac, vehicle-treated control human BAs-rep1
H3K27ac, vehicle-treated control human BAs-rep2
Input, FSK-treated control human BAs-rep1
Input, FSK-treated control human BAs-rep2
H3K27ac, FSK-treated control human BAs-rep1
H3K27ac, FSK-treated control human BAs-rep2
H2A.Z, FSK-treated control human BAs-rep1
H2A.Z, FSK-treated control human BAs-rep2

Genome browser session
(e.g. UCSC)

IGV: https://tinyurl.com/ycqtx33d

Methodology

Replicates

For ChIP-seq for H2A.Z, three biological replicates were generated for b3-AR stimulated murine brown adipocytes and two technical replicates for generated for FSK-treated human primary human brown adipocytes. For ChIP-seq for histone marks (H3K4me3 and H3K27ac), two biological replicates were generated for b3-AR stimulated control and H2A.Z KD murine brown adipocytes, and single profiles were generated for vehicle-treated and b3-AR stimulated murien brown adipocytes and normalized by input background and

IgG background, respectively. For H3K27ac ChIP-seq in primary human brown adipocytes, two technical replicates for generated for vehicle-treated and FSK-treated human human brown adipocytes. For CTCF, SMC1, and MED1 ChIP-seq in murine brown adipocytes, two biological replicates were generated for each condition.

Sequencing depth

IgG, vehicle BAs (total reads: 34million, uniquely mapped reads: 26million, read length: 50bp, single-end)
input, vehicle BAs (total reads: 43million, uniquely mapped reads: 34million, read length: 50bp, single-end.)
H3K4me3, vehicle BAs (total reads: 34million, uniquely mapped reads: 31million, read length: 50bp, single-end.)
H3K27ac, vehicle BAs (total reads: 35million, uniquely mapped reads: 30million, read length: 50bp, single-end.)
IgG, β3-AR-stimulated BAs (total reads: 31million, uniquely mapped reads: 24million, read length: 50bp, single-end.)
input, β3-AR-stimulated BAs (total reads: 46million, uniquely mapped reads: 37million, read length: 50bp, single-end.)
H3K4me3, β3-AR-stimulated BAs (total reads: 37million, uniquely mapped reads: 34million, read length: 50bp, single-end.)
H3K27ac, β3-AR-stimulated BAs (total reads: 34million, uniquely mapped reads: 28million, read length: 50bp, single-end.)
H3K27ac, β3-AR-stimulated control BAs, rep1 (total reads: 71million, uniquely mapped reads: 62million, read length: 42bp, paired-end.)
H3K27ac, β3-AR-stimulated control BAs, rep2 (total reads: 62million, uniquely mapped reads: 54million, read length: 42bp, paired-end.)
H3K4me3, β3-AR-stimulated control BAs, rep1 (total reads: 44million, uniquely mapped reads: 38million, read length: 42bp, paired-end.)
H3K4me3, β3-AR-stimulated control BAs, rep2 (total reads: 67million, uniquely mapped reads: 58million, read length: 42bp, paired-end.)
IgG, β3-AR-stimulated control BAs (total reads: 68million, uniquely mapped reads: 54million, read length: 42bp, paired-end.)
H3K27ac, β3-AR-stimulated H2A.Z KD BAs, rep1 (total reads: 68million, uniquely mapped reads: 58million, read length: 42bp, paired-end.)
H3K27ac, β3-AR-stimulated H2A.Z KD BAs, rep2 (total reads: 75million, uniquely mapped reads: 64million, read length: 42bp, paired-end.)
H3K4me3, β3-AR-stimulated H2A.Z KD BAs, rep1 (total reads: 65million, uniquely mapped reads: 56million, read length: 42bp, paired-end.)
H3K4me3, β3-AR-stimulated H2A.Z KD BAs, rep2 (total reads: 73million, uniquely mapped reads: 63million, read length: 42bp, paired-end.)
IgG, β3-AR-stimulated H2A.Z KD BAs (total reads: 66million, uniquely mapped reads: 53million, read length: 42bp, paired-end.)
H2A.Z, β3-AR-stimulated BAs, rep1 (total reads: 95million, uniquely mapped reads: 88million, read length: 150bp, paired-end.)
H2A.Z, β3-AR-stimulated BAs, rep2 (total reads: 92million, uniquely mapped reads: 86million, read length: 150bp, paired-end.)
H2A.Z, β3-AR-stimulated BAs, rep3 (total reads: 80million, uniquely mapped reads: 75million, read length: 150bp, paired-end.)
IgG for H2A.Z rep1: total reads (total reads: 95million, uniquely mapped reads: 88million, read length: 150bp, paired-end.)
IgG for H2A.Z rep2: total reads (total reads: 93million, uniquely mapped reads: 85million, read length: 150bp, paired-end.)
IgG for H2A.Z rep3: total reads (total reads: 82million, uniquely mapped reads: 75million, read length: 150bp, paired-end.)
Input for CTCF, vehicle-treated control BAs-rep1: (total reads: 66million, uniquely mapped reads: 59million, read length: 150bp, paired-end.)
Input for CTCF, vehicle-treated control BAs-rep2: (total reads: 89million, uniquely mapped reads: 79million, read length: 150bp, paired-end.)
Input for CTCF, β3-AR-stimulated control BAs, rep1: (total reads: 68million, uniquely mapped reads: 60million, read length: 150bp, paired-end.)
Input for CTCF, β3-AR-stimulated control BAs, rep2: (total reads: 68million, uniquely mapped reads: 60million, read length: 150bp, paired-end.)
CTCF, vehicle-treated control BAs-rep1: (total reads: 68million, uniquely mapped reads: 62million, read length: 150bp, paired-end.)
CTCF, vehicle-treated control BAs-rep2: (total reads: 65million, uniquely mapped reads: 60million, read length: 150bp, paired-end.)
CTCF, β3-AR-stimulated control BAs, rep1: (total reads: 47million, uniquely mapped reads: 43million, read length: 150bp, paired-end.)
CTCF, β3-AR-stimulated control BAs, rep2: (total reads: 68million, uniquely mapped reads: 62million, read length: 150bp, paired-end.)
Input for SMC1 and MED1, vehicle-treated control BAs-rep1: (total reads: 61million, uniquely mapped reads: 54million, read length: 150bp, paired-end.)
Input for SMC1 and MED1, vehicle-treated control BAs-rep2: (total reads: 61million, uniquely mapped reads: 54million, read length: 150bp, paired-end.)
Input for SMC1 and MED1, β3-AR-stimulated control BAs-rep1: (total reads: 59million, uniquely mapped reads: 53million, read length: 150bp, paired-end.)
Input for SMC1 and MED1, β3-AR-stimulated control BAs-rep2: (total reads: 61million, uniquely mapped reads: 55million, read length: 150bp, paired-end.)
Input for MED1, β3-AR-stimulated H2A.Z KD BAs-rep1: (total reads: 55million, uniquely mapped reads: 49million, read length: 150bp, paired-end.)
Input for MED1, β3-AR-stimulated H2A.Z KD BAs-rep2: (total reads: 54million, uniquely mapped reads: 48million, read length: 150bp, paired-end.)
SMC1, vehicle-treated control BAs-rep1: (total reads: 77million, uniquely mapped reads: 70million, read length: 150bp, paired-end.)
SMC1, vehicle-treated control BAs-rep2: (total reads: 42million, uniquely mapped reads: 38million, read length: 150bp, paired-end.)
SMC1, β3-AR-stimulated control BAs-rep1: (total reads: 57million, uniquely mapped reads: 52million, read length: 150bp, paired-end.)
SMC1, β3-AR-stimulated control BAs-rep2: (total reads: 53million, uniquely mapped reads: 49million, read length: 150bp, paired-end.)
MED1, β3-AR-stimulated H2A.Z KD BAs-rep1: (total reads: 62million, uniquely mapped reads: 54million, read length: 150bp, paired-end.)
MED1, β3-AR-stimulated H2A.Z KD BAs-rep2: (total reads: 60million, uniquely mapped reads: 52million, read length: 150bp, paired-end.)
MED1, vehicle-treated control BAs-rep1: (total reads: 56million, uniquely mapped reads: 50million, read length: 150bp, paired-end.)
MED1, vehicle-treated control BAs-rep2: (total reads: 50million, uniquely mapped reads: 44million, read length: 150bp, paired-end.)
MED1, β3-AR-stimulated control BAs-rep1: (total reads: 59million, uniquely mapped reads: 52million, read length: 150bp, paired-end.)
MED1, β3-AR-stimulated control BAs-rep2: (total reads: 59million, uniquely mapped reads: 52million, read length: 150bp, paired-end.)

Input, vehicle-treated control human BAs-rep1: (total reads: 160million, uniquely mapped reads: 148million, read length: 150bp, paired-end.)
Input, vehicle-treated control human BAs-rep2: (total reads: 177million, uniquely mapped reads: 164million, read length: 150bp, paired-end.)
H3K27ac, vehicle-treated control human BAs-rep1: (total reads: 156million, uniquely mapped reads: 148million, read length: 150bp, paired-end.)
H3K27ac, vehicle-treated control human BAs-rep2: (total reads: 159million, uniquely mapped reads: 151million, read length: 150bp, paired-end.)
Input, FSK-treated control human BAs-rep1: (total reads: 176million, uniquely mapped reads: 163million, read length: 150bp, paired-end.
Input, FSK-treated control human BAs-rep2: (total reads: 157million, uniquely mapped reads: 146million, read length: 150bp, paired-end.)
H3K27ac, FSK-treated control human BAs-rep1: (total reads: 197million, uniquely mapped reads: 186million, read length: 150bp, paired-end.)
H3K27ac, FSK-treated control human BAs-rep2: (total reads: 166million, uniquely mapped reads: 157million, read length: 150bp, paired-end.)
H2A.Z, FSK-treated control human BAs-rep1: (total reads: 158million, uniquely mapped reads: 147million, read length: 150bp, paired-end.)
H2A.Z, FSK-treated control human BAs-rep2: (total reads: 160million, uniquely mapped reads: 149million, read length: 150bp, paired-end.)

Antibodies

H2A.Z antibody (5 µg for ChIP-seq in murine brown adipocytes), Abcam, ab4171, lot#GR3402075-1; H2A.Z antibody (5 µg for ChIP-seq in primary human brown adipocytes), Active Motif, 39943, lot#00913003; H3K27ac antibody (5 µg for ChIP-seq), Active Motif, 39133, lot#31521015; H3K4me3 antibody (5 µg for ChIP-seq), Millipore Sigma, 07-473, lot#4022818; normal rabbit IgG (5 µg for ChIP-seq), Cell signaling, 2729, lot#10; CTCF antibody (10 µl for ChIP-seq), Cell signaling, 3418S, lot#6; SMC1 antibody (5 µg for ChIP-seq), ThermoFisher Scientific, A300-055A, lot#6; MED1 antibody (5 µg for ChIP-seq, 1:1000 for WB), ThermoFisher Scientific, PA5-36114, lot#ZD4269742.

Peak calling parameters

```
bam=$1 ## path for chip bam file
Igg=$2 ## path for IgG bam file
label=$3 ## label for this sample

echo "++++sort and uniq bam"
samtools sort ${bam} --output-fmt BAM > ${bam}.sorted.bam
picard MarkDuplicates I=${bam}.sorted.bam O=${bam}.dedup.bam REMOVE_DUPLICATES=true ASSUME_SORTED=true
VALIDATION_STRINGENCY=LENIENT METRICS_FILE=${bam}_metrices1.txt

echo "++++sort and uniq background IgG or Input"
dedup_Igg=${Igg}.dedup.bam
if [ -f "$dedup_Igg" ]; then
    echo "+++IgG dedup bam exists!"
else
    samtools sort ${Igg} --output-fmt BAM > ${Igg}.sorted.bam
    picard MarkDuplicates I=${Igg}.sorted.bam O=${dedup_Igg} REMOVE_DUPLICATES=true ASSUME_SORTED=true
VALIDATION_STRINGENCY=LENIENT METRICS_FILE=${Igg}_metrices1.txt
fi

export SAMTOOLS_X=0.1.19

echo "++++Danpos to call peaks"
python.danpos2 /programs/x86_64-linux/danpos2/2.2.2/danpos.py dpeak ${bam}.dedup.bam -b ${dedup_Igg} --smooth_width 0 -o
$label -c 25000000 --frsz 150 --extend 150
```

Data quality

The ChIP-seq data quality was inspected by CHIPs pipeline, including sequencing quality, mapping quality, total peak number, 10 fold peak number, Fraction of reads in the peaks (FRiP), PCR bottleneck coefficient (PBC), conservation around peak summit.

Software

The ChIP-seq data was analyzed by CHIPs pipeline (https://github.com/liulab-dfci/CHIPS) and DANPOS2 (https://sites.google.com/site/danposdoc/)